9-5-2013 12:00 AM

Second-order Analysis of Cable-stayed Bridge Deck Slabs

Zachary McNeil, *The University of Western Ontario*

Supervisor: Dr. F. Michael Bartlett, *The University of Western Ontario*

A thesis submitted in partial fulfillment of the requirements for the Master of Engineering Science degree in Civil and Environmental Engineering

SECOND-ORDER ANALYSIS OF CABLE-STAYED BRIDGE DECK SLABS

(Thesis format: Monograph)

by

Zachary McNeil

Graduate Program in Civil and Environmental Engineering

A thesis submitted in partial fulfillment
of the requirements for the degree of
Master of Engineering Science

The School of Graduate and Postdoctoral Studies
The University of Western Ontario
London, Ontario, Canada
September 2013

ABSTRACT

Current provisions in CSA S6-06 "Canadian Highway Bridge Design Code" for computing second-order effects in slender concrete beam-columns were derived for columns in buildings, where these effects can often be neglected, so their applicability to extremely slender cable-stayed bridge decks warrants investigation. The research reported in this thesis first reviews the provisions in CSA S6-06, as well as eight equations proposed by others, for computing the flexural rigidity, *EI*, of slender concrete beam-columns. Methods for quantifying the rotational restraint provided at deck slab supports by steel or concrete floorbeams are presented and validated: steel floorbeams provide negligible restraint but concrete floorbeams can provide sufficient restraint to reduce markedly the effective length factor. A rational method is presented and validated for analyzing continuous beam-columns subjected to transverse loads applied between their supports. A sensitivity analysis demonstrates that the variables that influence the moment magnification of cable-stayed bridge decks are: the applied axial load, the slenderness ratio, the concrete compressive strength, and the rotational restraint provided at the deck slab supports. Lastly, the deficiency of the provisions in CSA S6-06 for designing a simplified three-span cable-stayed bridge deck is demonstrated and recommendations are given to facilitate design office practice.

Keywords: Instability; cable-stayed bridge decks; slender beam-columns; second-order effects; flexural rigidity; reinforced concrete.

ACKNOWLEDGEMENTS

To my supervisor, Dr. Mike Bartlett, I am especially grateful. Dr. Bartlett's continuous guidance and cheerful encouragement have been invaluable during the past two years. His passion for structural engineering is inspirational and his dedication to his students and to the university is remarkable.

I would also like to thank Don Bergman from Buckland & Taylor Ltd. for his guidance regarding the axial stresses that are typical in cable-stayed bridge decks.

Financial support received from the National Science and Engineering Research Council of Canada and the Queen Elizabeth II Graduate Scholarship Program is gratefully acknowledged.

A special thanks to my parents, Maryanne and Terry, for their constant love and support. They have always been a phone call away when I needed them and have encouraged me in everything I have pursued. Lastly, to Terra, thank you for being with me throughout this journey. I know I can always count on you for support when I need it and for a helpful push in the right direction when I need that too!

TABLE OF CONTENTS

LIST OF TABLES

LIST OF FIGURES

NOMENCLATURE

A_g	area of the gross concrete section
A_s	area of tension steel reinforcement
A'_s	area of compression steel reinforcement
a	distance from the support to the applied load
b_e	effective flange width
C	applied compression force
C_c	critical buckling load
C_f	factored axial load
C_o	axial resistance of the cross section for zero applied moment
C_u	ultimate cross-sectional axial load resistance
c_m	non-uniform moment factor
c_u	neutral axis depth at the ultimate limit state
d	depth of reinforcement
E_c	modulus of elasticity of concrete
E_s	modulus of elasticity of steel reinforcement
E_{sc}	secant modulus of elasticity of concrete
E_{tc}	tangent modulus of elasticity of concrete
E_cI_g	uncracked rigidity
EI_{sec}	secant rigidity
EI_{tan}	tangent rigidity
EI	flexural rigidity
e	first-order end eccentricity
f'_c	28-day concrete compressive strength
f_c	concrete stress
f_y	yield stress of steel reinforcement
f_{LL}	flexibility coefficient for the left interior support due to a moment at the left interior support
f_{LR}	flexibility coefficient for the left interior support due to a moment at the right interior support
f_{RL}	flexibility coefficient for the right interior support due to a moment at the left interior support
f_{RR}	flexibility coefficient for the right interior support due to a moment at the right interior support
G	shear modulus of elasticity
G_c	shear modulus of elasticity of concrete
H	height of cable-stayed bridge tower above the deck
h	height of the cross section
h_s	deck slab thickness
J	torsional constant
I_g	moment of inertia of the gross concrete section

I_s moment of inertia of the steel reinforcement
I_x moment of inertia about the x-axis
I_y moment of inertia about the y-axis
K_e rotational restraint provided by the vertical eccentricity of the deck slab
K_θ rotational restraint provided by the transverse floorbeams
k_θ rotational restraint per unit width of slab provided by the transverse floorbeams
k effective length factor
k_G flexural stiffness accounting for second-order effects (k_{GL}: left adjacent span; k_{GR}: right adjacent span)
L compression member length, equivalent to the floorbeam spacing
L_m main span length
M bending moment
M_c maximum total moment at the critical section ($M_{c,A}$: actual value; $M_{c,S}$: simulated value)
M_d decompression moment
M_u ultimate cross-sectional moment capacity
M_y yield moment
M_L moment at the left interior support
M_R moment at the right interior support
M^* total moment
M_2 maximum applied first-order end moment
M_2^* maximum applied first-order end moment computed using *CSDECK*
P applied vertical point load
P_e restraining force provided by the vertical eccentricity of the deck slab
p_e uniform restraint provided by the vertical eccentricity of the deck slab
r radius of gyration
s spacing of the longitudinal girders
T applied torque
T_e restraining torque provided by the vertical eccentricity of the deck slab
UB_C upper-bound property for concrete floorbeams
UB_S upper-bound property for steel floorbeams
LB_C lower-bound property for concrete floorbeams
LB_S lower-bound property for steel floorbeams
w slab width
y distance from the extreme compression fibre to the concrete layer centroid
$\bar{y}$ distance from the extreme compression fibre to the floorbeam centroid

Greek Symbols

α	variable rigidity factor in equations proposed by others
β	coefficient in rigidity equations by Tikka and Mirza (2008)
β_d	sustained load factor
β_1	ratio of equivalent stress block depth to the neutral axis depth
γ_L	modification factor to account for second-order effects in the left adjacent span
γ_R	modification factor to account for second-order effects in the right adjacent span
δ	moment magnifier (δ_L: computed using linear-uncracked first-order analysis; δ_{NL}: computed using nonlinear-cracked first-order analysis)
Δ	deflection
Δ_e	deflection of floorbeam centroid due to the vertical eccentricity of the deck slab
ε	strain
ε_c	extreme compression fibre strain (ε_{cu}: at the ultimate limit state)
ε_o	strain corresponding to the peak concrete stress
η	coefficient in rigidity equation by Nathan (1983)
η_e	relative eccentricity factor in rigidity equation by Bonet et al. (2011)
θ	rotation
θ_L	primary rotation at the left end of the interior span
θ_R	primary rotation at the right end of the interior span
θ_{LL}	rotation at the left end of the interior span due to the unit moment at the left interior support
θ'_{LL}	rotation at the right end of the left adjacent span due to the unit moment at the left interior support
θ_{RR}	rotation at the right end of the interior span due to the unit moment at the right interior support
θ'_{RR}	rotation at the left end of the right adjacent span due to the unit moment at the right interior support
θ_{RL}	rotation at the right end of the interior span due to the unit moment at the left interior support
ξ_φ	sustained load factor in rigidity equation proposed by Bonet et al. (2011)
ρ_g	gross reinforcement ratio
φ	creep coefficient from Eurocode 2
ϕ_m	member resistance factor
ψ	curvature
ψ_c	curvature at the critical section
Ψ	relative stiffness ratio
ω	uniformly distributed load (ω_D: dead load; ω_L: live load)
Ω	coefficient in rigidity equation by Nathan (1983)

CHAPTER 1: INTRODUCTION

1.1 INTRODUCTION

Cable-stayed bridges are elegant structures that are economical for spans less than 1200m. The configuration has only recently been chosen for spans over 1000m that historically were the domain of the suspension bridge (Hauge & Anderson, 2011). As the pushing of the span envelope continues, the use of slender girder systems is no longer just an aesthetic preference but a necessity due to self-weight considerations.

Steel girder systems provide lightweight superstructures and therefore are used for very long spans. They are also relatively costly, however, and so should only be used when the reduction in weight can significantly reduce the cross sections of the cables, pylons, and piers (Gimsing & Georgakis, 2012). Composite systems, shown by the cross section in Figure 1.1 a), comprising steel girders and floorbeams with precast concrete deck slabs have become popular because a desirable self-weight is maintained, and the pre-fabricated components allow for efficient cantilever construction. Composite action is achieved by connecting the precast slabs to the steel girders using cast-in-place infill joints. This connection allows the deck slabs to contribute to both the compressive and bending resistance of the composite girder system. For shorter spans, when self-weight restrictions are not as severe, concrete girder systems, shown by the cross section in Figure 1.1 b), are also used, where the deck slab is cast monolithically with the floorbeams and the girders and so also contributes to the compression and bending resistance of the cross section.

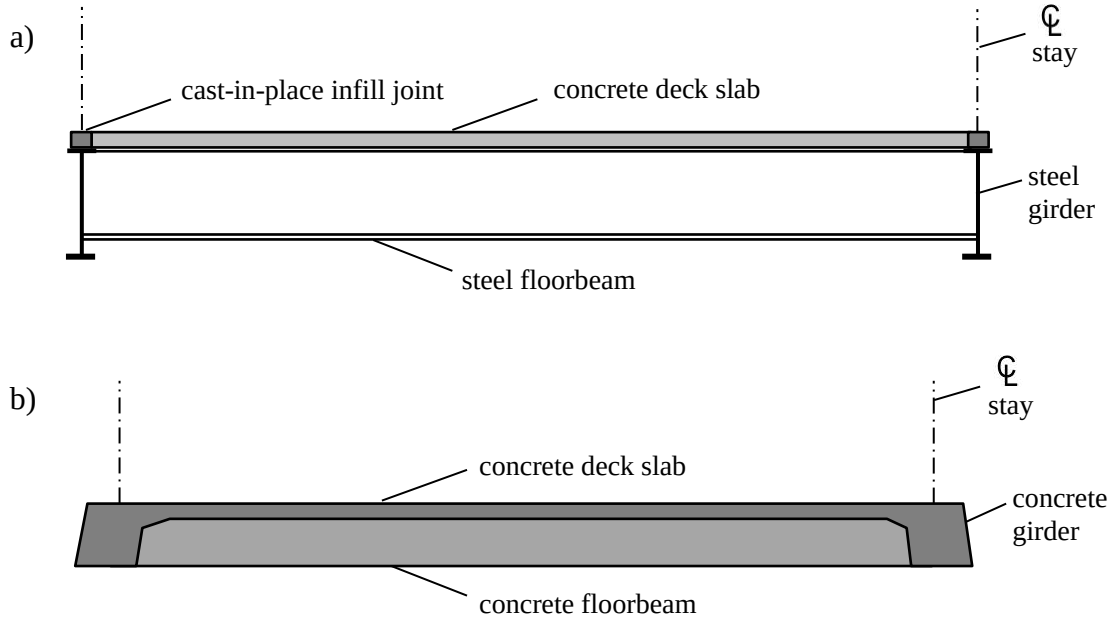

Figure 1.1: Cable-stayed bridge girder cross sections: a) composite girder system; b) concrete girder system.

In both girder systems shown in Figure 1.1, the deck slab must resist local bending moments from traffic loads applied between floorbeams, compression forces due to global bending of the girder system, and additional compression forces from the horizontal component of the stay cable tensions, as shown in Figure 1.2. The global axial force diagram of a typical cable-stayed bridge, shown in Figure 1.2 a), generally has a parabolic shape with the maximum compression at the towers. The typical global bending moment diagram, shown in Figure 1.2 b), is characterized by positive moments larger than the negative moments in regions with significant compression and positive and negative moments of similar magnitude near midspan where the compression is the least (Gimsing & Georgakis, 2012). The deck slab will act as a compression flange for the girder system, resisting global axial loads and positive moments, as shown in Figure 1.2 c), but will only resist negative bending moments if there is sufficient axial force to prevent tensile stresses in the deck. The stress blocks in Figure 1.2 c) are shown at the

ultimate limit state. The deck slabs spanning between the floorbeams also resist local moments resulting from traffic loads, shown in Figure 1.2 d), which will generally be positive beneath the applied load and negative above the supports.

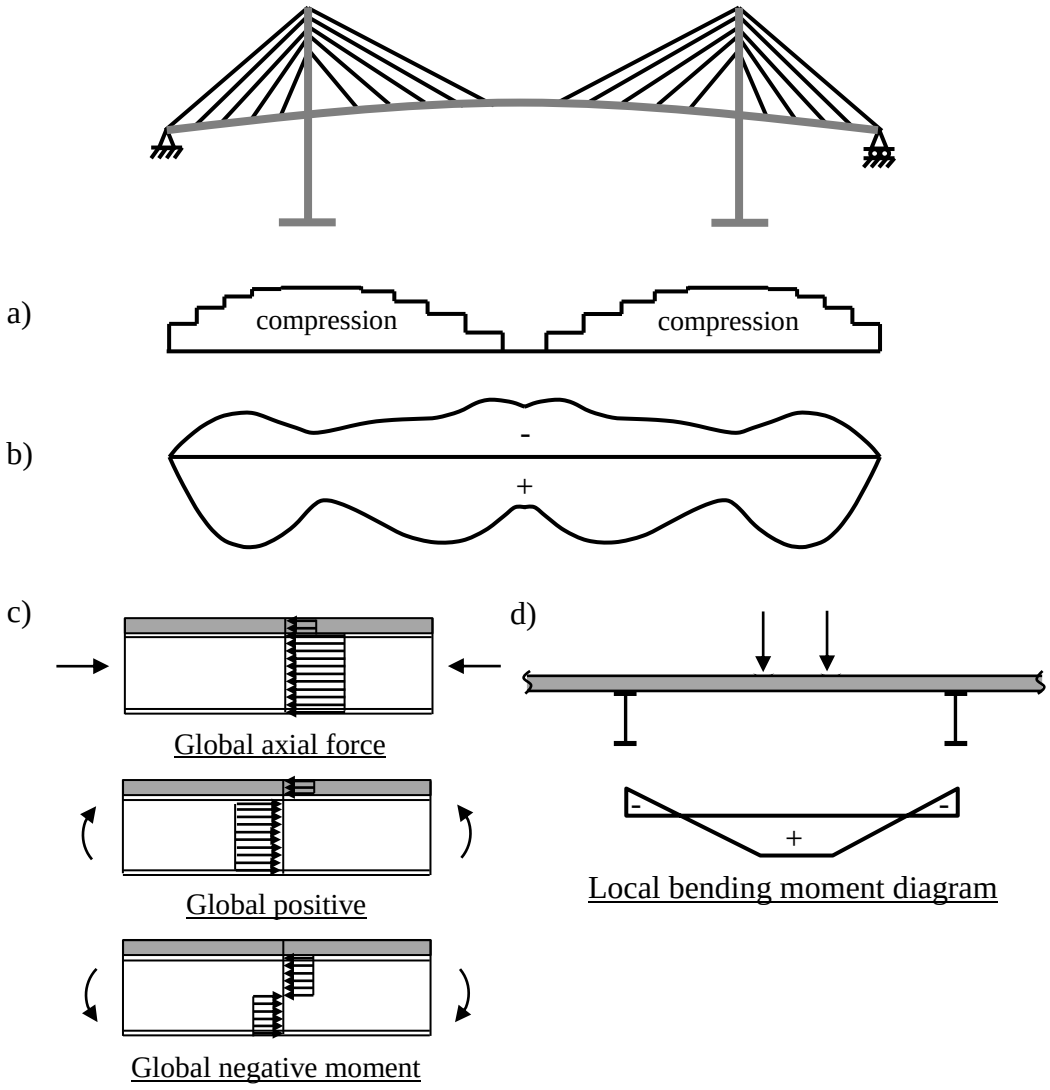

Figure 1.2: Simple cable-stayed bridge including typical a) global axial force diagram, b) global bending moment envelope (from Gimsing & Georgakis, 2012), c) global force effects on sections of the girder, and d) local force effects on the deck slab.

The maximum compression force at the towers due to the horizontal component of the stay cable tensions increases significantly as the main span length increases. For a fan

configuration, with all cables connected at the top of the tower, and uniform dead and live loads placed along the length of the main span, the maximum compression force, *C*, in the deck system is (Gimsing & Georgakis, 2012):

$$C = \frac{\left(\omega_D + \omega_L\right) L_m{}^2}{8H} \quad [1.1]$$

where ω_D and ω_L are uniformly distributed dead and live loads per unit length of deck, L_m is the main span length, and H is the height of the tower above the centroid of the deck system. For a constant uniformly distributed load, ω_D+ω_L, the compression force, C, should increase proportional to L_m, since the tower height, H, usually also increases proportionally to L_m (Gimsing & Georgakis, 2012). However, the increase in C requires a larger deck cross section, increasing the dead load per unit length, leading to a further increase in deck compression.

Figure 1.3 shows the approximate relationship between the compressive stress in the girder and main span length, proposed by Gimsing and Georgakis (2012) for a cable-stayed bridge with a constant deck width. The compressive stress is computed accounting for both the axial force from the horizontal component of the stay cable tensions and the additional stresses due to lateral bending of the girder system. The black-dashed line is a linear extrapolation of the original relationship and suggests that the span current limit for girder systems with concrete decks ($f'_c \leq 60$MPa) is in the order of 500m. For high-strength steel decks the theoretical limit is approximately 1500m (Gimsing & Georgakis, 2012). Clearly, if the current span envelope is to be extended, the self-weight of the

girder system must be reduced. For composite girder systems, lightweight concrete is not a viable option since undesirable creep properties and reduced elastic moduli result from using lightweight aggregates (e.g., Lopez, 2005). Therefore, minimizing the deck slab thickness seems to be the most viable option, although innovative panel cross sections, such as fluted panels, could also be considered (Bergman, 2011).

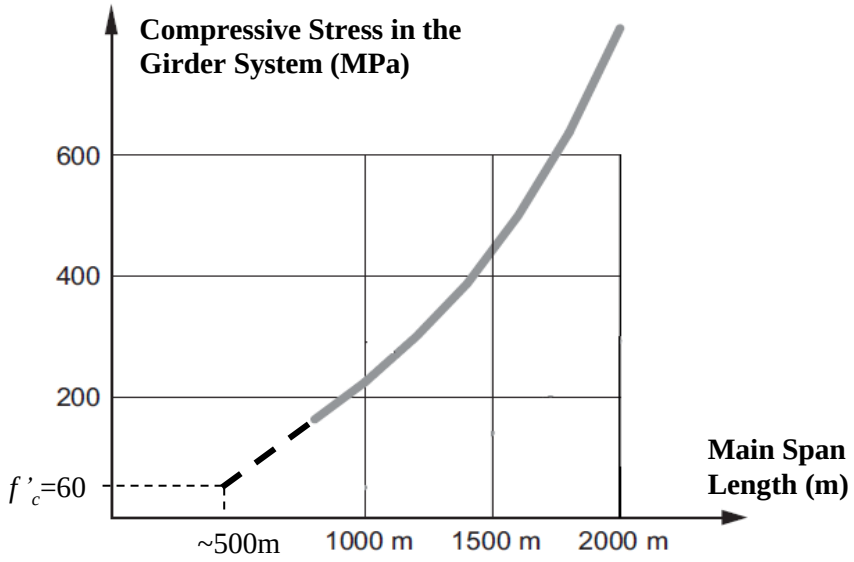

Figure 1.3: The maximum compressive stress in the girder system due to axial compression and lateral bending (after Gimsing & Georgakis, 2012).

Given that the panels are subjected to combined bending and axial compression loads, they must be designed as slender beam-columns since slenderness ratios larger than 70 can occur in practice. The longest cable-stayed bridge in Canada, the Alex Fraser Bridge in Vancouver, has a main span of 465m and its 215mm thick precast panels have slenderness ratios of 73 (CBA-Buckland & Taylor Ltd, 1983). Currently the longest cable-stayed bridge in North America, the John James Audubon Bridge near New Roads, Louisiana, has a main span 482m and consists of 240mm precast panels with slenderness

ratios of 66 (Schemmann et al., 2011). These members are extremely slender compared to typical building columns, where slenderness effects can usually be ignored (MacGregor, Breen, & Pfrang, 1970) and hence may require a more sophisticated analysis than is currently provided by Canadian standards.

1.2 SLENDER CONCRETE BEAM-COLUMNS

The essential response of a slender beam-column can be understood by considering a simple column bent in single curvature due to equal end moments, as shown in Figure 1.4. The factored axial load, C_f, applied at an initial eccentricity, e, creates a first-order end moment, M_2, equal to $C_f \cdot e$. The mid-height deflection of the column, Δ, results in a second-order moment, $C_f \cdot \Delta$, at mid-height of the member that further increases Δ. The total moment at the mid-height of the column is therefore the combination of the first- and second-order moments. If the second-order moment is less than 5% of the axial capacity of the column, the second-order behaviour is typically ignored (MacGregor, Breen, & Pfrang, 1970).

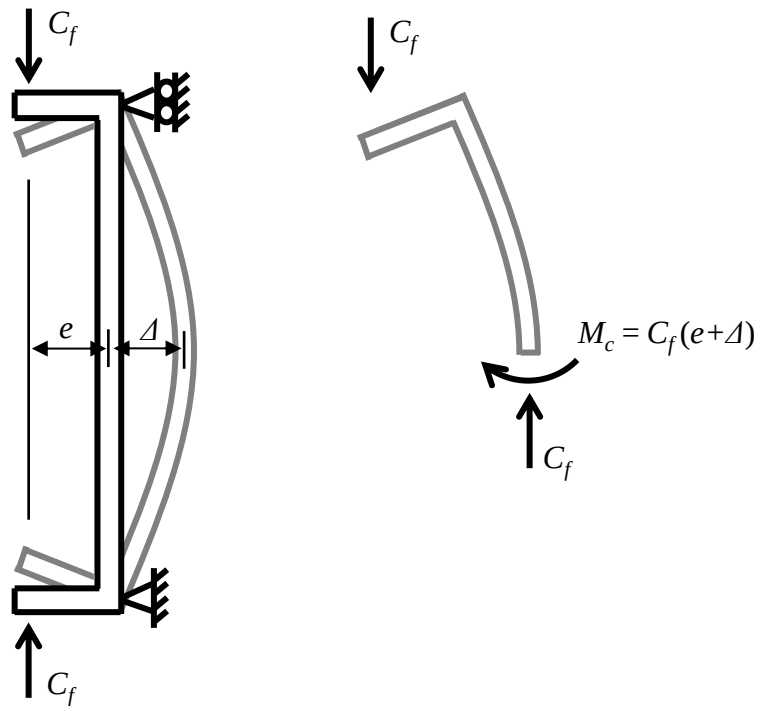

Figure 1.4: Forces on a simple slender column (after MacGregor & Bartlett, 2000).

Significant second-order effects can results in two failure modes, as demonstrated by the axial load versus bending moment diagram shown in Figure 1.5. The bold outer line is the capacity of the cross section. A short column, with no moment magnification, follows the linear load path shown until reaching the cross-section capacity at point A. An intermediate column will follow a nonlinear path, due to the C_f - Δ effect, until it fails when the cross-sectional strength is reached at point B. In both of these cases the cross-section capacity is reached, so the resistance of the column is limited by material failure. Slender (or "long") columns will not reach material failure but will fail at a maximum moment less than the cross-section capacity where the increase in moment for an increase in axial load, dM_c/dC, approaches infinity, as shown by point C. The moment magnification, due to the C_f - Δ effect, is usually very significant for long columns,

causing an instability failure to occur before the cross-section capacity is achieved (MacGregor & Bartlett, 2000).

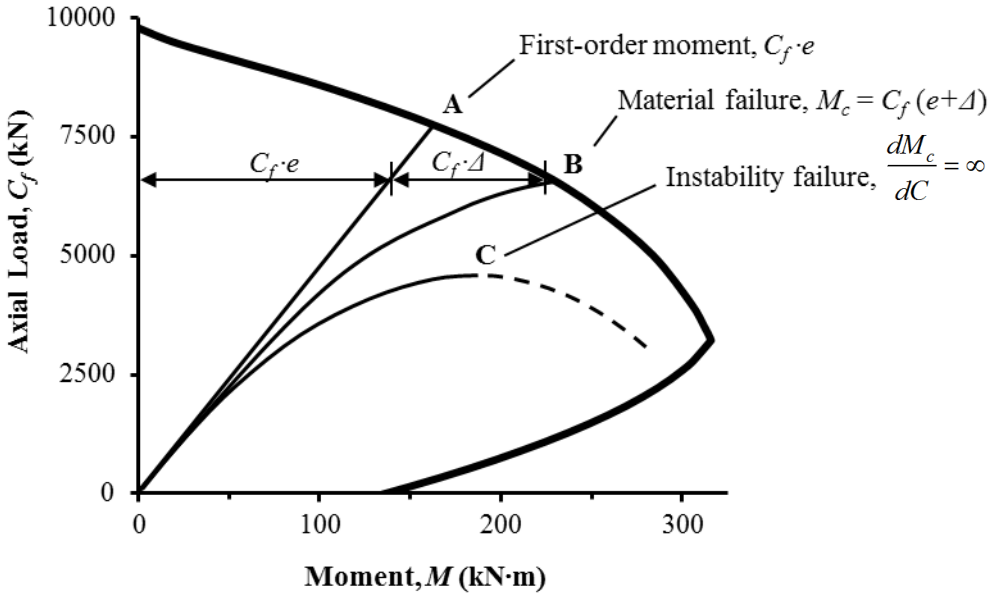

Figure 1.5: Cross-section interaction diagram showing the responses of a short column, A, an intermediate column, B, and a very slender column, C.

To further examine these failure modes, a distinction between secant and tangent member rigidities is necessary. Material failures are dependent on the moment magnification present and so on the secant rigidity at failure, EI_{sec}, which is simply the moment, M, divided by the corresponding curvature, ψ:

[1.2] $$EI_{sec} = \frac{M}{\psi}$$

A theoretical equation, first proposed by Anderson and Moustafa (1970), can be easily derived for the secant rigidity at material failure:

[1.3] $$EI_{sec} = \frac{M_u \cdot c_u}{\varepsilon_{cu}}$$

where the neutral axis depth at the ultimate limit states, c_u, is determined for the ultimate cross-sectional moment capacity, M_u, and the strain in the extreme compression fibre, ε_{cu}, is assumed to be equal to 0.0035 in CSA S6-06.

As the applied moment increases, the secant rigidity reduces as shown by the moment-curvature curve in Figure 1.6. At instability failure, which depends on the tangent rigidity at the failure point A, the maximum moment is less than the cross-section capacity, M_u, and hence the secant stiffness is greater than at material failure.

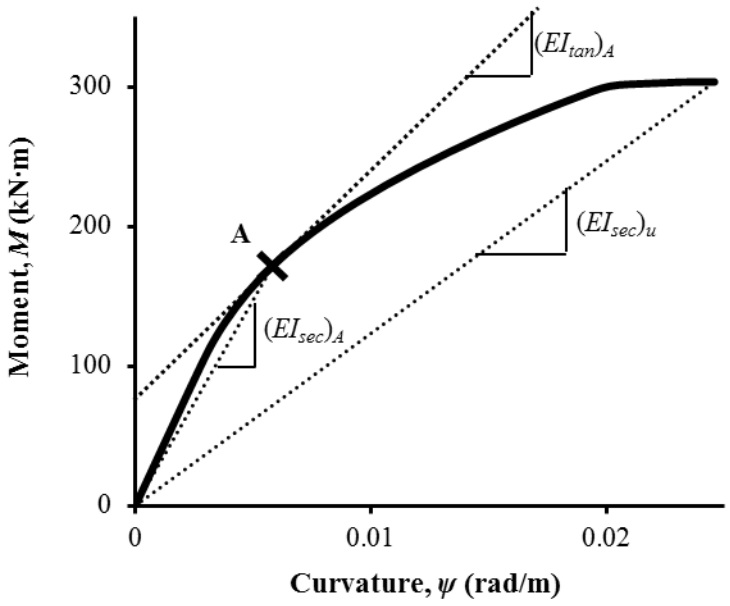

Figure 1.6: Relationship between the moment-curvature response and the secant and tangent rigidities.

Instability failure is dependent on the tangent rigidity of the member, $dM/d\psi$, which is also shown on Figure 1.6. Bartlett (1991) and others have developed a rational expression for the mid-height tangent rigidity, $dM_c/d\psi_c$, at instability, using the Euler buckling formula:

$$EI_{tan} = \frac{dM_c}{d\psi_c} = \frac{C_f \left(kL\right)^2}{\pi^2} \quad [1.4]$$

This expression for the critical tangent rigidity, EI_{tan}, can be derived by equating the change in end moment, dM_2, with respect to a change in mid-height curvature, $d\psi_c$, to zero. According to Eq. [1.4], the tangent rigidity at failure must increase, and so the mid-height moment at stability failure must decrease, Figure 1.6, when either the factored axial load, C_f, or the effective length of the member, kL, increases. Since the critical tangent rigidity is defined by the cross-section response and the susceptibility of the member to buckling, it can be quantified by drawing the member-stability-effect line, through the origin of the cross-section moment-curvature curve with a slope equal to that given by the right hand side of Eq. [1.4], as shown in Figure 1.7. The critical mid-height moment, M_c, and corresponding curvature, ψ_c, at failure can then be determined as the point on the moment-curvature curve where the tangent rigidity is parallel to the member-stability-effect line. This effectively maximizes the first-order end moment, M_2, at failure which is the difference between the moment-curvature curve and the "member-stability-effect line," as shown, yielding:

[1.5] $$M_2 = M_c - \left(\frac{C_f \left(kL\right)^2}{\pi^2} \right) \psi_c$$

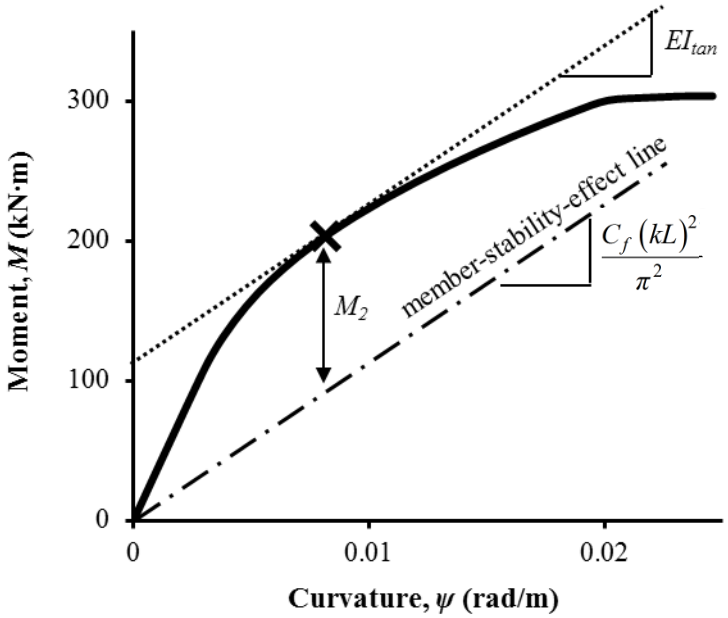

Figure 1.7: Moment-curvature response of a member susceptible to instability (after Bartlett, 1991).

This method is a rational approach to determine the capacity of very slender members such as cable-stayed bridge decks, but it applies only to simply supported members with equal end eccentricities, causing single curvature. However, cable-stayed bridge decks are often subjected non-uniform local moments from traffic loading applied between the floorbeam supports, as was shown in Figure 1.2 d). These moments are typically positive at midspan and negative at the supports, since rotations of the ends of the deck slab are partially restrained by the adjacent deck slabs and the transverse floorbeams. Rational methods are not currently available for computing the second-order effects in continuous beam-columns subjected to transverse loads between the supports, so further

investigation is required to determine the response of continuous beam-columns subjected to non-uniform first-order moments.

1.3 SLENDER COLUMNS IN CSA S6-06

For reinforced concrete members with slenderness ratios less than 100, CSA S6-06 (CSA, 2006) allows slenderness effects to be computed using a moment magnifier, δ, computed as:

[1.6] $$\delta = \frac{c_m}{1 - \left(\frac{C_f}{0.75 C_c} \right)}$$

The magnified moment, M_c, equivalent to $C_f(e+\Delta)$ in Figure 1.4, is computed as the product of the moment magnifier, δ, and the larger first-order end moment, M_2. The factor, c_m, accounts for unequal end moments and is taken as 1.0 for members with transverse loads applied between supports, such as traffic loads applied to the deck slabs of cable-stayed bridges. The 0.75 factor accounts for uncertainties in determining the critical buckling load (Bartlett, 1991), C_c, where C_c is the Euler Buckling Load given by:

[1.7] $$C_c = \frac{\pi^2 EI}{(kL)^2}$$

where *EI* is the rigidity and *kL* is the effective buckling length. For moment magnification, the rigidity of the column, *EI*, must represent the secant rigidity, which is approximated using two equations in CSA S6-06:

[1.8] $$EI = \frac{0.2E_c I_g + E_s I_s}{(1+\beta_d)}$$

[1.9] $$EI = 0.25E_c I_g$$

In these equations, E_c and E_s are the elastic moduli for concrete and steel respectively, and I_g and I_s are the moments of inertia about the centroid of the section for the gross concrete section and the steel reinforcement, respectively. The factor β_d accounts for the fraction of applied load that is sustained. Equation [1.8] is more accurate than Eq. [1.9], although for lightly reinforced concrete members the more conservative Eq. [1.9] tends to produce acceptable results (MacGregor, Breen, & Pfrang, 1970). The simplicity of Eq. [1.9] is often preferred during preliminary stages of design.

Provided it can be justified, CSA S6-06 allows the use of an effective length factor, *k*, less than 1 for members in braced frames. There is no guidance, however, for computing *k* for cable-stayed bridge deck slabs restrained by transverse floorbeams.

Equations [1.6] through [1.9] were developed by MacGregor, Breen, and Pfrang (1970) for columns in buildings that typically are quite stocky and so have minimal second-order effects. For this reason, Eqs. [1.8] and [1.9] are intended to approximate the secant

rigidity of the section at material failure. If a member fails by instability, the maximum moment will be less than the cross-section capacity, M_u, and the secant rigidity at failure will likely be much greater than that predicted by Eqs. [1.8] or [1.9], as was shown in Figure 1.6 (Bartlett, 1991).

1.4 INSTABILITY OF CABLE-STAYED BRIDGE DECKS

Very slender columns fail due to instability before the maximum moment along the member reaches the cross-section capacity, i.e. when $dM_c/dC=\infty$, as shown in Figure 1.5. Since the CSA S6-06 rigidity equations, Eqs. [1.8] and [1.9], were derived primarily for material failures, their extension to the analysis of instability failures is hard to justify. The inaccuracy associated with their use to compute the resistance of a cable-stayed bridge deck with a slenderness ratio of 73 was reported by Bartlett (1991). Slender column resistances computed using rigidity equations similar to those in CSA S6-06 were compared to those obtained by computing the critical mid-height moment associated with the critical tangent rigidity, Eq. [1.4], and the corresponding first-order end moment using Eq. [1.5]. The results varied significantly between the two approaches, with the code provisions providing extremely conservative resistances in the compression failure region and unconservative capacities in the tension failure region.

Bartlett (1991) assumed the deck was simply supported and was subjected to equal and opposite end moments. Rotational restraint provided by the floorbeams was neglected, so the effective length, kL, was equal to the floorbeam spacing, L. Given that the current method in CSA S6-06 was shown to be inaccurate for this simplified case, its application

to more complex non-uniform loading conditions can also be expected to contain significant error, so other methods proposed in the literature must be examined.

1.5 RESEARCH OBJECTIVES

The objectives of this research are as follows:

1) Determine the accuracy of the current methods in the literature for computing the rigidity, *EI*, of slender concrete beam-columns.
2) Develop approximate methods for computing the rotational restraint provided by steel or concrete transverse floorbeams and apply these methods to compute the effective length of cable-stayed bridge decks.
3) Develop a rational method for computing first- and second-order moments in continuous, slender beam-columns subjected to transverse point loads between the supports.
4) Implement the method into a computer program capable of analyzing an idealized cable-stayed bridge deck system.
5) Perform a sensitivity analysis of the parameters that influence the moment magnification of continuous cable-stayed bridge decks.
6) Provide recommendations to practicing designers.

1.6 THESIS OUTLINE

Chapter 2 contains detailed review of eight methods proposed in the literature for computing *EI* of slender concrete beam-columns bent in single curvature due to equal end moments. Chapter 3 presents and validates approximate methods for quantifying the

rotational restraint provided at the ends of the deck slab span by steel or concrete transverse floorbeams. Chapter 4 presents and validates a rational method for computing second-order effects in continuous beam-columns subjected to transverse point loads applied between the supports. Chapter 5 presents a sensitivity analysis to determine the parameters that influence the moment magnification of slender cable-stayed bridge decks. Chapter 6 provides a summary of the research contained in this thesis, highlights the main conclusions, offers advice for practicing designers, and provides recommendations for future work.

CHAPTER 2: REVIEW OF SLENDER COLUMN ANALYSES IN THE LITERATURE

2.1 SIMPLIFIED *EI* EQUATIONS PROPOSED IN THE LITERATURE

Several equations for the effective rigidity, *EI*, of slender columns have been developed since the moment magnifier equation, Eq. [1.6], was introduced by MacGregor et al. in 1970. The equations in Table 2.1 include:

- two rigidity equations provided in CSA S6-06, Eqs. [1.8] and [1.9],
- six equations that have been proposed in the literature to replace the current code equations, Eqs. [2.1] to [2.6],
- one theoretical equation for the secant rigidity at material failure first proposed by Anderson and Moustafa (1970), Eq. [1.3].

All equations yield nominal rigidities and, with the exception of Eq. [2.1], should be used with the stability resistance factor of 0.75, which accounts for uncertainties in determining the buckling load, C_c, in Eq. [1.6].

Table 2.1: Proposed equations for the rigidity, *EI*.

Eq. [#]	Author (year)	General Form of Equation	Variable Rigidity Factors
[1.8]	CSA (2006) #1	$EI = \frac{0.2E_cI_g + E_sI_s}{(1+\beta_d)}$	
[1.9]	CSA (2006) #2	$EI = 0.25E_cI_g$	

Table 2.1 (cont.): Proposed equations for the rigidity, *EI*.

Eq. [#]	Author (year)	General Form of Equation	Variable Rigidity Factors
[2.1]	Nathan (1983)	$EI = \frac{E_c I_g}{\alpha\left(1+\beta_d\right)}$	$\alpha = \eta\Omega \geq 1.5$ $\eta = \frac{3}{C_f/C_o} - \frac{0.02}{\left(C_f/C_o\right)^2}$ $7 \leq \eta \leq 100$ Sections with no compression flange: $\Omega = \frac{17}{kL/r}$
[2.2]	Khuntia & Ghosh (2004)[a]	$EI = \alpha E_c I_g \left(0.80 + 25\rho_g\right)$	$\alpha = \left(1 - \frac{e}{h} - 0.5\frac{C_f}{C_o}\right)$
[2.3]	Olendzki (2008)	$EI = \frac{\alpha E_c I_g + E_s I_s}{\left(1+\beta_d\right)}$ $E_c = 4733\sqrt{f'_c}$	$\alpha = \left(0.81 - 0.004\frac{kL}{r}\right)$
[2.4]	Tikka & Mirza (2008) #1	$EI = \frac{\alpha E_c \left(I_g - I_s\right)}{\left(1+\beta_d\right)} + 0.85E_s I_s$	$\alpha = 0.48 - 3.5\frac{e}{h}\left[\frac{1}{1+\beta\left(\frac{e}{h}\right)}\right] + 0.00058\frac{kL}{r}$ $\beta = 7 \quad \text{for } \rho_g \leq 2\%$
[2.5]	Tikka & Mirza (2008) #2	$EI = \frac{\alpha E_c I_g}{\left(1+\beta_d\right)} + 0.8E_s I_s$	$\alpha = 0.47 - 3.5\frac{e}{h}\left[\frac{1}{1+\beta\left(\frac{e}{h}\right)}\right] + 0.00087\frac{kL}{r}$ $\beta = 7 \quad \text{for } \rho_g \leq 2\%$
[2.6]	Bonet, Romero & Miguel (2011)	$EI = \frac{\alpha E_c I_g}{\left(1+\varphi\right)} + \frac{E_s I_s}{\left(1+\xi_\varphi\right)}$ $E_c = 22{,}000\left(f'_c/10\right)^{0.3}$ $\xi_\varphi = 1.9\varphi\exp\left(\frac{-kL}{25r}\right)$	$\eta_e = \frac{e}{4r}$ For η_e < 0.2: $\alpha = \left(1.95 - 0.035\frac{kL}{r} - 0.25\varphi\right)\left(\eta_e - 0.2\right)$ $+\left(f'_c/225 + 0.11\right) \geq 0.1$ For $\eta_e \geq 0.2$: $\alpha = \left(f'_c/110 + 0.45\right)\left(0.2 - \eta_e\right)$ $+\left(f'_c/225 + 0.11\right) \geq 0.1$
[1.3]	Anderson & Moustafa (1970)[a]	$EI = \frac{M_u c_u}{\varepsilon_{cu}}$	

[a] No discussion of β_d.

In Table 2.1, E_c and E_s are the concrete and steel moduli of elasticity, respectively. The moments of inertia of the gross uncracked concrete section and the steel reinforcement are I_g and I_s, respectively. The sustained load factor is β_d, kL is the effective buckling length, and r is the radius of gyration. The eccentricity of the applied load, C_f, is e and C_o is the factored axial resistance of the cross section for zero applied moment. The height of the cross section is h, ρ_g is the gross reinforcing ratio, and f'_c is the 28-day concrete compressive strength in MPa. The creep coefficient used in Eq. [2.6], φ, is recommended by Bonet et al. (2011) to be taken from Eurocode 2 (European Committee for Standardization, 2004). The ultimate neutral axis depth, c_u, in Eq. [1.3] corresponds to the cross-sectional moment resistance, M_u, at the applied load, C_f, and the ultimate strain in the extreme compression fibre, ε_{cu}, is assumed to be 0.0035 in CSA S6-06. Most of the equations contain a variable rigidity factor, α, as defined in the rightmost column.

Each of these equations is restricted to certain limitations that may limit its applicability to cable-stayed bridge deck design. The deck panels in the Alex Fraser Bridge in Vancouver have slenderness ratios of 73 (CBA-Buckland & Taylor Ltd, 1983), so the typical range of slenderness ratios, kL/r, was assumed to be from 60 to 80. Similarly, the typical range of gross reinforcing ratios, ρ_g, is assumed to be from 0.5 to 2%, since the deck panels in the Alex Fraser Bridge have reinforcing ratios ranging from 0.6 to 1.3%. The basis and limitations of the proposed equations are discussed in detail in Appendix A.

A variation on Eq. [1.3] was suggested by Shuraim and Naaman (2003) for slender prestressed concrete columns. As shown in Figure 2.1, they propose adopting the secant rigidity corresponding to the applied end eccentricity, $e = M_2/C_f$, shown as point B, instead of taking the rigidity at the applied load C_f , point A, as suggested by Anderson and Moustafa (1970).

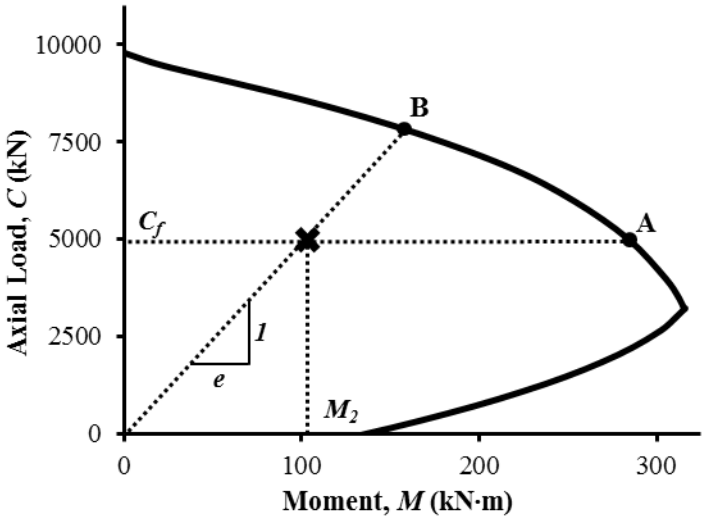

Figure 2.1: Interaction diagram showing Shuraim and Naaman's (2003) proposal for calculating the secant rigidity using Eq. [1.3].

The computed rigidity proposed by Shuraim and Naaman (2003) is compared to the results from their finite element analysis in Figure 2.2. At low eccentricity ratios, *e*/*h*, the method greatly underestimates the rigidity, as shown by the dashed line. To avoid extreme conservatism at these eccentricities, they further proposed that the rigidity should not be taken less than the peak secant rigidity, shown by point B on Figure 2.2. The peak secant rigidity can be obtained by setting the derivative of the secant rigidity equation, Eq. [1.3], to zero. For rectangular sections, the ultimate neutral axis depth at the peak rigidity simplifies to:

[2.7] $$c_u = \frac{2h}{3\beta_1}$$

where β_1 is the ratio of the equivalent rectangular stress block depth to the neutral axis depth.

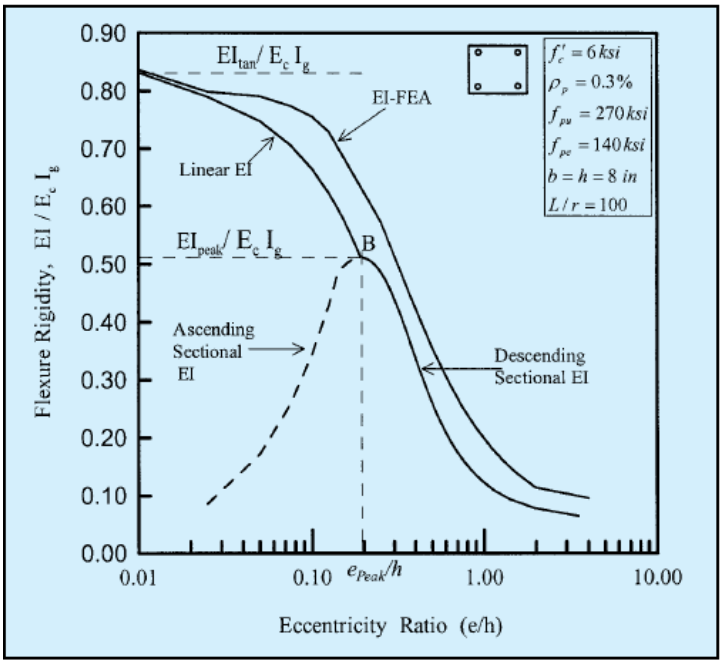

Figure 2.2: The rigidity using the method proposed by Shuraim and Naaman compared to results from their finite element analysis (from Shuraim & Naaman, 2003).

Shuraim and Naaman (2003) assume that the ultimate neutral axis depth is known for a sufficient number of points defining the short column interaction diagram. The ultimate axial load and moment resistances, C_u and M_u, at the peak rigidity can then be computed by interpolating between these values for the c_u value obtained from Eq. [2.7]. If the short column interaction curve is not available, an iterative procedure is required to determine

the C_u and M_u corresponding to c_u from Eq. [2.7]. Once both the M_u and c_u values are known, the peak rigidity can be computed using Eq. [1.3].

For applied end eccentricities less than that corresponding to the peak rigidity, they propose computing the rigidity by interpolating between the peak secant rigidity, point B on Figure 2.2, and the tangent rigidity under concentric axial load, EI_{tan}, shown by the dashed line, which is computed as:

[2.8] $$EI_{tan} = E_{tc} I_g$$

where E_{tc}, the concrete tangent modulus of elasticity, computed as:

[2.9] $$E_{tc} = \frac{2 f'_c}{\varepsilon_o}\left(1 - \frac{\varepsilon}{\varepsilon_o}\right)$$

where ε_o is the strain corresponding to the peak stress, f'_c, and the strain, ε, at failure under concentric axial load is computed as:

[2.10] $$\varepsilon = \left[\varepsilon_o + \left(\frac{\pi r}{kL}\right)^2\right] - \sqrt{\varepsilon_o{}^2 + \left(\frac{\pi r}{kL}\right)^4}$$

The derivation of Eqs. [2.9] and [2.10] are presented in Appendix A.

2.2 INFLUENCE OF KEY VARIABLES ON THE SIMPLIFIED *EI* EQUATIONS

The equations shown in Table 2.1, except Eqs. [1.8] and [1.9], yield flexural rigidities that are not constant for a given cross section. There is little agreement regarding which variables influence the rigidity, however, as shown in Table 2.2. The symbol ✗ indicates that the equation neglects the contribution of a particular variable to the effective rigidity, while the symbol ✓ indicates the equation specifically addresses the instability case. A plus, +, or minus sign, -, indicates that an increase in a particular variable will increase or decrease the effective rigidity, respectively. As will be detailed in this section, there is limited consensus of which variables are important or how a particular variable impacts the rigidity.

Table 2.2: Variables included in the proposed rigidity equations.

Eq. [#]	Author (year)	e	$\frac{C_f}{C_o}$	$\frac{kL}{r}$	ρ_g or I_s	f'_c or E_c	Address Instability
[1.8]	CSA (2006) #1	✗	✗	✗	+	+	✗
[1.9]	CSA (2006) #2	✗	✗	✗	✗	+	✗
[2.1]	Nathan (1983)	✗	+	+	✗	+	✓
[2.2]	Khuntia & Ghosh (2004)	-	-	✗	+	+	✗
[2.3]	Olendzki (2008)	✗	✗	-	+	+	✗
[2.4]	Tikka & Mirza (2008) #1	-	✗	+	+	+	✗
[2.5]	Tikka & Mirza (2008) #2	-	✗	+	+	+	✗
[2.6]	Bonet, Romero & Miguel (2011)	+/-	✗	+	+	+	✓
[1.3]	Anderson & Moustafa (1970)	+/-	+/-	✗	+	+	✗
[1.3] & [2.8]	Shuraim & Naaman (2003)	+/-	+/-	✗	+	+	✓

All of the proposed methods account for the increase in effective rigidity resulting from an increase in the concrete modulus of elasticity, E_c, as shown in Table 2.2. All of the methods except the simplified CSA S6-06 Eq. [1.8] and Eq. [2.1] proposed by Nathan (1983) account for an increase in rigidity due to increased reinforcement, either ρ_g or I_s.

In Eqs. [2.1], [2.4] and [2.5], and [2.6], the rigidity increases as the slenderness ratio, kL/r, increases. Increasing the slenderness increases the likelihood of an instability failure (e.g. Bonet et al., 2011) and the associated rigidity is greater. Clearly the rigidity used must correspond to the correct mid-height moment, M_c. Hence, the rigidity, EI, increases as the slenderness increases, because the mid-height moment at failure decreases. Equation [2.3] implies, however, that the rigidity will decrease as the slenderness increases, perhaps because it was developed entirely on statistical analyses.

Most of the proposed methods consider the influence of either the applied end eccentricity, e, or the applied axial force, C_f. Including both variables as suggested by Eq. [2.2] may significantly affect the results from a regression analysis, since they are correlated. As the normalized applied axial load, C_f / C_o, increases from 0 to 1, the maximum applied end eccentricity ratio, e/h, decreases from infinity to zero. Eq. [2.2] was developed from a parametric study treating the two variables independently, but the coefficients assigned to these variables are potentially highly correlated: there should be an unlimited number of coefficients that will fit the parametric study results with similar accuracy.

Equation [2.1] implies that increasing C_f / C_o will increase the rigidity, as shown in Figure 2.3 for various slenderness ratios, kL/r. At axial loads less than $0.02C_o$ the rigidity from Eq. [2.1] is a minimum value, which is defined by the slenderness ratio. Equation [2.1] reaches a maximum at $0.42C_o$ that is also related to the slenderness ratio. For columns with slenderness ratios exceeding 80, this maximum rigidity value is limited to two thirds of the gross rigidity, E_cI_g. Equation [2.2], contradicts Eq. [2.1] however, because it implies that the effective rigidity will reduce as the normalized applied axial load is increased.

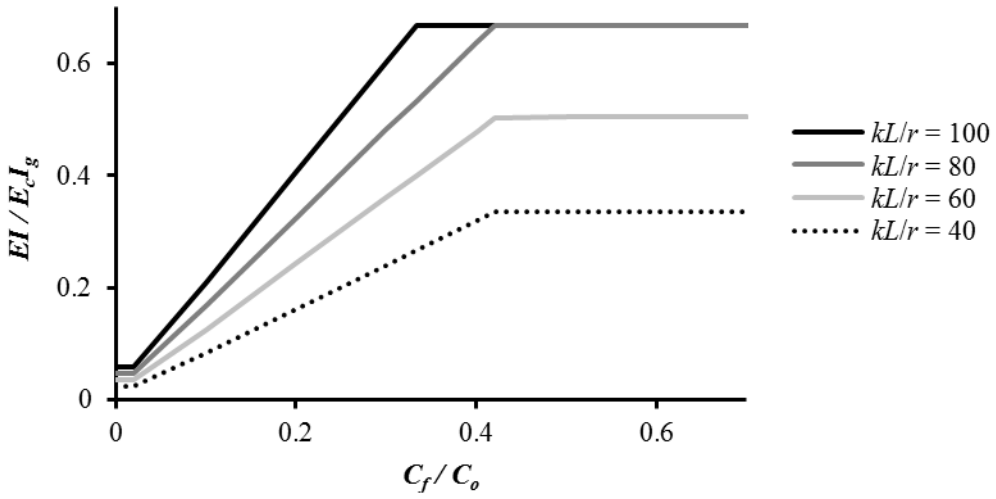

Figure 2.3: Effective rigidity according to Eq. [2.1] for short-term loading.

Equation [1.3] suggests a complex relationship between the normalized applied axial load, C_f / C_o, and the effective flexural rigidity, EI, that depends on the concrete compressive strength, f'_c, the steel-effective-depth-to-section-height ratio, d/h, and the gross reinforcement ratio, ρ_g. Figure 2.4 a) shows the variation of the secant rigidity obtained using Eq. [1.3] with the normalized applied axial load for a cross section with

f'_c = 50MPa, ρ_g= 1%, and *d*/*h* from 0.75 to 0.90. Since the top steel layer in cable-stayed bridge decks is not tied to prevent buckling, only the lower layer has been considered when computing the reinforcing ratio, ρ_g. Increasing the *d*/*h* ratio causes a slight increase in effective rigidity, as shown in Figure 2.4 a). Increasing the normalized applied axial load causes a more significant response, increasing the effective rigidity at low axial loads and decreasing it at higher loads. To further examine the influence of either the axial load or the *d*/*h* ratio on the secant rigidity, the effects of increasing these parameters on the neutral axis depth and on the cross-sectional moment resistance will be considered separately.

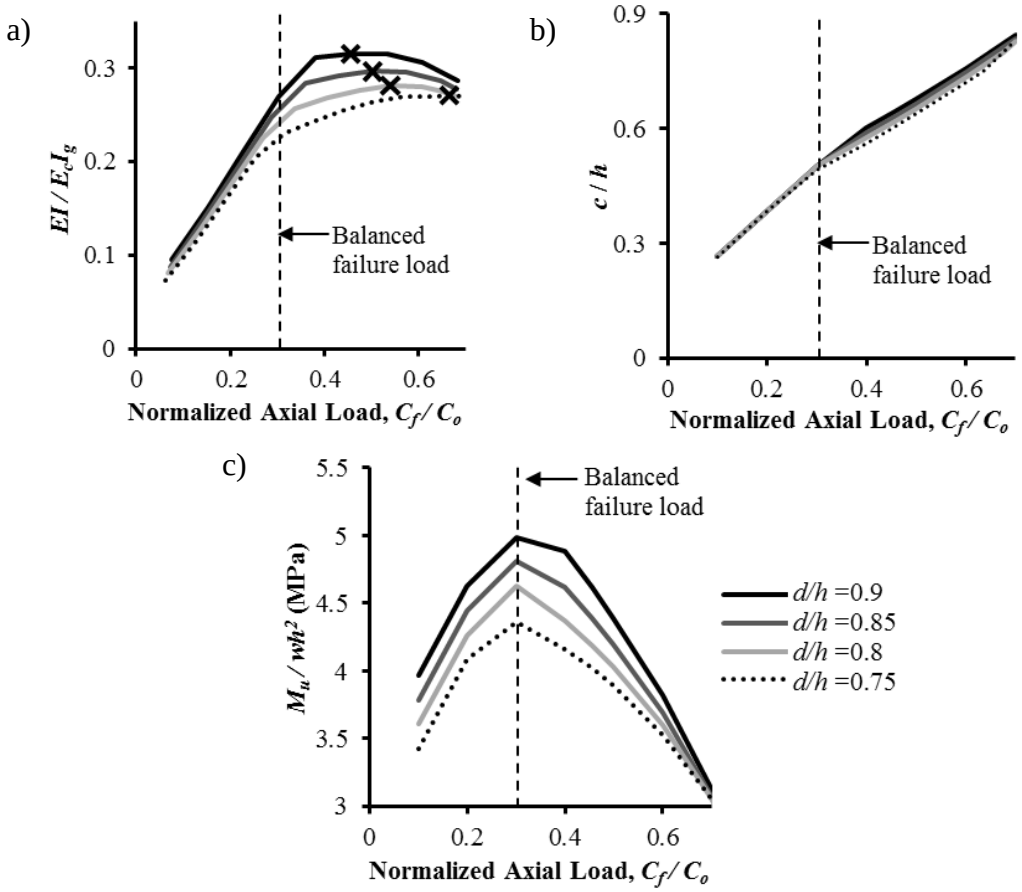

Figure 2.4: Influence of the normalized applied axial load, according to Eq. [1.3], on the: a) rigidity; b) neutral axis depth; and c) moment resistance for ρ_g = 1% and f'_c = 50MPa.

Figure 2.4 b) demonstrates the relationship between the normalized applied axial load and the neutral axis depth for various *d*/*h* ratios. For axial loads below the balanced failure load at roughly $0.3C_o$, the *d*/*h* ratio does not affect the neutral axis depth. For loads above the balanced failure load, increasing the *d*/*h* ratio slightly increases the neutral axis depth. Increasing the axial load is more significant because the neutral axis depth triples as the load is increased from $0.1C_o$ to $0.7C_o$.

The relationship between the normalized applied axial load and the moment capacity is shown in Figure 2.4 c). The moment resistance, M_u, is divided by wh^2, where *w* is the width of the member, to obtain a normalized value of the bending stress. Clearly, the moment resistance is strongly affected by both the *d*/*h* ratio and the normalized applied axial load. Increasing the *d*/*h* ratio increases the moment resistance regardless of the applied load. Increasing the applied load increases the moment resistance until the balanced failure load is reached and decreases the moment resistance once the balanced failure load is exceeded.

The maximum rigidity for the indicated range of axial loads is shown on Figure 2.4 a) by the symbol X. The peak rigidity corresponds to the axial load where the rate of increase in neutral axis depth, Figure 2.4 b), is equivalent to the rate of reduction in moment resistance, Figure 2.4 c), and therefore must occur at an axial load exceeding the balanced failure load.

Equations [2.2], [2.4], and [2.5], suggest that increasing the end eccentricity ratio, *e*/*h*, will decrease the effective rigidity. Equation [2.6] implies that the effect of the applied

eccentricity, *e*, depends on both the magnitude of the relative eccentricity factor, η_e, and the slenderness ratio, *kL*/*r*, as shown in Figure 2.5. For $\eta_e > 0.2$, increasing the applied eccentricity causes the effective rigidity to decrease for all slenderness ratios. For $\eta_e < 0.2$, increasing the applied eccentricity reduces the rigidity in members with slenderness ratios greater than 55, and increases the rigidity in members with slenderness ratios less than 55. Bonet et al. (2011) explain that when $\eta_e < 0.2$ and the slenderness is high, failure is due to instability and so increasing the slenderness while holding the eccentricity constant approaches an unstable position, so the mid-height moment at failure is reduced and the rigidity at failure increased. At low slenderness ratios, material failure occurs, so as the eccentricity reduces the section becomes more compressed and the factor α reduces to account for the difference between the actual secant elastic modulus at the applied load and the nominal tangent modulus computed using Eq. [2.6]. Since α reduces with the eccentricity only when $kL/r < 55$, it can be assumed that Bonet et al. (2011) chose a slenderness ratio of 55 to be the limit when instability failure occurs before material failure is reached, though it would seem that this limit is likely a function of other parameters as well.

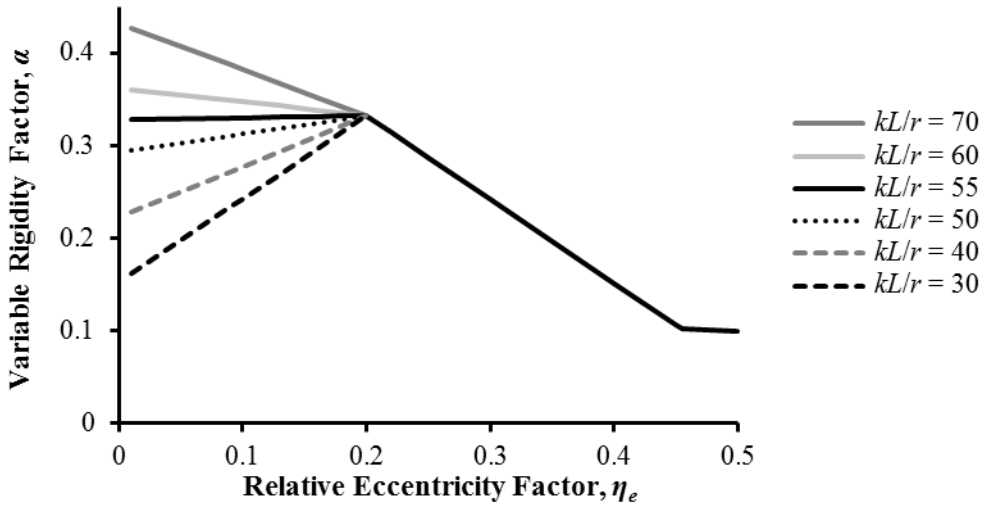

Figure 2.5: The variable rigidity factor, α, provided by Eq. [2.6] for short-term loading.

Equations [2.1], [2.6], and the method proposed by Shuraim and Naaman (2003), using Eqs. [1.3] and [2.8], explicitly account for instability failures. In contrast, Eqs. [1.8], [1.9], [2.4], and [2.5], only address material failures. Equation [1.3] provides the secant rigidity at material failure and so does not apply to instability failures. Equation [2.2] was intended to provide the secant rigidity of the cross section at service and ultimate loads. However, Eq. [2.2] can only be applied to instability failures if the maximum moment at failure is known. Equation [2.3] was derived from a statistical analysis of slender column tests reported in the literature. This equation may implicitly address instability, if some columns in the sample failed by instability, but this is not discussed and no specific approach is given for considering instability.

The equations in Table 2.2 range in sophistication from the basic Eqs. [1.8] and [1.9], to the more complicated Eqs. [2.4], [2.5], and [2.6]. However, the more complicated equations are not necessarily more accurate. Olendzki (2008) analysed experimental results reported in the literature for 180 columns that satisfied the slenderness limits of

CSA S6-06, and had compressive strengths less than 55MPa. The experimental capacities were compared to the capacities predicted using the moment magnifier equation, Eq. [1.6], with the effective rigidity provided by CSA S6-06, Eq. [1.8], and that suggested by Tikka and Mirza (2008), Eq. [2.4]. The mean value and coefficient of variation of the test-to-predicted ratios were 1.13 and 0.18, respectively, for Eq. [1.8] and 1.15 and 0.18, respectively, for Eq. [2.4]. Equation [2.4], although more complicated, was therefore slightly more conservative than and essentially as variable as Eq. [1.8]. Olendzki (2008) observes that Eq. [2.4] was derived by regression of both simulated reinforced concrete and composite column results.

2.3 CASE STUDY: VARIABILITY AMONG THE *EI* EQUATIONS PROPOSED IN THE LITERATURE

Various methods have been proposed to compute the capacity of slender columns, shown in Table 2.1. However, as shown in Table 2.2, there is limited consensus regarding which variables influence the rigidity. A simple example will be presented to demonstrate further the different outcomes obtained using these methods.

A simply supported slender column 4500mm long, 215mm thick, and 1000mm wide (kL/r = 72.5), is subjected to equal end moments, as shown in Figure 2.6 a). The concrete compressive strength, f'_c, is 55MPa and there are two layers of reinforcement centered 35mm from each face, containing 2000mm^2 of reinforcing steel (f_y = 400MPa), respectively, as shown in Figure 2.6 b). This cross section is similar to that of the deck panels near midspan of the Alex Fraser Bridge in Vancouver (CBA-Buckland & Taylor Ltd, 1983). The maximum first-order moment, M_2, that the column can resist is calculated

for axial loads, *C*, of 1000kN and 5000kN, which correspond to roughly 10% and 50% of the short column capacity, C_o = 9790kN, as shown on the cross-section interaction diagram in Figure 2.6 c). The end moments are calculated using the moment magnifier equation, Eq. [1.6], with the equivalent rigidities, *EI*, proposed in the literature, Eqs. [1.3], [1.8], [1.9], [2.1] to [2.6], and [2.8].

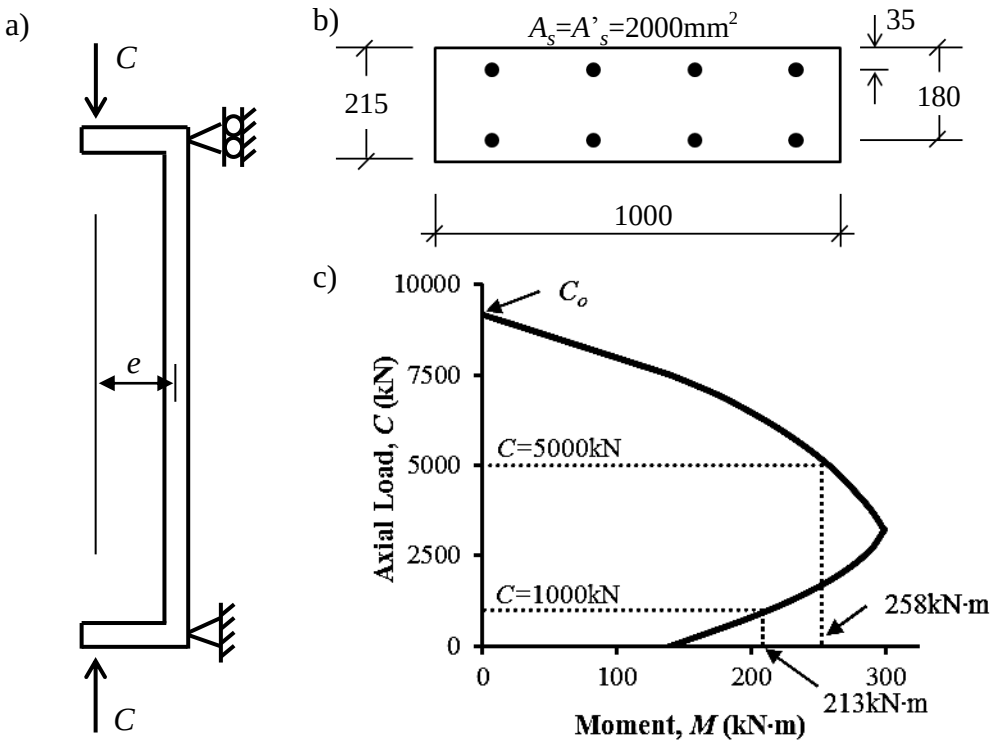

Figure 2.6: Simply supported column: a) applied loading; b) cross section; c) cross-section interaction diagram.

The following assumptions are made:

a) Resistance factors are set equal to 1.0 and only short-term loading is considered.

b) Steel is considered to only act in tension, since it is not tied to prevent buckling (Clause 8.14.4.1, CSA S6-06). This reduces the gross reinforcing ratio, ρ_g, to 0.93%. The moment of inertia of the reinforcement, I_s, therefore considers only

the bottom layer of reinforcement and is calculated about the centroid of the gross concrete section.

c) The mid-height moment is equal to the cross-section capacity, M_u, when using the moment magnifier equation, Eq. [1.6].
   - M_u = 213.1 kN·m (C = 1000kN)
   - M_u = 257.6 kN·m (C = 5000kN)

The results obtained using the proposed equations are compared to the results from a detailed computer analysis, specifically the program *CSDECK* described in Chapter 4. The analysis uses the moment-curvature relationship of the cross section to approximate the distribution of curvature along the member. The concrete stress-strain relationship proposed by Thorenfeldt et al. (1987) with the simplifications proposed by Collins and Mitchell (1990) is used to derive to moment-curvature relationship. The stress-strain relationship was derived for f'_c=55MPa and then the stress values were multiplied by 0.9 to account for the difference between the in-place strength and cylinder strength (MacGregor & Bartlett, 2000). This also reduces the modulus of elasticity by a 0.9 factor, so the modulus of elasticity used to derive the relationship was computed using Clause 8.4.1.7 of CSA S6-06 (CSA, 2006) and then increased by (1/0.9). The resulting stress-strain relationship has a peak stress of $0.9f'_c$ and an initial tangent modulus of elasticity, E_c, that equals the value computed using CSA S6-06. Figure 2.7 shows the cross-section interaction diagrams obtained from *CSDECK* and from the equivalent rectangular stress block provided in CSA S6-06: clearly the two diagrams are similar.

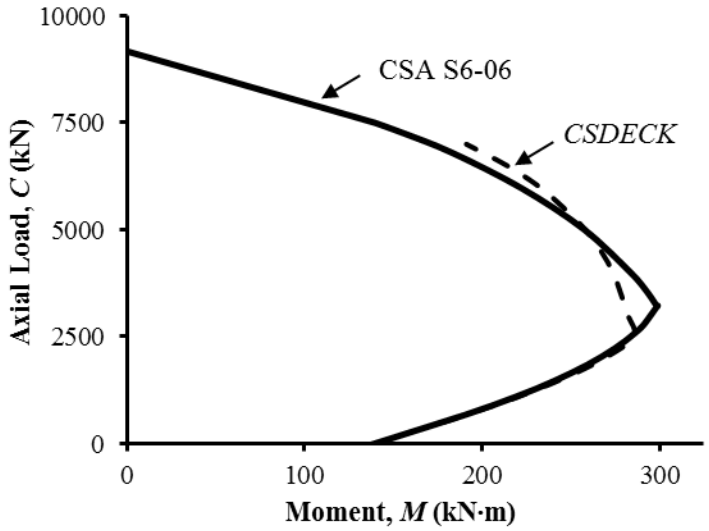

Figure 2.7: Cross-section interaction diagrams obtained using the provisions in CSA S6-06 and the program *CSDECK*.

The various methods proposed by others are considered acceptable if the predicted maximum end moment, M_2, is within 20% of the maximum end moment obtained from the *CSDECK* analysis, M_2*.

For the applied axial load of 1000kN, the failure is tension-initiated with the steel yielding before the concrete crushes. The maximum end moments capacities determined for the various proposed methods are shown in Table 2.3. The *CSDECK* analysis predicts an instability failure at the critical section where the maximum moment reaches 95% of the cross-sectional capacity, M_u , due to an applied end moment, M_2*, of 157 kN·m. The right most column in Table 2.3 shows the percent difference between the value obtained using each proposed method and the more accurate result from *CSDECK*.

Table 2.3: Maximum end moments obtained using the rigidity equations proposed in the literature for C=1000kN.

Eq. [#]	Author (year)	EI (*10^3 kN·m^2)	C_c (kN)	M_2 (kN·m)	Difference (%)
[1.8]	CSA (2006) #1	7.30	3560	153	2%
[1.9]	CSA (2006) #2	6.50	3170	146	7%
[2.1]	Nathan (1983)	4.04	1970	105	33%
[2.2]	Khuntia & Ghosh (2004)	6.84	3330	149	5%
[2.3]	Olendzki (2008)	17.2	8390	188	-20%
[2.4]	Tikka & Mirza (2008) #1	4.90	2390	124	21%
[2.5]	Tikka & Mirza (2008) #2	5.07	2470	127	19%
[2.6]	Bonet, Romero & Miguel (2011)	5.14	2510	128	18%
[1.3]	Anderson & Moustafa (1970)	3.12	1520	72.9	53%
[1.3] & [2.8]	Shuraim and Naaman (2003)	5.78	2820	137	12%
	CSDECK			157	0%

Equations [1.8] and [1.9] from CSA S6-06 accurately predicted the capacity of the column, as did Eq. [2.2], proposed by Khuntia and Ghosh (2004). Equations [2.4] and [2.5], proposed by Tikka and Mirza (2008), and Eq. [2.6], proposed by Bonet et al. (2011), underestimated the capacity by 18 to 21%. Equation [2.3], proposed by Olendzki (2008), gave the least conservative result, overestimating the capacity by 20%. The theoretical secant rigidity equation at material failure, Eq. [1.3], gave extremely conservative results, as did Eq. [2.1], proposed by Nathan (1983), underestimating the capacity by 53 and 33%, respectively. The variation of Eq. [1.3] proposed by Shuraim and Naaman (2003) improved the accuracy of Eq. [1.3] considerably, providing acceptable results within 12% of the results from *CSDECK*.

For the applied axial load of 5000kN, because the failure is compression-initiated, the concrete crushes in compression before the steel yields. The associated maximum end moments are summarized in Table 2.4. The *CSDECK* analysis computes the maximum applied end moment, M_2*, to be 114 kN·m, which causes an instability failure at the critical section where the maximum moment is 94% of the cross-section capacity. All the proposed methods produced conservative predictions. Equations [1.8] and [1.9], from CSA S6-06, and Eqs. [2.4] and [2.5], proposed by Tikka and Mirza (2008), suggest the column subjected to this axial force will buckle before any end moment is applied. Equation [2.3], proposed by Olendzki (2008), and Eq. [2.2], proposed by Khuntia and Ghosh (2004), gave the most accurate predictions, underestimating the results from *CSDECK* by only 8 and 7%, respectively. Equation [2.1] suggested by Nathan (1983), and Eq. [2.6], proposed by Bonet et al. (2011), underestimate the capacity by 20 and 26%, respectively. The theoretical equation for the secant rigidity at material failure, Eq. [1.3], underestimates the capacity by 84%. The method using Eqs. [1.3] and [2.8], proposed by Shuraim and Naaman (2003), performed better than Eq. [1.3], but is still very conservative, underestimating the capacity by 29%.

Table 2.4: Maximum end moments obtained using the rigidity equations proposed in the literature for C=5000kN.

Eq. [#]	Author (year)	EI (*10^3 kN·m^2)	C_c (kN)	M_2 (kN·m)	Difference (%)
[1.8]	CSA (2006) #1	7.30	3560	0	100%
[1.9]	CSA (2006) #2	6.50	3170	0	100%
[2.1]	Nathan (1983)	15.8	7720	90.7	20%
[2.2]	Khuntia & Ghosh (2004)	17.4	8460	105	7%
[2.3]	Olendzki (2008)	17.2	8390	104	8%
[2.4]	Tikka & Mirza (2008) #1	9.89	4820	0	100%
[2.5]	Tikka & Mirza (2008) #2	10.2	4960	0	100%
[2.6]	Bonet, Romero & Miguel (2011)	15.2	7430	84.1	26%
[1.3]	Anderson & Moustafa (1970)	11.1	5390	18.5	84%
[1.3] & [2.8]	Shuraim and Naaman (2003)	14.9	7270	80.5	29%
	CSDECK			114	0%

2.4 SUMMARY AND CONCLUSIONS

Eight different equations proposed in the literature for computing the rigidity of slender concrete beam-columns were investigated and the influence of their key variables were compared. A simple example involving a realistic cable-stayed bridge deck section and effective length was investigated to demonstrate that the methods proposed in the literature provide inconsistent results. The equations provided by CSA S6-06, Eqs. [1.8] and [1.9], gave accurate predictions of the maximum end moments in the tension-initiated-failure region, but gave unrealistic and extremely conservative estimates in the compression-initiated-failure region. Equation [2.1], suggested by Nathan (1983), consistently yielded over-conservative results. Equation [2.2], proposed by Khuntia and

Ghosh (2004), gave the most accurate results with accurate predictions at both applied axial loads. Equation [2.3], proposed by Olendzki (2008), was unconservative at the lower applied load, but gave an accurate prediction at the higher applied load. Equations [2.4] and [2.5], suggested by Tikka and Mirza (2008), and Eq. [2.6], proposed by Bonet et al. (2011), gave conservative predictions at both loads, with over-conservative predictions at the higher applied load of 5000kN. The theoretical equation for the secant rigidity at material failure, Eq. [1.3], gave extremely conservative predictions at both loads, since the rigidity is strongly influenced by the extreme fibre compression strain, ε_{cu}, and the minimum rigidity, occurring at the critical section, is assumed to apply along the entire length of the member. The method proposed by Shuraim and Naaman (2003), using variations on Eq. [1.3] and Eq. [2.8], gave a good prediction at the applied load of 1000kN, but an overly conservative prediction at the higher applied load of 5000kN.

The only noticeable trend among the proposed methods, with the exception of Eq. [2.1] proposed by Nathan (1983), is the predictions became more conservative as the applied load increased. With the exception of Eq. [2.3] (Olendzki, 2008), the proposed methods were more conservative than the CSA S6-06 equations for the tension-initiated failure case. All of the equations proposed by others yielded less conservative estimates of the rigidity for the compression-initiated failure case, though Eqs. [2.4] and [2.5] (Tikka and Mirza, 2008) still predict that the member will buckle when subjected to the applied axial load alone.

For this idealized case of equal and opposite end moments causing single curvature there is a great deal of variability among the methods proposed in the literature. Cable-stayed

bridge decks however are subjected to non-uniform local moments from traffic loads applied between floorbeams. These moments are negative above the supports and positive at midspan, so deck slabs are typically bent in triple curvature. Therefore, a more detailed investigation is warranted to determine the effect of non-uniform moment distributions.

CHAPTER 3: EFFECTIVE LENGTH OF CABLE-STAYED BRIDGE DECKS

3.1 INTRODUCTION

Equation [1.7] is given in CSA S6-06 (CSA, 2006) for computing the critical buckling load, C_c. Figure 3.1 a) shows the buckled shape of a slender cable-stayed bridge deck spanning between steel transverse floorbeams. The effective buckling length, kL, in Eq. [1.7] is the spacing between the inflection points of the buckled shape, shown in Figure 3.1 b).

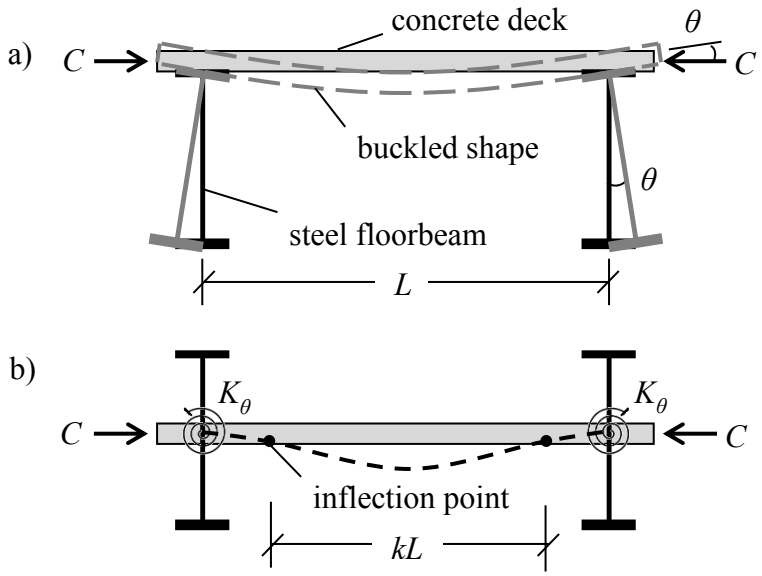

Figure 3.1: Deck slab instability: a) buckled shape; b) idealization with deck slab at floorbeam centroid.

If the deck slab is pinned at the floorbeams, its ends will be free to rotate, the distance between the inflection points will equal the floorbeam spacing, L, and the effective length factor, k, will be 1.0. If the ends of the slab are restrained from rotation, the inflection points will move inwards and the effective length will reduce, approaching a minimum value of half the floorbeam spacing (i.e., $k = 0.5$) if the ends are completely fixed.

Dimensionless ratios of relative stiffness, Ψ, can be used to obtain the effective length factor from an alignment chart (e.g., MacGregor & Bartlett, 2000) if the stiffnesses of the end restraints can be quantified. The assumption necessary for using these alignment charts is that all of the compression members buckle simultaneously. This assumption is more realistic for cable-stayed bridge decks than for columns in buildings, since the deck compression force is almost constant between adjacent floorbeams near the pylons.

Neglecting distortion and local transverse bending deformation at the web, end rotations of the deck slab must be accompanied by equal rotations of the floorbeams, as shown in Figure 3.1 a). The ends of the slab are therefore partially restrained by the rotational restraint, K_θ, of the floorbeams. However, to take advantage of this restraint the floorbeams must be designed and detailed to resist torsion. Assuming a uniform moment causing single curvature of the slab at the onset of buckling, the relative stiffness is:

$$\Psi = \frac{2\ \Sigma\left(EI / L\right)}{K_\theta} \qquad [3.1]$$

where EI is the flexural rigidity of the deck slab and L is the floorbeam spacing.

3.2 IDEALIZATION OF THE ROTATIONAL RESTRAINT OF TRANSVERSE FLOORBEAMS

The rotational restraint, K_θ, is the torque required to cause a unit rotation of the floorbeam. Assuming the floorbeams rotate about their centroid is analogous to assuming the deck slab is connected there, as shown in Figure 3.1 b). However, the deck slab is actually either shear-connected to the top flange of steel floorbeams or cast

monolithically with the web of concrete floorbeams. The significant slab axial stiffness causes negligible longitudinal deflection at the midpoint of the deck due to rotation of the floorbeams. The partial restraint of the eccentric deck slab is idealized in Figure 3.2 as a counteracting force, P_e, which causes the floorbeam centroid to deflect a horizontal distance, Δ_e, as the member rotates. Assuming the rotation, θ, is small, $\Delta_e \approx \theta(\bar{y} - h_s/2)$, where $\bar{y}$ is the distance from the top of the slab to the centroid and h_s is the thickness of the slab. The rotational restraint, K_θ, is therefore a function of the floorbeam torsional rigidity, GJ, its y-axis bending rigidity, EI_y, and the location of its centroid, $\bar{y}$.

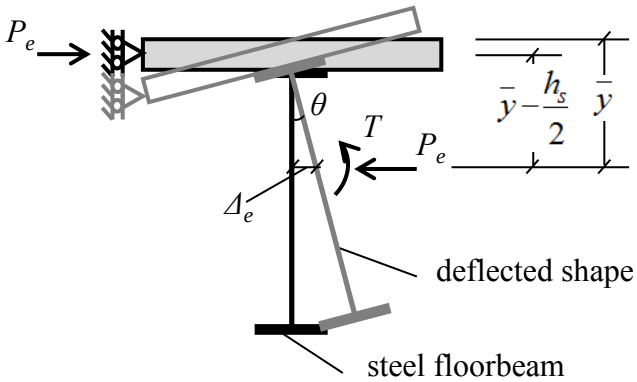

Figure 3.2: Horizontal deflection of floorbeam centroid.

3.3 APPROXIMATE ANALYTICAL EQUATIONS FOR THE ROTATIONAL RESTRAINT OF TRANSVERSE FLOORBEAMS

The rotational restraint, K_θ, of a linear-elastic member with fixed ends rotating about its centroid due to an applied point torque is:

[3.2] $$K_\theta = \frac{T}{\theta} = \frac{GJs}{a(s-a)}$$

where θ is the rotation at the point of application of the point torque, *T*, at a distance, *a*, from the support. The shear modulus is *G*, *J* is the St. Venant torsional constant, and *s* is the floorbeam length.

If the eccentricity of the deck slab is considered, the force, P_e, shown in Figure 3.2, causes a restraining torque, T_e, equivalent to the product of P_e and $\bar{y} - h_s/2$. For small rotations, the restraint provided by the eccentric deck slab, K_e, can be computed as (see Appendix B for derivation):

$$[3.3] \quad K_e = \frac{T_e}{\theta} = \frac{3EI_y s^3 \left(\bar{y} - h_s/2\right)^2}{a^3 \left(s-a\right)^3}$$

The total rotational restraint, K_θ, is sum of the restraint provided by the torsional stiffness of the floorbeam, Eq. [3.2], and that provided by the eccentricity of the deck, Eq. [3.3]:

$$[3.4] \quad K_\theta = \frac{GJs}{a\left(s-a\right)} + \frac{3EI_y s^3 \left(\bar{y} - h_s/2\right)^2}{a^3 \left(s-a\right)^3}$$

Figure 3.3 shows a width of slab, *w*, spanning between transverse floorbeams. Using Eq. [3.4] to compute the rotational restraint of a floorbeam subjected to a point torque is analogous to assuming the width of the deck slab, *w*, is only 1m. This assumption yields small values for the relative stiffness, Ψ, from Eq. [3.1], since the entire floorbeam contributes to K_θ but only 1m width of deck contributes to the deck rigidity, *EI*. Since the

effective length factor reduces with Ψ, this yields very unconservative estimates of k and so Eq. [3.4] must be revised to suit more realistic loading conditions.

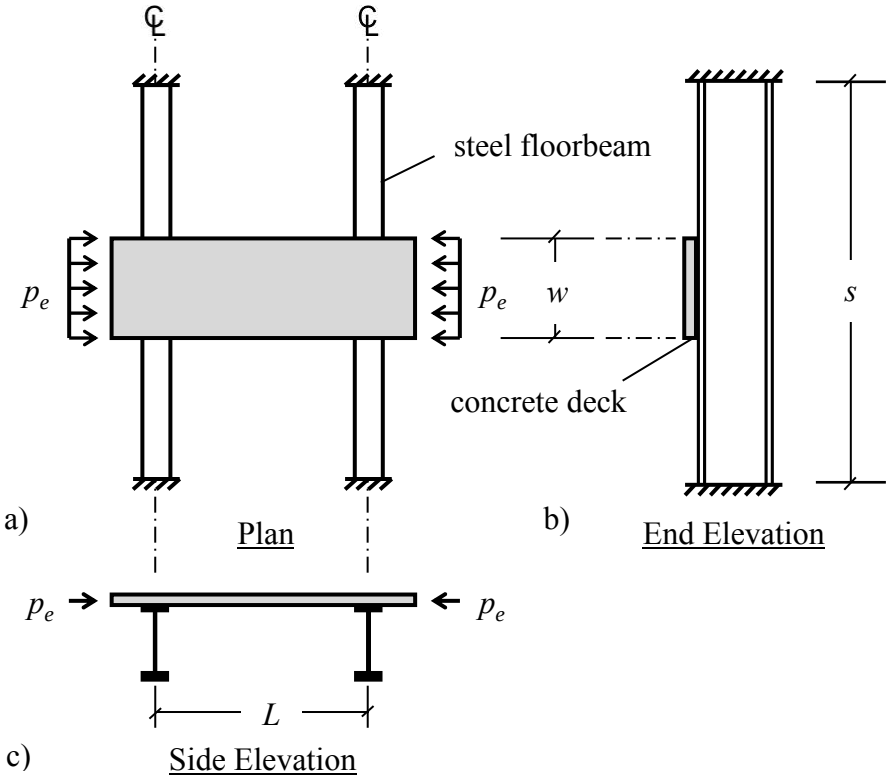

Figure 3.3: Concrete deck on steel floorbeams: a) plan; b) end elevation; and c) side elevation.

If a uniform torque is applied along a width greater than 1m, the eccentricity of the deck slab can be idealized as a uniformly distributed restraint, p_e, as shown in Figure 3.3. For the remainder of this thesis, it will be assumed that the uniform torque is applied along a width of slab equal to half the length of the floorbeam (i.e. $w = s/2$), centered at the floorbeam midspan.

Equations [3.5] and [3.6], shown in Table 3.1 (see Appendix B for derivation), yield the rotational restraint, k_θ, at the floorbeam midspan and quarter-spans, respectively,

provided by a floorbeam with fixed ends to a slab subjected to uniform torque applied between the quarter points. They are derived assuming that the ends of the floorbeams are fixed against y-axis bending. This assumption is appropriate for bridges with concrete floorbeams, but not for bridges with steel floorbeams, which are more likely pin ended. The rotational restraint provided by a steel floorbeam is therefore reduced, as given by Eqs. [3.7] and [3.8] at the quarter-span and midspan, respectively, of the floorbeam (see Appendix B for derivation). The total rotational restraint, K_θ, is the product of the uniform restraint, k_θ, and the length loaded length (i.e. $K_\theta = k_\theta(s/2)$).

Table 3.1: Rotational restraint provided by floorbeams.

Floorbeam End Restraints	**Rotational Restraint, k_θ**	
	Quarter-span	**Midspan**
Fixed against all translations & rotations	[3.5] $\frac{16GJ}{s^2}+\frac{6144EI_y\left(\bar{y}-h_s/2\right)^2}{7s^4}$	[3.6] $\frac{32GJ}{3s^2}+\frac{6144EI_y\left(\bar{y}-h_s/2\right)^2}{13s^4}$
Fixed against all translations & torsional rotation	[3.7] $\frac{16GJ}{s^2}+\frac{768EI_y\left(\bar{y}-h_s/2\right)^2}{5s^4}$	[3.8] $\frac{32GJ}{3s^2}+\frac{6144EI_y\left(\bar{y}-h_s/2\right)^2}{57s^4}$

3.4 VALIDATION USING SAP2000

Equation [3.4] was validated by performing a linear-elastic static analysis in SAP2000 (Computers & Structures Inc., 2011). A solid steel bar 100mm in diameter, spanning 500mm between fixed supports was chosen so the contribution of the rotational restraint provided by the eccentric deck slab, K_e, would be a significant portion of the total restraint, K_θ. The bar was modelled as four frame elements 125mm long. To simulate the effect of the eccentric deck slab, the rigid link shown in Figure 3.4 a) connected the

centroid of the frame element to a roller support at the top of the section. Figure 3.4 b) demonstrates the effect of this support, forcing the centroid to deflect as the member rotates.

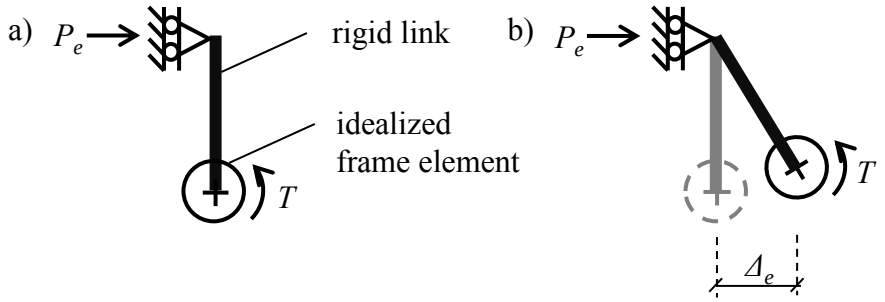

Figure 3.4: Model specimen: a) cross section showing rigid link connecting the centroid to a roller; b) deflection of the centroid.

Equation [3.4] was used to predict the rotation that would occur due to a point torque applied at both the midspan and quarter-span of the member. Neglecting shear deformations, the SAP2000 model predicted the identical rotations as Eq. [3.4] for a 1kN·m torque applied at either location.

A similar linear-elastic static analysis was performed to validate Eqs. [3.5] and [3.6]. The same section, spanning 500mm between fixed supports was idealized as 100 frame elements, each 5mm long. A uniformly distributed torque of 4kN·m/m was applied between the quarter points. Rigid links and roller supports, as shown in Figure 3.4, were spaced at 5mm between the quarter points to simulate the eccentricity of the deck slab.

Ignoring shear deformations, the rotation at the quarter-span predicted using the SAP2000 model was 7% less than predicted using Eq. [3.5] and the rotation at midspan

was 1% less than predicted using Eq. [3.6]. The derivations of Eqs. [3.5] and [3.6] assume the eccentric deck slab provides a uniformly distributed restraint, p_e, as shown in Figure 3.3. Figure 3.5 shows the reactions at the ends of the rigid links, which are not uniformly distributed, but instead are greater near the quarter points than at midspan. The links at quarter-spans partially restrain the rotation of the central region, so the restraint provided at the midspan is less.

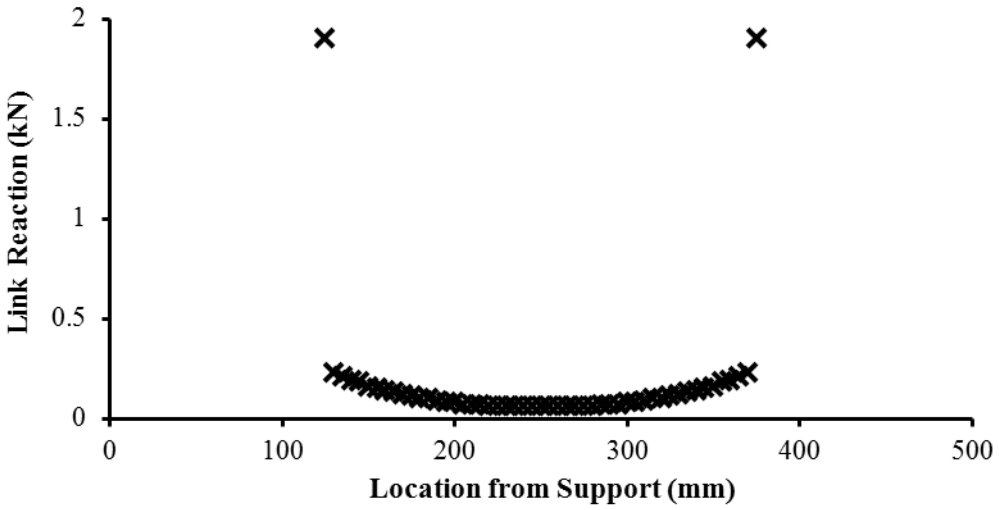

Figure 3.5: Reactions at link supports in SAP2000 model.

The SAP2000 model was then modified to check Eqs. [3.7] and [3.8] by changing the support conditions to prevent only torsional rotations. This change causes the deflected shape to resemble that of a pin-ended member when bending about the y-axis, which is more representative of the behaviour of steel floorbeams. Ignoring shear deformations, the rotations at the quarter-spans predicted by the SAP2000 model were 2% larger than predicted by Eq. [3.7] and the associated midspan rotation was 1% lower than predicted by Eq. [3.8]. These small discrepancies can again be attributed to the assumed uniformly

distributed restraint of the deck slab, whereas the actual restraint is not uniform. The equations shown in Table 3.1 were therefore deemed sufficiently accurate to quantify the rotational restraint provided by the floorbeams.

3.5 CASE STUDIES: THE EFFECTIVE LENGTH OF DECK SLABS WITH STEEL AND CONCRETE FLOORBEAMS

The steel plate girders in the Alex Fraser Bridge in Vancouver and the concrete T-beams in the Talmadge Memorial Bridge in Savannah, Georgia, were chosen as typical examples of transverse floorbeams in cable-stayed bridges. Figure 3.6 a) shows the typical cross-section dimensions of the 28m long floorbeams in the Alex Fraser Bridge, and Figure 3.6 b) shows approximate dimensions of the 21.5m long T-shaped floorbeams in the Talmadge Bridge. The typical floorbeam spacing is 4.5m for the steel girders in the Alex Fraser Bridge and 8.61m for the concrete T-beams in the Talmadge Memorial Bridge.

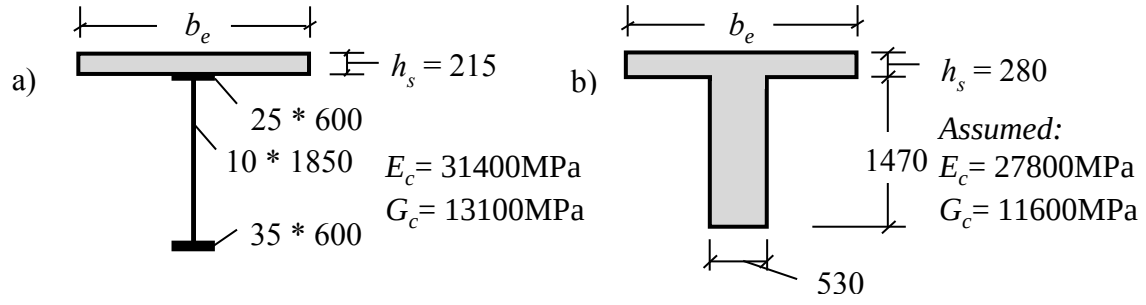

Figure 3.6: Typical floorbeam cross sections: a) steel; b) concrete (dimensions in mm).

To determine the floorbeam cross-sectional properties, an effective width of slab, b_e, that contributes to the rotational restraint of the floorbeams must be assumed. The effective width equation in Clause 5.8.2.1 of CSA S6-06 (CSA, 2006) is intended to account for

shear lag in both composite and concrete T-beams subjected to strong-axis bending. Applied to the floorbeams in the Alex Fraser Bridge it indicates that the full width of slab is effective (i.e. b_e = 4.5m). Therefore, this equation provides an upper bound for determining the sectional properties of floorbeams.

Since Clause 5.8.2.1 was not intended to determine the torsional constant, *J*, it may be unconservative to assume the full width of deck is effective at restraining rotation. As a lower bound for steel floorbeams it will be assumed that only half of the deck slab width, (i.e., $b_e/2$), effectively resists rotation.

Clause 13.8.2.7 of CSA A23.3-04 (CSA, 2004) quantifies the effective slab width for computing the torsional constant, *J*, of T-beams in two-way slab systems. These provisions are therefore assumed to provide a lower bound for calculating the sectional properties of concrete floorbeams.

Hsu (1968) subjected a member with moderate torsional reinforcement to pure torsion to study the effect of torsional cracking. Immediately after cracking he observed that the torsional stiffness, *GJ*, reduced to 20% of the uncracked value. Thus in deriving the lower bound for determining the sectional properties, the torsional constant, *J*, will be reduced to 20% of the uncracked value.

Table 3.2 shows the resulting upper- and lower-bound cross-sectional properties of the floorbeams investigated. The symbols UB_S and LB_S represent the upper- and lower-bound values for steel floorbeams, respectively, and UB_C and LB_C are the upper- and lower-

bound values for concrete floorbeams. To reiterate: the upper-bound values are computed assuming the maximum width of slab, from Cl. 5.8.2.1 of CSA S6-06 (CSA, 2006), is effective at resisting rotation and the concrete is uncracked in torsion. The lower-bound properties for steel floorbeams were computed assuming half of the available deck slab effectively resists rotation and the deck slab is cracked in torsion. The lower-bound properties for the concrete floorbeams were computed using CSA A23.3-04 (CSA, 2004) to determine the effective slab width and also assume the concrete is cracked in torsion.

Table 3.2: Upper- and lower-bound cross-sectional properties of steel and concrete floorbeams.

Property	**Steel (Alex Fraser)**		**Concrete (Talmadge)**		$\frac{UB_C}{UB_S}$	$\frac{LB_C}{LB_S}$
	UB_S	LB_S	UB_C	LB_C		
b_e (m)	4.50	2.25	6.44	2.77	1.43	1.23
EI_x ($*10^6$ kN·m^2)	18.3	15.9	15.8	12.3	0.87	0.77
EI_y ($*10^6$ kN·m^2)	51.5	6.62	174	14.3	3.38	2.16
GJ ($*10^4$ kN·m^2)	19.0	1.93	129	19.5	6.76	10.1

The x-axis bending rigidity, EI_x, of concrete floorbeams is 13 to 23% smaller than that of steel floorbeams. The y-axis bending rigidity of concrete floorbeams, EI_y, is 2.2 to 3.4 times larger than that of steel floorbeams, because the deck slab is 30% thicker and the effective slab width is from 23 to 43% greater. However, the torsional rigidity, GJ, of the concrete floorbeams exceeds that of the steel floorbeams by a factor of 6.8 to 10, due to the different deck slab dimensions, and the inefficiency of thin steel plate girder elements in resisting St. Venant torsion.

Table 3.3 shows the upper- and lower-bound rotational restraints, as computed using Eqs. [3.5] and [3.6] for concrete floorbeams and Eqs. [3.7] and [3.8] for steel floorbeams. Table 3.3 also shows the increase in rotational restraint obtained by accounting for the eccentricity of the deck slab. The contribution of the rotational restraint that is due to the eccentric deck slab, K_e, corresponds to the second term in Eqs. [3.5] to [3.8]. The contribution of the eccentric deck slab is significant for the bridge with steel floorbeams, representing a minimum of 24% of the total rotational restraint, K_θ. The contribution is greater for the bridge with the concrete floorbeams, representing at least 47% of K_θ.

Table 3.3: Rotational restraint bounds for bridges with steel and concrete floorbeams.

	Steel (Alex Fraser)		**Concrete (Talmadge)**	
	K_θ (*10^4 kN·m/rad)	K_e/K_θ	K_θ (*10^4 kN·m/rad)	K_e/K_θ
Upper bound at midspan	4.81	0.25	60.7	0.47
Lower bound at midspan	0.75	0.51	11.4	0.57
Upper bound at quarter-span	7.13	0.24	101	0.53
Lower bound at quarter-span	1.10	0.50	19.4	0.63

The results in Table 3.3 were used in Eq. [3.1] to determine the relative stiffness ratio, Ψ, and a range of effective length factors, k, were obtained using an alignment chart (e.g., MacGregor & Bartlett, 2000). Figure 3.7 shows the approximate ranges of effective length factors for concrete cable-stayed bridge decks with steel or concrete transverse floorbeams. The vertical axis shows the effective length factor, k, of the deck slab, which ranges from 0.5 to 1.0. An effective length factor, k, of 0.5 corresponds to a deck slab

spanning between floorbeams with infinite rotational restraint (fixed), while k =1.0 corresponds to a slab spanning between floorbeams with no rotational restraint (pinned).

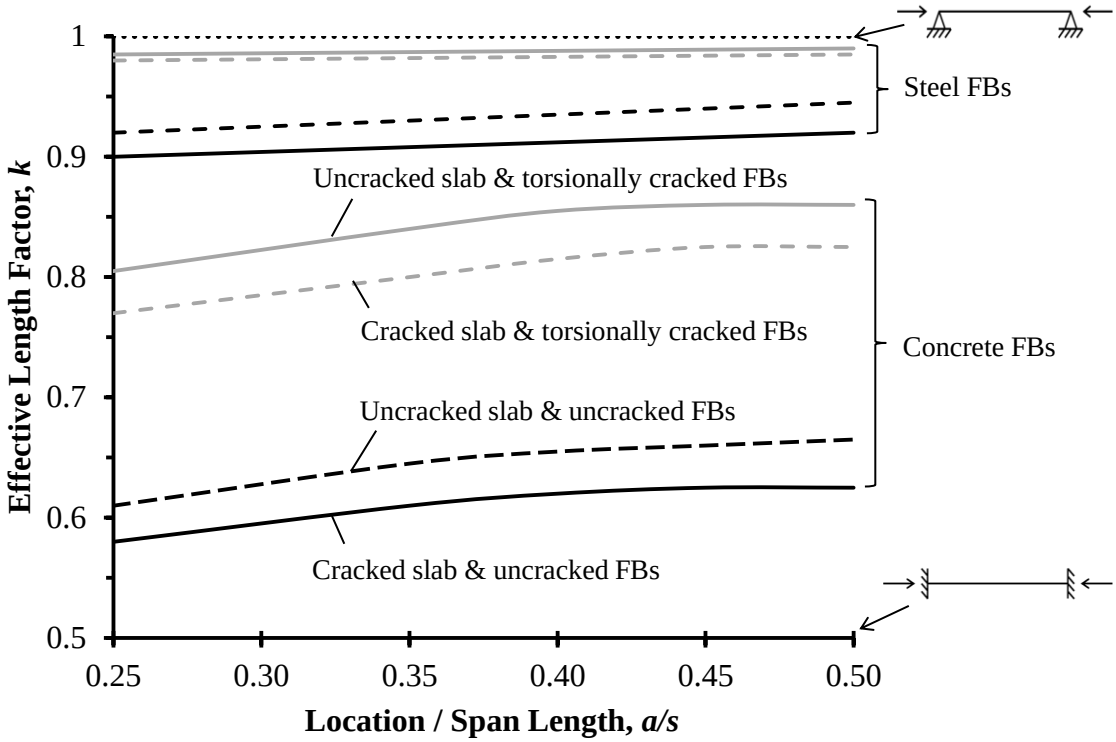

Figure 3.7: Effective length factors for cable-stayed bridge decks.

The lines for steel floorbeams in Figure 3.7 are linear because they connect only two data points, one at the quarter-span computed using Eq. [3.7] and one at midspan computed using Eq. [3.8]. The lines for concrete floorbeams are not linear since they represent several data points from the quarter-span to midspan, computed using additional equations derived using the methodology outlined in Appendix B.

The lower-bound estimates of the effective length factor, shown by the black lines in Figure 3.7, were obtained using the upper-bound rotational restraints from Table 3.3,

which were computed assuming the floorbeams remain uncracked in torsion. The grey lines correspond to the upper-bound estimates of *k* and were obtained assuming the concrete portions of the floorbeams crack in torsion. The solid black lines provide the lowest estimates of *k* by considering the concrete portions of the floorbeams uncracked in torsion and taking the flexural rigidity, *EI*, of the deck slab in Eq. [3.1] as 70% of the uncracked rigidity, E_cI_g, as suggested by CSA A23.3-04 (CSA, 2004) to account for non-linear responses in columns. The solid grey lines provide conservative estimates of *k*: they are derived assuming the concrete portion of the floorbeams to be cracked in torsion while the deck slab remains uncracked in flexure. A more appropriate range of *k* is bounded by the grey and black dashed lines: the grey dashed lines are computed assuming that the deck slab is cracked in flexure when the floorbeams are cracked in torsion and the black dashed lines are computed assuming the floorbeams are uncracked in both flexure and torsion.

The lowest value of *k* for a concrete deck slab supported by steel floorbeams is 0.90 at the quarter-span when the entire uncracked concrete slab is assumed effective in torsion but cracks in flexure. These assumptions are unconservative, so steel floorbeams seem incapable of reducing the effective length factor below 0.90. The more appropriate range of *k* for concrete decks on steel floorbeams ranges from a minimum of 0.92 at the quarter-span to a maximum of 0.98 at midspan.

The lowest *k* value for concrete deck slabs supported by concrete floorbeams is 0.58 at the quarter-span. This value corresponds to a 6.44m width of uncracked concrete deck resisting rotation and the slab cracks in flexure. The highest *k* value is 0.86 at midspan,

which corresponds to a 2.77m width of cracked deck effectively resisting rotation while the slab remains uncracked in flexure. However, the Talmadge Memorial Bridge concrete floorbeams are longitudinally post-tensioned and so are unlikely to crack in torsion. The grey lines are therefore conservative and so the rotational restraint provided by concrete floorbeams can reduce the slab effective length factor to less than 0.9. The more practical range of *k*, neglecting torsional cracking, ranges from 0.61 at the quarter-span to 0.75 at midspan.

The flexural stiffness, EI/L, is significantly smaller for the slab on concrete floorbeams since the floorbeam spacing, *L*, is larger. The concrete floorbeams are also significantly shorter than the steel floorbeams, so the rotational restraint they provide is higher. The relative stiffness ratio, Ψ, and effective length factor, *k*, will therefore be smaller for the concrete floorbeam case, since the EI/L term in Eq. [3.1] is smaller and the K_θ term is larger. If the concrete floorbeam spacing is reduced to 4.5m and the length is increased to 28m, the EI/L term for the concrete floorbeam case is almost twice that for the steel floorbeam case, so any difference in *k* values reflects the increased rotational restraint of concrete floorbeams. For these dimensions, the bounds of *k* range from 0.77 at the quarter-span to 0.95 at midspan and the more appropriate values of *k*, neglecting torsional cracking, are all less than 0.89. Thus, although the dimensional changes significantly increased effective length factors for the concrete case, the minimum rotational restraint provided by the concrete floorbeam is still three times that of the maximum rotational restraint of steel floorbeams, if torsional cracking is prevented.

The eccentricity of the deck slab increases the rotational restraint significantly, but has a lesser influence on the effective length factor, *k*. If the eccentricity of the slab is ignored the *k* values for slabs supported by steel floorbeams range from 0.92 to 0.99 instead of 0.90 to 0.99. For slabs supported by concrete floorbeams *k* ranges from 0.65 to 0.93 if the eccentricity of the deck slab is neglected, compared to 0.58 to 0.86 when it is considered. Therefore, neglecting the eccentricity of the slab reduces the rotational restraint provided by concrete floorbeams by a factor of 1.9, but only increases the effective length factor by 12%. The small influence is due to the relationship between *k* and the relative stiffness, Ψ, on the alignment chart. The relative stiffness can range from 0 for fixed end supports to infinity for a pinned supports, while the effective length factor only ranges from 0.5 to 1.0 for these same support conditions.

3.6 SUMMARY AND CONCLUSIONS

Floorbeams provide both vertical and rotational restraints to slender concrete cable-stayed bridge decks. The effectiveness of the rotational restraint provided is a function of the torsional rigidity of the floorbeam, *GJ*, its weak-axis bending rigidity, EI_y, and the location of the floorbeam centroid, $\bar{y}$. Idealizing the restraint of an eccentric deck slab as a uniformly distributed force allows the rotational restraint of floorbeams to be quantified so that the effective length factor, *k*, can be determined. Calculations have been carried out for the steel floorbeams of the Alex Fraser Bridge and the concrete floorbeams of the Talmadge Memorial Bridge.

The eccentricity of the deck slab can markedly increase the rotational restraint provided by the floorbeams. This contribution represents at least 24% and 47% of the total rotational restraint provided by the steel and concrete floorbeams investigated, respectively.

The effective length factor, *k*, approaches 1.0 for the case of the deck slab supported by steel floorbeams and is significantly less than 0.90 for the case of the slab supported by concrete floorbeams, typically ranging from 0.6 to 0.85.

The eccentricity of the deck slab has a negligible influence on *k* for the case of the deck supported by steel floorbeams, and only slightly influences *k* for the case of the deck supported by concrete floorbeams. While the eccentricity of the slab doubled the rotational restraint of concrete floorbeams it only decreased *k* by a maximum of 11%. Therefore, neglecting the eccentricity of the deck slab provides a reasonable quantification of the rotational restraint of floorbeams, for the purpose of determining the effective length factor of cable-stayed bridge decks.

CHAPTER 4: SECOND-ORDER ANALYSIS OF CABLE-STAYED BRIDGE DECKS WITH NON-UNIFORM PRIMARY MOMENT DIAGRAMS

4.1 IDEALIZED STRUCTURE

Second-order analysis of a cable-stayed bridge deck slab requires a rational method for computing the deflection due to vertical loads and the resulting second-order bending moments. Realistic support conditions must be considered, including the flexural stiffness of the adjacent spans and the rotational restraint provided by the transverse floorbeams.

In this chapter, the interior span of the idealized three-span deck system shown in Figure 4.1 will be analysed for first- and second-order moments. The compression force, C, is constant in all spans and a single vertical point load, P, is applied at the middle of the interior span. The rotational restraint provided by the transverse floorbeams, K_θ, is represented by rotational springs at both interior supports. The exterior supports of the adjacent spans are assumed to be pinned. Preliminary analyses were also conducted using a five-span model, with the centre span loaded, and differences of the linear-elastic moments from those in the three-span model were negligible.

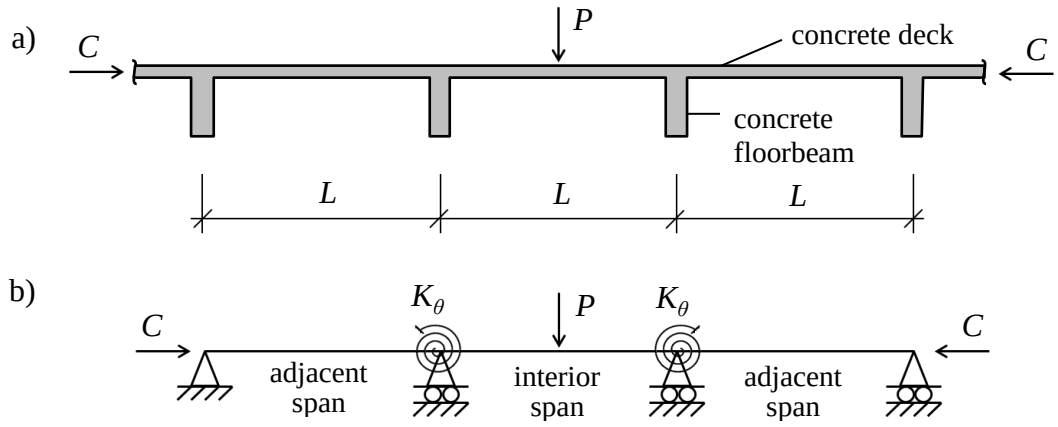

Figure 4.1: Cable-stayed bridge deck: a) cross section; b) idealized.

The deck slab shown in Figure 4.1 b) is assumed to bend in one direction only. This is equivalent to treating the slab as a strip of unit width cut along the length of the bridge. Two-way behaviour caused by the slab deflecting between the longitudinal girders is neglected, so the strip analysis provides a conservative approximation of the true behaviour. Obviously the error in the approximation will increase as the ratio of the floorbeam length to floorbeam spacing, *s*/*L*, reduces. For typical values of this ratio greater than 2, it is assumed that strip analysis provides an acceptable approximation.

4.2 MOMENT-CURVATURE RELATIONSHIP

Computation of the deflected shape of a member requires the curvature distribution along its length. The curvature at any point along a cable-stayed bridge deck can be obtained from the moment-curvature relationship derived for the given applied axial force, *C*.

A common method for computing moment-curvature relationships (e.g., Nathan, 1985, and Salonga, 2010) requires computing contours of equal curvature for the cross section, as shown in Figure 4.2 a), and then deriving the moment-curvature relationship for a given axial load by interpolation from these contours, as shown in Figure 4.2 b).

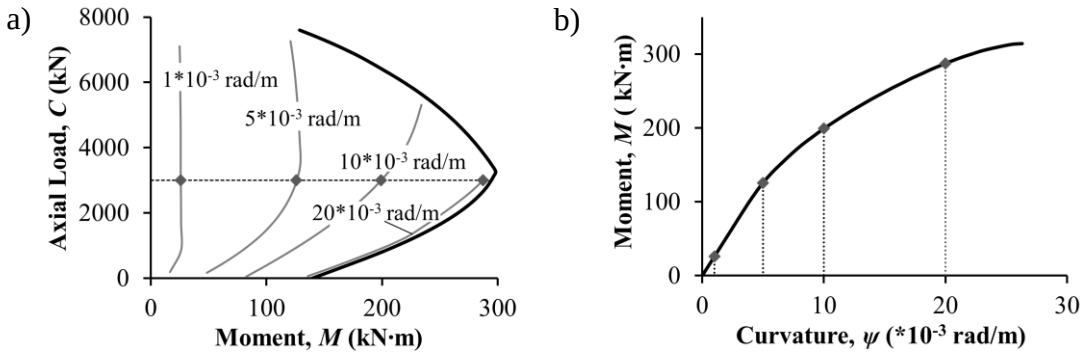

Figure 4.2: a) Curvature contours; b) moment-curvature relationship for *C* = 3000kN.

To compute curvature contours that account for the nonlinear stress-strain behaviour of concrete in compression, Nathan (1985) suggests the following five-step procedure:

1. Discretize the cross section into thin horizontal layers and compute the distance, y, from the centroid of each layer to the extreme compression fibre.

2. Compute the strain at the centroid of each layer, $\varepsilon(y)$, for given values of curvature, ψ, and extreme compression fibre strain, ε_c, as:

[4.1] $$\varepsilon(y) = \varepsilon_c - \psi y$$

where positive strains indicate compression.

3. Determine the stress at the centroid of each layer using a realistic stress-strain relationship.

4. Compute the force and moment from each layer, assuming the stress in each layer is constant.

5. Determine the corresponding applied axial load and bending moment using the fundamental equations of force and moment equilibrium.

A full contour can be computed for a given value of curvature, ψ, by incrementing the extreme compression fibre strain, ε_c, from 0 to 0.0035, the ultimate value specified in

CSA S6-06 (CSA, 2006), and applying Steps 1 to 5 to compute the axial load and moment for each increment. The maximum possible curvature occurs at material failure when the applied axial load, *C*, is zero. Once multiple curvature contours are computed, the moment-curvature relationship can be interpolated from these contours for any applied axial load, *C*, as shown in Figure 4.2.

To obtain the full moment-curvature relationship, this procedure must be performed twice, once with the extreme compression fiber at the top face, for positive moments and curvatures, and then again with the extreme compression fiber at the bottom face, for negative moments and curvatures.

4.3 MOMENT DISTRIBUTION AT SUPPORTS

Vertical loads applied to the deck slab will create local negative moments at each transverse floorbeam, due to the rotational restraint provided by the floorbeams and the flexural stiffness of the adjacent slabs. These negative moments can be computed efficiently using the Force Method of analysis (e.g., Hibbeler, 2009). All redundancies are removed initially to obtain a statically determinate primary structure. For example, for the idealized structure in Figure 4.3 a), hinges are assumed in the deck slab at each interior support to define the primary structure. For the applied vertical load, the bending moment is derived and, using the moment-curvature relationship for the given applied axial load, the curvature distribution along the length of the member is computed. The deflected shape, including primary end rotations, θ_L and θ_R in Figure 4.3 b), are computed by numerically integrating the primary curvatures for discrete segments of the member

(e.g. Hibbeler, 2009) while satisfying the displacement boundary conditions at the supports.

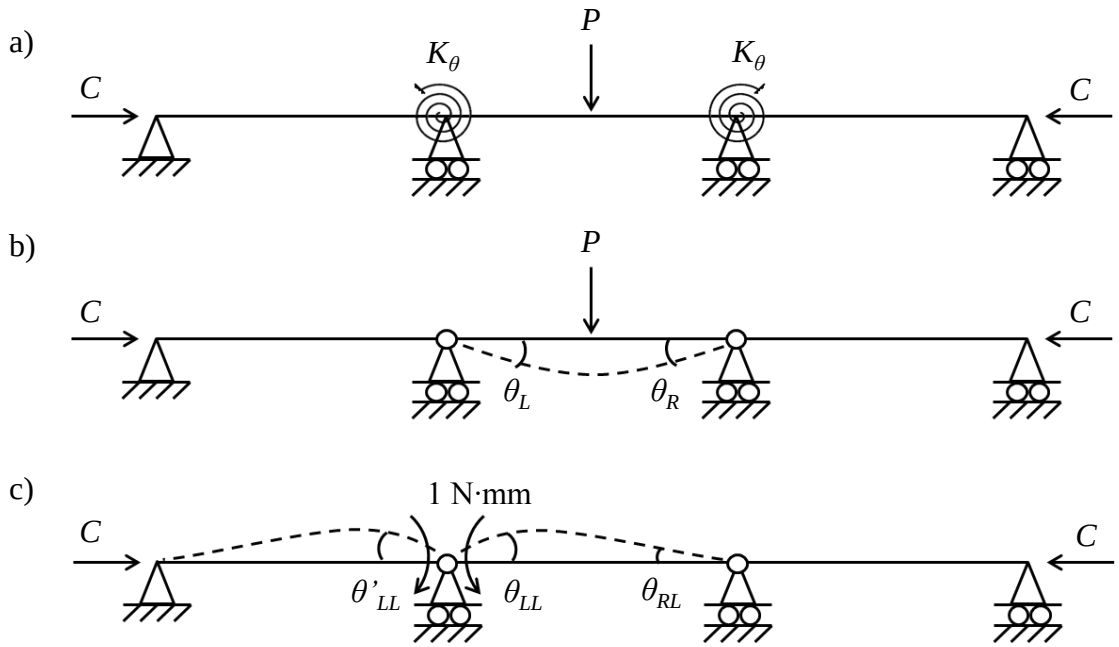

Figure 4.3: The force method of analysis, a) actual structure; b) primary structure; c) redundant moment at the left interior support.

A unit moment of 1N·mm, shown at the left interior support in Figure 4.3 c), is then applied at each location where a redundancy was removed to determine flexibility coefficients f_{LL}, f_{RR}, f_{LR}, and f_{RL}:

[4.2] $$f_{LL} = \theta_{LL} + \theta'_{LL} = \theta_{LL} + \frac{1}{\frac{3\gamma_L E_c I_g}{L} + K_\theta}$$

[4.3] $$f_{RR} = \theta_{RR} + \theta'_{RR} = \theta_{RR} + \frac{1}{\frac{3\gamma_R E_c I_g}{L} + K_\theta}$$

[4.4] $$f_{LR} = f_{RL} = \theta_{RL}$$

where θ_{LL}, θ'_{LL}, and θ_{RL} are the rotations at the left end of the interior span, the right end of the left adjacent span, and the right end of the interior span, respectively, due to the unit moment at the left interior support. Similarly, θ_{RR} and θ'_{RR} are the rotations of the right end of the interior span and the left end of the right adjacent span, respectively, due to a unit moment at the right interior support. In these equations, L is the span length, EI_g is the gross rigidity of the deck slab, and K_θ is the rotational restraint provided the floorbeams.

The rotations at the ends of the interior span, θ_{LL}, θ_{RR}, and θ_{RL}, can be computed by numerically integrating the curvatures due to the unit moment at either support for discrete segments of the interior span. However, the curvature of each segment must be obtained by dividing average moment in the segment, due to the unit moment at the support, by the average rigidity, EI. Initially, this rigidity can be computed as the secant rigidity obtained from the moment-curvature relationship for the average primary moment, computed by analysing the primary structure in Figure 4.3 b).

The factors γ_L and γ_R account primarily for geometric nonlinearities in the adjacent spans: since the moments in these adjacent spans are lower than those in the interior span, their stiffnesses will approach the uncracked stiffness so material nonlinearities will be negligible. However, the compression force will cause second-order moments in the adjacent spans that will increase their deflection, causing more rotation at the floorbeam

supports. Assuming a linear-elastic response, Przemieniecki (1968) gives a geometric stiffness matrix for a 2D beam element that accounts for geometric nonlinearities. The corresponding flexural stiffness, k_G, at one end of a simply supported compression member is:

[4.5] $$k_G = \frac{4E_cI_g}{L} - \frac{2CL}{15} - \frac{(2E_cI_g / L + CL/30)^2}{(4E_cI_g / L - 2CL/15)}$$

where the applied axial load, C, is positive in compression. Using Eq. [4.5] to account for the geometric nonlinearities in the adjacent spans, the modification factors can be computed as:

[4.6] $$\gamma_L = \frac{k_{GL}}{3E_cI_g / L}$$

and

[4.7] $$\gamma_R = \frac{k_{GR}}{3E_cI_g / L}$$

where k_{GL} and k_{GR} are the flexural stiffnesses of the left and right adjacent spans, respectively, computed using Eq. [4.5]. Once all flexibility coefficients have been determined, the support moments can be found by solving the following two equations simultaneously for the moments at the left and right supports, M_L and M_R:

[4.8] $$0 = \theta_L + M_L f_{LL} + M_R f_{LR}$$

[4.9] $$0 = \theta_R + M_L f_{RL} + M_R f_{RR}$$

Since the response of a concrete beam-column is typically not linear-elastic, several iterations are often required to solve for the actual bending moment distribution. As shown in Figure 4.4, the curvature distribution in the first iteration is computed from the primary moment distribution, so the rigidity, *EI*, along the member corresponds to the primary moment distribution rather than the actual moment distribution. The rigidity distributions in the subsequent iterations are computed from the updated moment distributions, accounting for the end moments computed using Eqs. [4.8] and [4.9]. The end moments and updated moment diagram should converge to the final moment distribution, provided the interior span is discretized using a sufficient number of segments. For computing the deflected shape of concrete beam-columns, Nathan (1972) recommends using segment lengths of one to two times the section depth, so 20-30 segments should be sufficient for slenderness ratios less than 100. In certain cases, usually at very low axial loads $\left(< 0.1 f'_c A_g\right)$, the process outlined in Figure 4.4 still may not converge, regardless of the number of segments used. To achieve convergence in these cases, an algorithm was developed as part of a MATLAB program (The Mathworks Inc., 2011) that is discussed in Section 4.6. The source code for this program is given in Appendix C, where the algorithm is explained in detail.

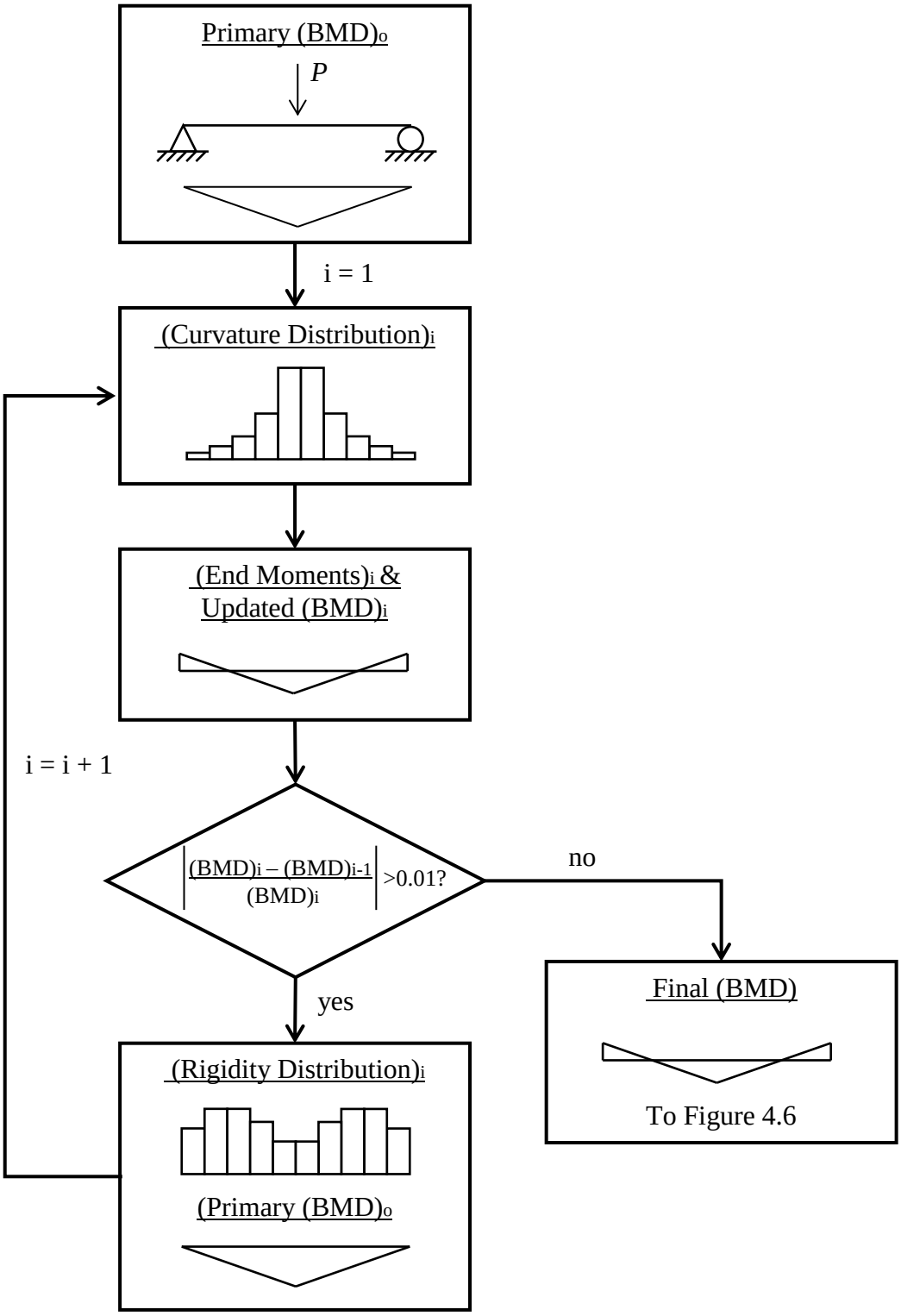

Figure 4.4: Flowchart for distributing moments in cable-stayed bridge decks.

For very slender members it is possible that the maximum negative moment can exceed the negative moment capacity before the maximum positive moment reaches the positive moment capacity. As the positive moment approaches the cross-section capacity, the secant rigidity reduces significantly. The deflection is sensitive to the secant rigidity near midspan, so as the rigidity reduces the deflections increase significantly, causing larger end rotations of the primary structure and so larger negative end moments.

If the negative moment reaches the negative moment capacity, the member will not necessarily fail. Plastic moment redistribution may occur, where the support moment remains constant at the negative moment capacity and the remaining moment necessary to satisfy equilibrium must be redistributed to the midspan. This plastic behaviour requires the negative reinforcement to yield, so the applied compression force must be less than that corresponding to a balanced failure condition. If the compression force exceeds the balanced failure load, plastic redistribution cannot occur and the member will fail when the support moment reaches the negative moment capacity.

4.4 DEFLECTED SHAPE AND SECOND-ORDER BENDING MOMENTS

Once the distribution of first-order moments and curvatures along the interior span has been determined, the deflection of the deck slab can be obtained using numerical integration. Nathan (1972) uses a numerical integration method originally proposed by Newmark that approximates the rotation, θ, and deflection, Δ, along the slab using Taylor series expansions. If the rotation is known at any point, x_o, shown in Figure 4.5, the rotation a distance Δx from x_o is, using the first two terms of the Taylor series expansion:

[4.10] $$\theta(x_o + \Delta x) = \theta(x_o) - \psi(x_o)\Delta x$$

where $\psi(x_o)$ is the curvature at x_o. Similarly, the deflection, Δ, can be approximated using the first three terms of the corresponding Taylor series expansion:

[4.11] $$\Delta(x_o + \Delta x) = \Delta(x_o) + \theta(x_o)\Delta x - \psi(x_o)\Delta x^2 / 2$$

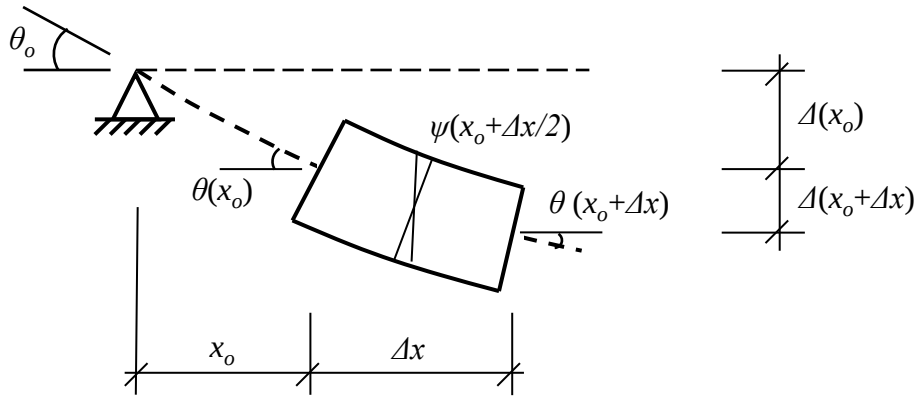

Figure 4.5: Deflected shape of a small segment of a beam-column.

The approximations provided by Eqs. [4.10] and [4.11] are equivalent to assuming constant curvature along the segment length, Δx. From this, Nathan (1985) proposes using the average curvature between x_o and $x_o+\Delta x$ instead of $\psi(x_o)$ in Eqs. [4.10] and [4.11] to provide a better approximation.

Once the deflected shape of the deck slab has been computed for the first-order moment distribution, the total moment, due to first- and second-order effects, M^*, at any point x_o is:

[4.12] $$M^*(x_o) = M(x_o) + C\Delta(x_o)$$

where $M(x_o)$ is the first-order moment at x_o. However, the second-order effects increase the rotation at each interior support and therefore increase the negative support moments. The deflection will also increase, so an iterative process must be adopted to compute the final deflected shape and total moment distribution, including second-order effects.

The flowchart shown in Figure 4.6 outlines an iterative method for computing the second-order moments that is readily implemented numerically. For a given primary first-order moment diagram, the support moments are computed and the moment diagram is shifted using the procedure shown in Figure 4.4. The associated deflected shape is then computed and the resulting *C-Δ* moments are added to the original primary moment diagram to become the starting point for the next cycle of calculations. If repeated, this process will either converge to a stable deflected shape or the total applied moment will exceed the cross-section capacity at some point along the member, indicating failure.

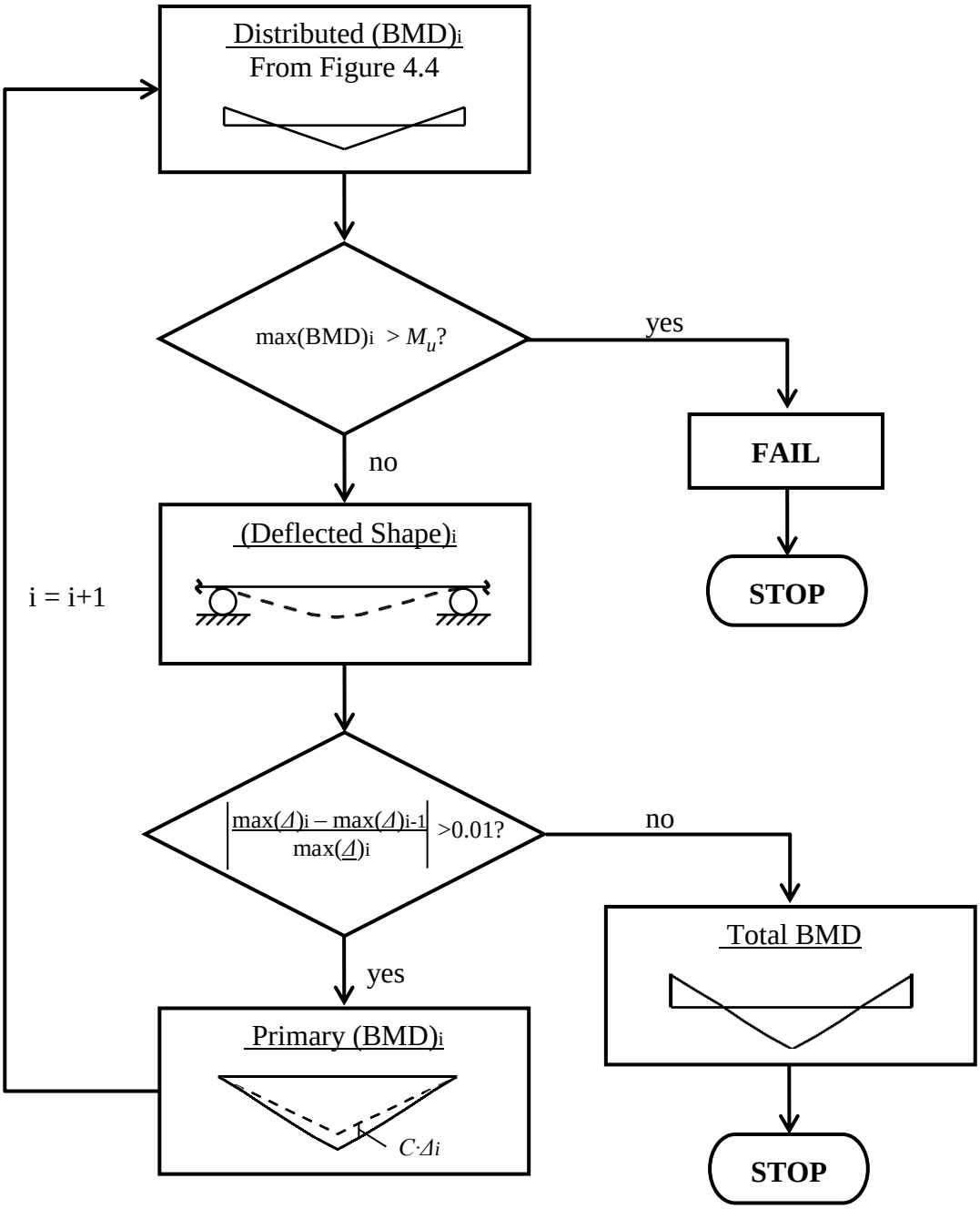

Figure 4.6: Flowchart for computing the total moment distribution of cable-stayed bridge decks.

4.5 MAXIMUM FIRST-ORDER PRIMARY MOMENT

Figure 4.7 shows the maximum possible primary moments that a member can resist if no second-order effects are present. The magnitudes of the average negative applied

moments plus the average positive applied moment must be less than or equal to the difference between the positive and negative moment capacities of the cross section. The maximum primary moment that can be resisted by slender beam-columns is the largest moment that can be applied without causing the maximum total moment, including first- and second-order effects, to exceed the cross-section capacity.

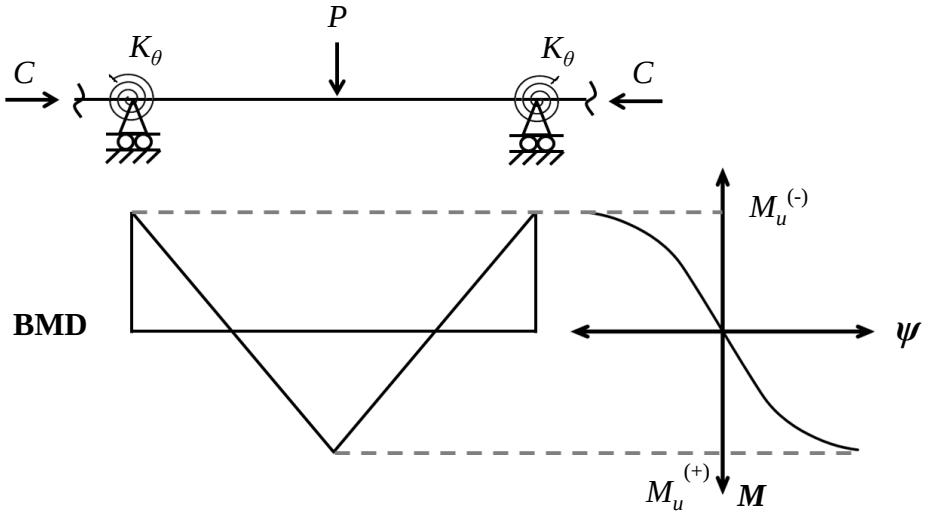

Figure 4.7: Maximum possible primary moment.

Sections that can resist a maximum positive total moment of greater than 95% of the cross-section capacity, M_u, will be assumed to have reached material failure. Instability failures will be assumed if the maximum total moment is less than 95% of the cross-section capacity.

4.6 OVERVIEW OF COMPUTER PROGRAM

A computer program was written using MATLAB R2011b (The Mathworks Inc., 2011) to analyse the idealized structure subjected to applied axial and vertical loads as shown in

Figure 4.1. The program follows the procedures presented in Sections 4.2 to 4.5 for computing the moment-curvature relationship, negative support moments, total moment diagram, and maximum primary moment diagram. The MATLAB program was developed specifically to perform a nonlinear geometric analysis, accounting for nonlinear material behaviour and cracking, of the structure shown in Figure 4.1 b). Since the program was developed specifically for this application the run time is expected to be significantly less than the run time of an equivalent finite element analysis.

As discussed in Section 4.2, methods for computing moment-curvature relationships using curvature contours have been presented previously by Nathan (1985) and Salonga (2010). Salonga (2010) also developed a program, *QULT*, to perform a second-order analysis of slender ultra-high-performance fibre-reinforced concrete columns. *QULT* is written in the MATLAB programming language and Salonga's source code for the functions that compute the moment-curvature relationship was used as a model to develop the source code for similar functions in the program discussed in this chapter.

Figure 4.8 illustrates the overall hierarchy of the program. The overall function, *CSDECK*, computes the maximum primary moment diagram that can be applied to a given cable-stayed bridge deck. Within *CSDECK*, the two main functions are *MOMCURV* to compute the moment curvature relationship and *PDELTA* to compute the total bending moment diagram, including second-order effects. Each main function contains one or more sub-functions to perform detailed calculations, as well as several basic functions to perform simple repetitive calculations.

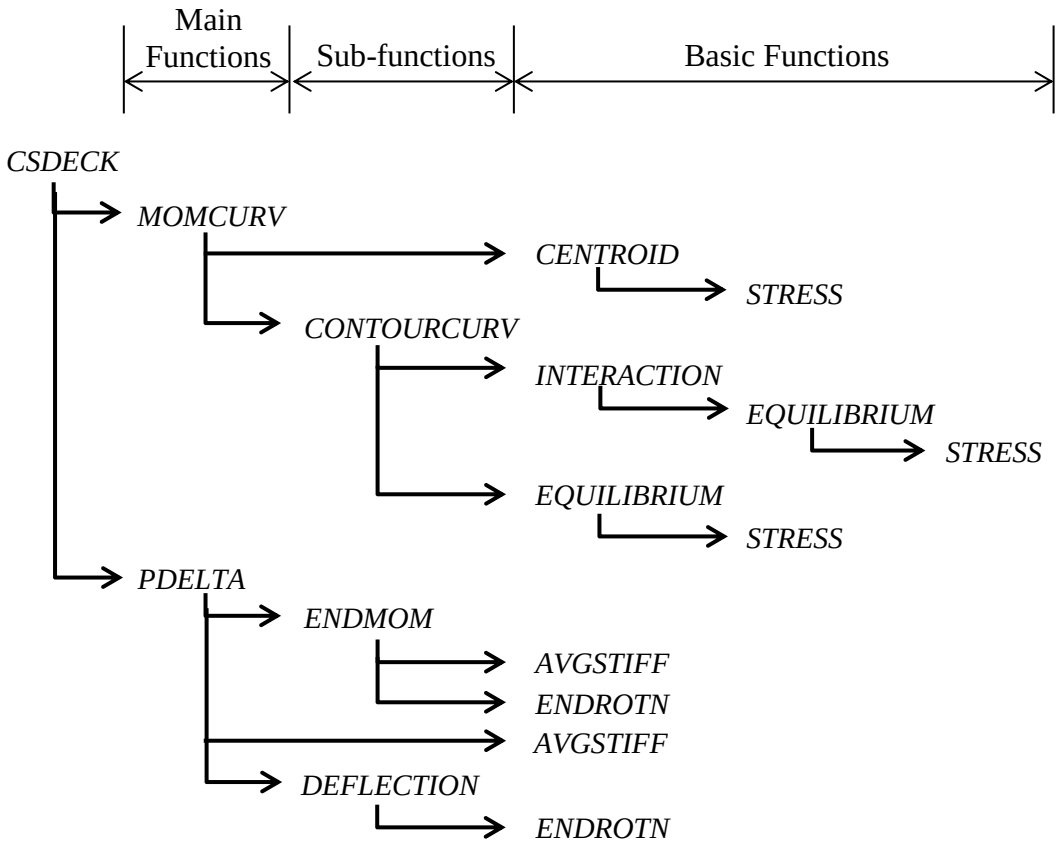

Figure 4.8: Hierarchy of the MATLAB program developed.

The function *MOMCURV* generates the moment-curvature relationship of the cross section for a given applied compression force. From Figure 4.8, *MOMCURV* does this by first calling the basic function *CENTROID* to compute the plastic centroid of the section. *MOMCURV* then calls *CONTOURCURV* to compute contours of equal curvature for the section and interpolates the moment-curvature relationship from these contours. The sub-function *CONTOURCURV* uses the function *INTERACTION* to compute the cross-section interaction diagram. The basic functions *EQUILIBRIUM* and *STRESS* are used in *INTERACTION* to compute the axial force and bending moment at each point on interaction diagram using the equations of force and moment equilibrium. This

interaction diagram is then used to determine the range of curvature contours that must be computed and the axial force and moment at each point on the contours is again found using the basic functions *EQUILIBRIUM* and *STRESS*.

Once the moment-curvature relationship has been calculated, *CSDECK* begins the second-order analysis by setting the primary first-order moment to the maximum possible value, discussed in Section 4.5, and computes the total bending moment diagram using *PDELTA*. *PDELTA* returns a matrix of zeros if any applied total moment exceeds the cross-section capacity, so *CSDECK* incrementally reduces the applied load until a stable, non-zero, total bending moment diagram is obtained from *PDELTA*.

To compute the total moment diagram, *PDELTA* calls the sub-function *ENDMOM* to determine the distribution of moments in slab, following the procedure in Section 4.3. *ENDMOM* performs an iterative loop, beginning by using the basic function *AVGSTIFF* to compute the average rigidity of each segment in the center span, corresponding to the primary moment diagram. *ENDROTN* is then called to compute the primary end rotations using the Moment Area Theorem (e.g., Hibbeler, 2009). Using the primary end rotations, *ENDMOM* computes the end moments and the revised moment diagram and then performs the loop again using *AVGSTIFF* to compute the rigidity corresponding to the revised moment diagram. This rigidity is used to provide a better approximation of the primary end rotations using *ENDROTN* and after several iterations *ENDMOM* converges to a stable bending moment diagram.

Once the distributed moment diagram is found, *PDELTA* computes rigidity of each segment using *AVGSTIFF* and calls the sub-function *DEFLECTION* to compute the deflected shape. *DEFLECTION* uses *ENDROTN* to compute the rotation of the slab at each end and then computes the rotation, θ, and deflection, Δ, at the ends of each segment using Eqs. [4.10] and [4.11]. *PDELTA* then adds the secondary moments due to the deflection at the ends of each segment to the primary moment diagram and returns to *ENDMOM* to compute the new distribution of moments. The cycle is then continued until the deflections obtained converge to a stable solution or the maximum total applied moment in the slab exceeds the cross-section capacity.

The complete source code for each function and brief explanation of the calculations performed by each function can be found in Appendix C. As discussed in Appendix C, four of the functions within *CSDECK*, *MOMCURV*, *CONTOURCURV*, *INTERACTION* (originally called *NMBOUND*), and *INTERPOLATE*, were developed by Salonga (2010) and have been implemented into *CSDECK* with only minor modifications.

4.7 VALIDATION

The program discussed in the previous chapter has been validated by comparing the results to both a nonlinear finite element analysis performed using ANSYS 12.0 (ANSYS Inc., 2009) and a computer analysis by Nathan (1987). A simplified idealization of the Talmadge Memorial Bridge deck slab, shown in Figure 4.9, was chosen as a typical example and was analysed using an iterative procedure in ANSYS 12.0 to determine the total bending moment diagram, including second-order effects. The Talmadge Memorial Bridge deck slab, shown in Figure 4.9 a), is 280mm thick and is idealized as a strip of

unit width (Bartlett, 1991) for the following analysis. The deck slab is assumed to have two layers of reinforcing steel (f_y = 400MPa), each 1400mm^2, centered at 40mm from the top and bottom faces. The floorbeam supports, shown in Figure 4.9 b), are typically spaced at 8.61m. Only the two interior supports provide rotational restraint, K_θ, assumed to be 2.2*10^4 kN·m/rad, which for a 1m wide slab is about 20% larger than the lower-bound value at the quarter-span of this bridge, as mentioned in Chapter 3. The axial compression force is 2800kN$\left(\sim 0.25 f'_c A_g\right)$ and a vertical load of 225kN is applied in the middle of the interior span.

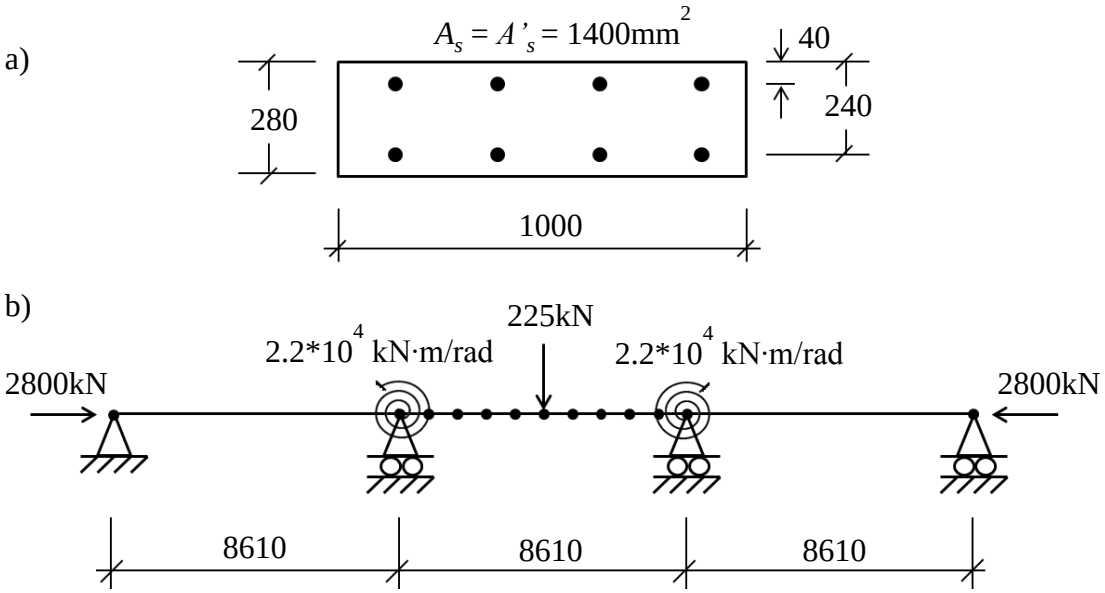

Figure 4.9: Cable-stayed bridge deck; a) cross section; b) idealized structural system (dimensions in mm).

The moment-curvature relationship was computed using the method described in Section 4.3 using the concrete stress-strain relationship used in Chapter 2 (Thorenfeldt et al., 1987), for an assumed compressive strength, f'_c, of 40MPa. The stress-strain relationship

was derived for f'_c = 40MPa and the stress values were then multiplied by 0.9. The initial tangent modulus of elasticity, E_c, was computed using Clause 8.4.1.7 of CSA S6-06 (CSA, 2006) and was divided by the 0.9 factor to counteract the effect of the stress value reduction, as explained previously in Chapter 2. The steel reinforcement was considered effective in tension but was treated as concrete in compression, since it is not tied to prevent buckling.

A nonlinear static analysis including large displacements was performed in ANSYS 12.0 to include the effect of geometric nonlinearities. Default convergence tolerances of 0.5% for force and moment imbalances were adopted. To determine the load step size the automatic time-stepping function was used, which applied the load in 7 sub-steps.

To approximate the material nonlinearities, the interior span is represented by ten segments, as shown in Figure 4.9 b), and an iterative process was used to determine an equivalent modulus of elasticity, *E*, for each segment. For the first iteration, the moment at the centroid of each segment was obtained from the primary moment diagram, which is equivalent to the moment diagram for the vertical load applied to a simply supported beam 8.61m long. The rigidity, *EI*, was computed using Eq. [1.2] for the secant rigidity, EI_{sec}, where *M* is moment at the centroid of each segment and ψ is obtained from the moment-curvature relationship. The equivalent modulus of elasticity of each segment was then computed by dividing the secant rigidity, EI_{sec}, by the moment of inertia of the gross concrete section, I_g.

The moments in the adjacent spans reduce linearly from a maximum at the interior support to zero at the exterior support, so the rigidity of these spans was assumed equal to the gross uncracked rigidity, E_cI_g, and the modulus of elasticity was not reduced. The two adjacent spans were each meshed into twenty two-dimensional beam elements (BEAM3) and each segment of the center span was meshed into two BEAM3 elements, so that the nonlinear geometric response could be accurately captured. The analysis was repeated using twice as many beam elements in each side span, and the difference in results was negligible. The rotational restraint was modelled using torsional spring elements (COMBIN14) of zero length at the two interior support nodes.

The moment diagram from the first analysis was used to determine the average moment in each segment, which was then used to find the secant rigidity, EI_{sec}, of each segment. The modulus of elasticity of the two elements within each segment was then changed to account for the new EI_{sec} and a new cycle of analysis was performed. The solution converged after eight iterations, yielding the total bending moment diagram for the interior span, including second-order effects, shown in Figure 4.10 a). For this example, instability failure did not occur. The maximum total moment determined from the ANSYS 12.0 analysis was 344kN·m at midspan, just less than the cross-section capacity of 353kN·m, indicating that a vertical load of 225kN is close to the maximum that can be resisted by this member for the applied compression load of 2800kN. Although material failure occurred, the second-order effects were still very significant. Figure 4.10 b) shows the second-order bending moments along the interior span, which have the same form as the final deformed shape. The maximum second-order moment of 123kN·m occurs due to

a midspan deflection of 44mm and must be redistributed along the span. To compute the moment magnification due to second-order effects, a first-order analysis, ignoring large displacements, was performed in ANSYS 12.0 using the same iterative procedure to compute the equivalent modulus of elasticity of the segments in the interior span. The resulting first-order moment diagram is shown by the grey line in Figure 4.10 c). The second-order effects magnify the maximum first-order negative moment of -200kN·m by a factor of 1.32, resulting in a maximum total negative moment of -263kN·m, also shown in Figure 4.10 c). Likewise, the maximum first-order positive moment of 284kN·m is magnified by 1.21, yielding a maximum total positive moment of 344kN·m.

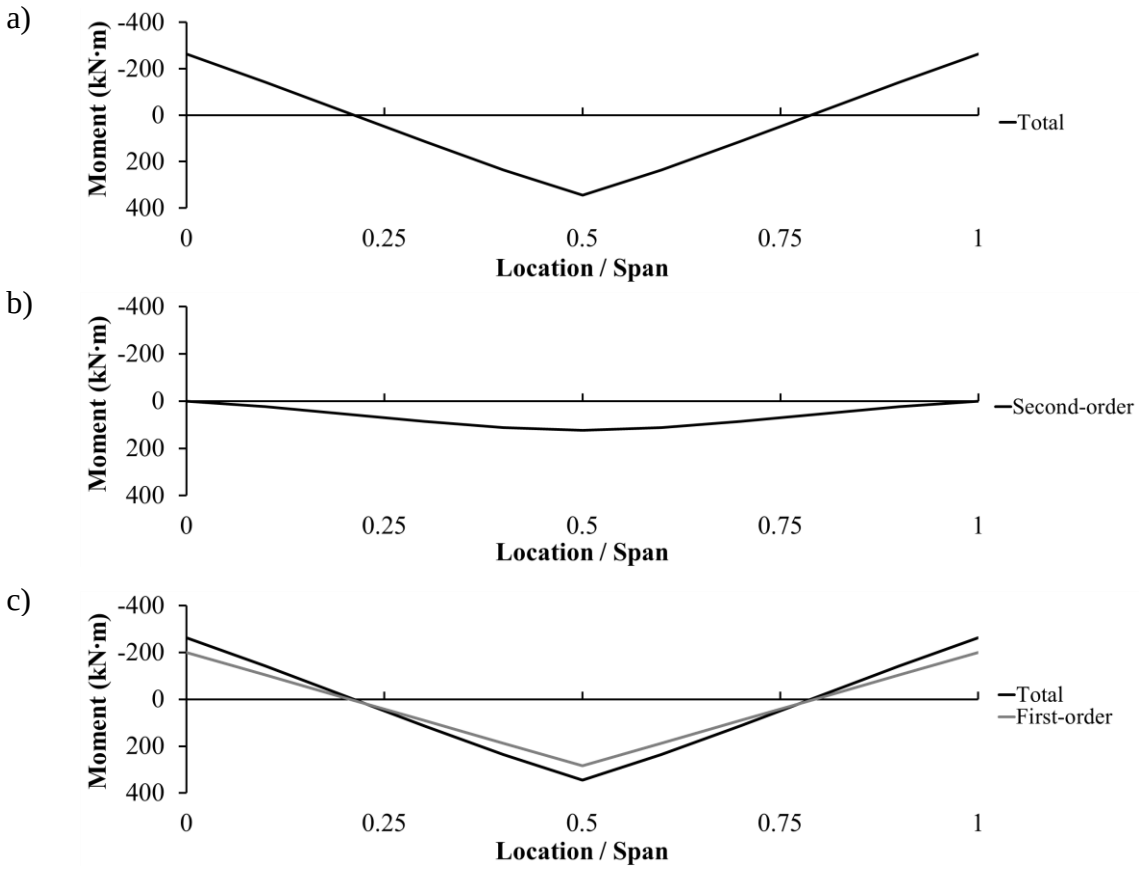

Figure 4.10: Bending moment diagrams from ANSYS 12.0; a) total; b) second-order; and c) total and first-order.

The cross section shown in Figure 4.9 was also analyzed using the *CSDECK* program. The interior span was again represented by ten segments, the modifications factors γ_L and γ_R were computed using Eqs. [4.6] and [4.7], respectively, and the resulting bending moment diagram is shown by the grey line in Figure 4.11. The black X markers represent the total moment diagram, including second-order effects, obtained from the ANSYS 12.0 analysis. Both sets of analysis results are in very good agreement, indicating that *CSDECK* provides an accurate approximation of the second-order moments in cable-stayed bridge decks subjected to non-uniform primary moments.

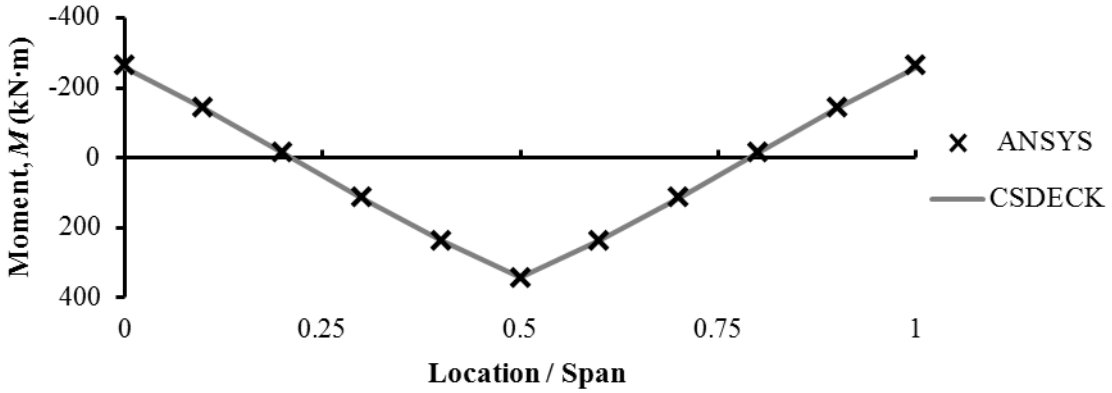

Figure 4.11: Total moment diagrams obtained from ANSYS 12.0 and the MATLAB program.

To test the accuracy of *CSDECK* further, a separate comparison using an analysis method proposed by Nathan (1987) for computing second-order effects in prestressed concrete columns was carried out. Nathan's analysis also uses the moment-curvature relationship of the cross section to approximate the curvature along the member and follows a process similar to that described in Section 4.4 for computing the deflected shape, but is limited to simply supported members. The program *CSDECK* can be used to analyze simply

supported deck slabs if the rotational restraint, K_θ, and the factors, γ_L and γ_R, are set equal to zero. This triggers the program to skip the process discussed in Section 4.3 for distributing moments, so the total moments and deflected shape are computed for the first-order moments entered for the simply supported interior span, shown in Figure 4.4.

The cross section of the Talmadge Memorial Bridge deck, shown in Figure 4.9 a), was analyzed. It was idealized to be 8.61m long, pinned at both ends, and subjected to an applied axial load of 2800kN. Using the stress-strain relationship for concrete that was used previously, the maximum equal and opposite ends moments that the member could resist were computed using the analysis program developed by Nathan (1987), assuming the steel to be effective in both tension and compression. The deck slab was discretized into segments approximately equal to the slab thickness. Nathan's program predicted that the member could resist an applied end moment of 112kN·m. The associated failure mode was instability with a maximum mid-height moment, M_c, of 245kN·m, or 65% of the predicted cross-section capacity, M_u, of 377kN·m. The analysis was repeated using the program *CSDECK*, with the member discretized into 30 segments with lengths approximately equal to the slab thickness. The maximum end moment predicted using *CSDECK* is 109kN·m, the predicted failure mode is also instability, and the maximum mid-height moment is 222kN·m, or 59% of the predicted cross-section capacity or 374kN·m. Therefore, the maximum end moments predicted using *CSDECK* are 3% less than those predicted using Nathan's program and the maximum mid-height moment predicted by *CSDECK* is 10% less. Since *CSDECK* accurately provides similar estimates of the maximum first-order end moments that the deck slab can resist and has already

been shown to agree closely with results from ANSYS 12.0 for a three-span deck system, it can be concluded that the program *CSDECK* provides acceptable approximations of the second-order moments in cable-stayed bridge decks.

4.8 SUMMARY

In this chapter a rational method was presented to compute first- and second-order moments in continuous reinforced concrete beam-columns subjected to transverse point loads between their supports. The method requires deriving the moment-curvature relationship for the given applied axial load, distributing the moments along the member to determine the negative moments at the supports, computing the final deformed shape and corresponding second-order moments, and solving iteratively for the maximum transverse loads that can be resisted.

A MATLAB program (The Mathworks Inc., 2011) was developed to apply this method to compute the maximum transverse point load that can be resisted by an idealized three-span cable-stayed bridge deck. The MATLAB program was used to compute the total moment diagram, including second-order effects, in a realistic deck slab subjected to a single vertical point load applied at the middle of the interior span. The same deck slab was analysed again using a second-order analysis in ANSYS 12.0 (ANSYS Inc., 2009) and the two programs yielded very similar results. The MATLAB program was modified to predict the capacity of a simply supported cable-stayed bridge deck subjected to equal end moments causing single curvature and the results were shown to agree with a similar second-order analysis program created by Nathan (1987) for prestressed concrete columns. Since the results from the MATLAB program are in close agreement with those

from both ANSYS 12.0 and from Nathan's program developed specifically for analyzing slender concrete beam-columns, the *CSDECK* program is deemed acceptable for approximating the second-order and total moments in cable-stayed bridge decks.

CHAPTER 5: SENSITIVITY ANALYSIS

5.1 INTRODUCTION AND RESEARCH OBJECTIVES

The current provisions in CSA S6-06 to compute moment magnification in slender concrete beam-columns have been investigated in Chapter 2. If the deck is subjected to equal and opposite end moments, they predict the capacity of an idealized simply supported cable-stayed bridge deck accurately at low applied axial loads but are extremely conservative at higher applied loads. However, this finding has limited application because cable-stayed bridge decks are typically continuous, so traffic loads create negative moments over the supporting floorbeams and positive moments at midspan. The bending moment diagram is therefore more complex than the idealized uniform moment case considered in Chapter 2. The main objectives of the research reported in this chapter are to determine variables that significantly influence the moment magnification of continuous cable-stayed bridge decks subjected to traffic loads applied between the floorbeams and to assess each significant variable in the context of the underlying mechanics.

In Chapter 4, first-order moments were computed using a nonlinear-cracked analysis, described in Section 4.3, that accounts for material nonlinearity and cracking of the cross section by discretizing the member into short segments and computing the curvature of each segment from the moment-curvature relationship. This approximates the rigidity distribution along the member, but is time-consuming and so difficult to carry out in practice. In contrast, linear-uncracked analyses assume constant rigidity along the member equal to the uncracked rigidity, $E_c I_g$, and so are readily carried out in practice.

Therefore, the secondary objectives of this chapter are to determine the moment magnifiers, δ, necessary to compute the total moments, accounting for second-order effects, from the results of a linear-uncracked first-order analysis and to determine the accuracy the current provisions of CSA S6-06 to predict these δ values.

5.2 ANALYTICAL APPROACHES

Moment magnifiers, δ, will be computed as the ratio of the total moment to the first-order moment. The total moments will be computed using the program *CSDECK*, as described in Chapter 4. The first-order moments will be determined by nonlinear-cracked analysis or by linear-uncracked analysis.

The difference between the two first-order analyses is demonstrated in Figure 5.1, for two idealized cable-stayed bridge decks with different slenderness ratios. The nonlinear-cracked first-order moment diagram, shown by the grey line in Figure 5.1 a), and total moment diagram, shown by the black line, are identical to those shown previously in Figure 4.10 c). These lines were computed for an idealized three-span segment of the Talmadge Memorial Bridge deck slab, shown in Figure 4.9, subjected to an axial compression force, C, of 2800kN ($0.25\, f'_c\, A_g$) and a vertical point load, P, of 225kN. The linear-uncracked first-order moment diagram, shown by the grey dashed line, slightly underestimates the negative moments by 14kN·m, or 7%, and overestimates the maximum positive moments by 14kN·m, or 5%. The Talmadge Memorial Bridge deck slab has a high slenderness ratio of 107, so the second-order moments are significant, magnifying the maximum negative and positive nonlinear-cracked first-order moments

by 1.32 and 1.21, respectively. These differences between the maximum moments computed using the two first-order analyses are small with respect to the magnification of the moments caused by second-order effects.

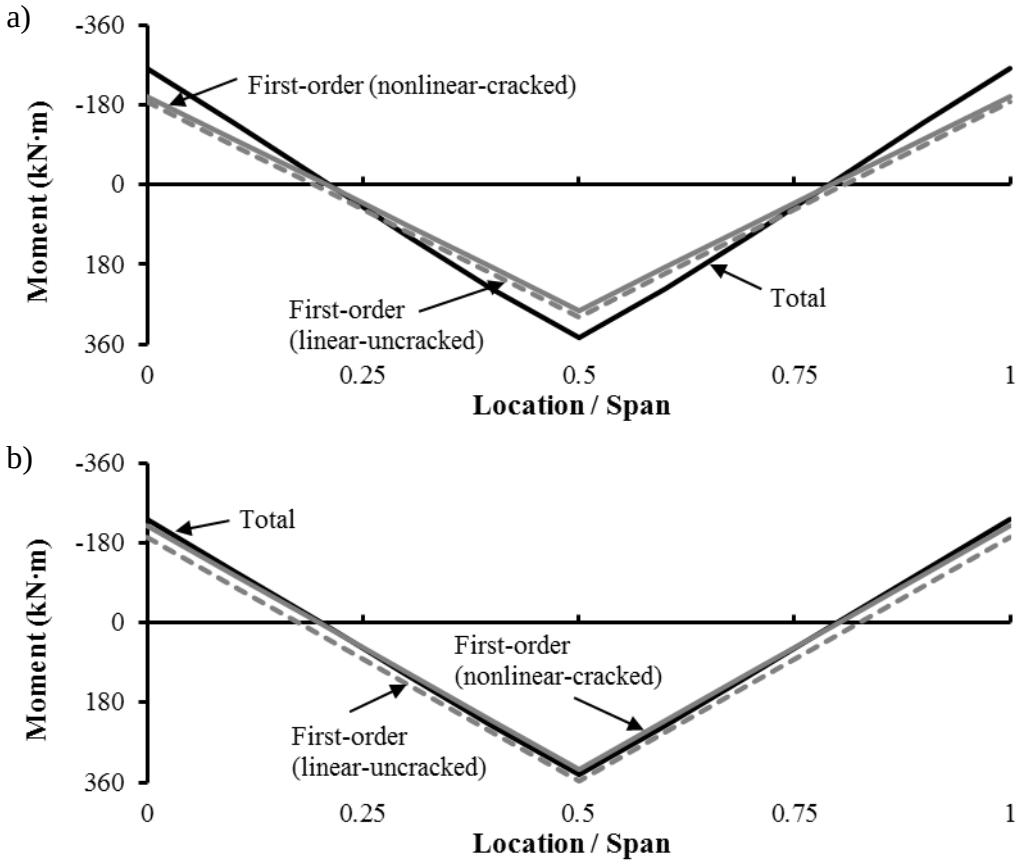

Figure 5.1: First- and second-order moment diagrams; a) *L/r* = 107; b) *L/r* = 49.

Figure 5.1 b) compares these same three moment diagrams for the same cross section with a reduced floorbeam spacing of 4m, yielding a reduced *L/r* of 49. The compression force is again 2800kN and the vertical point load is increased to 550kN, to create midspan moments, including second-order effects that approach 95% of the cross-section capacity. This relatively stocky slab has small second-order moments with positive and negative moment magnifiers of only 1.04 and 1.06, respectively. For this member, the

linear-uncracked analysis underestimates the maximum negative moments and overestimates the maximum positive moment by 26kN·m, or 8 and 12% of the maximum nonlinear-cracked positive and negative values, respectively. The positive moment magnifiers for the linear-uncracked first-order moments are therefore less than 1, implying that the second-order effects reduce the positive moments! Clearly this is not true, so linear-uncracked analyses may not be appropriate for computing the first-order moments and associated moment magnifiers of relatively stocky members.

Other parameters that affect the moment magnification, such as the magnitude of the applied axial load, may also affect the accuracy of the linear-uncracked analysis and this will be investigated as a secondary objective of the sensitivity analysis.

The floorbeams of the idealized cable-stayed bridge decks used to develop Figure 5.1 were assumed to provide $2.2*10^4$kN·m/rad of rotational restraint to the slab ends. Using the methods described in Chapter 3, this restraint can reduce the effective length factor, *k*, to 0.74 and 0.83 for the decks analyzed in Figure 5.1 a) and 5.1 b), respectively. To determine the predicted total moments using the provisions of CSA S6-06, Eq. [1.8] was used to compute the rigidity and Eq. [1.6] was used to magnify the first-order moments from the linear-uncracked analysis, neglecting the 0.75 reduction factor. The maximum total positive and negative moments shown in Figure 5.1 a) are overestimated by factors of 7.8 and 6.4, respectively and the maximum total positive and negative moments shown in Figure 5.1 b) are overestimated by 37 and 9%, respectively. Since the CSA S6-06 provisions yield unacceptably conservative results for the slender slab and conservative results for the relatively stocky slab, Eq. [2.3] (Olendzki 2008) was also investigated for

computing the rigidity, *EI*. Using this equation, the maximum total positive and negative moments shown in Figure 5.1 a) are overestimated by 67 and 37%, respectively, and the maximum total positive and negative moments shown in Figure 5.1 b) are overestimated by 14 % and underestimated by 9%, respectively. For both examples, using Eq. [2.3] to compute *EI* yielded more accurate predictions of the total moments than using Eq. [1.8]. However, the results obtained using Eq. [2.3] were still extremely conservative for the more slender slab. Therefore, both Eq. [1.8] and Eq. [2.3] are investigated to compute *EI* when determining the accuracy of the moment magnifier equation, Eq. [1.6], for estimating the second-order effects.

5.3 SCOPE OF THE SENSITIVITY ANALYSIS

A sensitivity analysis was performed to determine the parameters that have a significant influence on moment magnification in cable-stayed bridge decks. This section outlines the ranges of parameters chosen for the sensitivity analysis and defines the applied loading conditions.

5.3.1 Parameters Investigated

The moment magnifier for a column bent in symmetric single curvature due to equal and opposite end moments can be computed as:

[1.6] $$\delta = \frac{1}{1 - \left(\frac{C_f}{0.75 C_c} \right)}$$

where C_f is the factored axial load and C_c is the critical buckling load computed using Eq. [1.7]. Neglecting the 0.75 factor in Eq. [1.7] that is intended to account for uncertainties in computing C_c (Bartlett, 1991), recognizing $I = I_g = r^2 A_g$, and substituting E_c for E, this equation can be rewritten as:

[5.1] $$\delta = \frac{1}{1 - \left(\frac{C_f}{A_g}\right)\left(\frac{kL}{r}\right)^2\left(\frac{1}{\pi^2 E_c}\right)}$$

Equation [5.1] suggests that increasing either the factored axial load, C_f, or the slenderness ratio, L/r, should increase the moment magnifier significantly. Increasing the rotational restraint provided by the floorbeams, K_θ, can reduce the effective length factor, k, especially for bridges with concrete floorbeams as discussed in Chapter 3, so increasing K_θ should reduce the moment magnification. Increasing the concrete strength, f'_c, will increase the modulus of elasticity, E_c, and so can also be expected to reduce the moment magnifier. For these reasons, the following parameters will be included in the sensitivity analysis to determine their influence on the moment magnifier, δ: the applied axial load ratio, $C/f'_c A_g$; the slenderness ratio, L/r; the rotational restraint provided by the floorbeams, K_θ; and, the concrete strength, f'_c. The applied axial stress, C/A_g, in Eq. [5.1] is divided by f'_c to be made dimensionless. With this change, increasing f'_c will increase E_c and will decrease $C/f'_c A_g$ and so should be more significant in increasing δ.

Most of the methods for computing the flexural rigidity, *EI*, discussed in Chapter 2, assume that the rigidity increases with either the gross reinforcing ratio, ρ_g, or the moment of inertia of the reinforcement, I_s, as shown in Table 2.2. For this reason, both ρ_g and the steel-depth-to-slab-thickness ratio, d/h_s, will also be investigated to determine their influence on δ.

Table 5.1 outlines the ranges of each individual parameter that will be considered. The left column represents the primary parameter being examined in each set of simulated tests and the columns to the right show the ranges of the other variables investigated in each set. In all cases, the slab thickness, h_s, is assumed to be 240mm and the slab width, *w*, is assumed to be 1000mm. The applied axial load ratio was chosen to range from 0.1 to 0.7, because members with axial load less than 0.1 behave essentially as beams and the maximum compression force is limited to $0.75C_o$ for members with tie reinforcement in CSA S6-06 (CSA, 2006), where C_o is the factored axial resistance of the cross section subjected to zero moment. The use of the moment magnifier equation, Eq. [1.6], is limited in CSA S6-06 to members with slenderness ratios less than 100, so to assess the suitability of this upper-bound value, slenderness ratios up to 120 will be investigated. Slenderness ratios less than 60 will not be investigated, since higher values are common in practice (e.g. Alex Fraser Bridge, Talmadge Memorial Bridge, and James John Audubon Bridge).

Table 5.1: Ranges of variables chosen for the sensitivity analysis.

Primary Parameter	$\frac{C}{f'_c A_g}$	$\frac{L}{r}$	f'_c (MPa)	K_θ (10^3 kN·m/rad)	ρ_g (%)	$\frac{d}{h_s}$
$C/f'_c A_g$	0.1, 0.2, 0.3, 0.4, 0.5, 0.6, 0.7	60, 80, 100	40, 55	0	1.0	0.85
L/r	0.2, 0.4, 0.6	60, 70, 80, 90, 100, 110, 120	40, 55	0	1.0	0.85
f'_c (MPa)	0.2, 0.4, 0.6	60, 80	40, 50, 60, 70	0	1.0	0.85
K_θ (10^3 kN·m/rad)	0.2, 0.4, 0.6	60, 80, 100	40, 55	0, 5, 10, 50	1.0	0.85
ρ_g (%)	0.2, 0.4, 0.6	60, 80	55	0	0.5, 1.0, 1.5, 2.0	0.85
d/h_s (h_s = 240mm)	0.2, 0.4, 0.6	60, 80	55	0	1.0	0.80, 0.85, 0.90

The concrete strength, f'_c ranges from 40 to 70 MPa, since the average of these values, 55MPa, was used in both the Alex Fraser Bridge and the James John Audubon Bridge (Schemmann et al., 2011) and is believed to be representative of current practice. The concrete stress-stress relationship by Thorenfeldt et al. (1987), is adopted: stress values are derived for the given compressive strength and then multiplied by a 0.9 factor. The initial tangent modulus of elasticity, E_c, is computed using Clause 8.4.1.7 of CSA S6-06 (CSA, 2006) and is therefore divided by the 0.9 factor to counteract the effect of multiplying the stress values by 0.9, as explained previously in Chapter 2.

The rotational restraint provided by the floorbeams was chosen to be representative of the values determined in Chapter 3 for steel and concrete floorbeams. Zero rotational restraint is assumed as the lower bound for steel floorbeams and $K_\theta = 5\text{x}10^3$kN·m/rad as the approximate upper bound, based on the calculations for the steel floorbeams of the Alex Fraser Bridge. The two higher K_θ values are representative of concrete floorbeams, with K_θ of $10\text{x}10^3$kN·m/rad and $50\text{x}10^3$kN·m/rad corresponding approximately to the realistic lower and upper bounds, respectively, for the Talmadge Memorial Bridge.

The deck reinforcing ratio, ρ_g, in the Alex Fraser Bridge ranges from roughly 0.6% near the pylons to 1.3% near midspan (CBA – Buckland & Taylor Ltd., 1983). For the sensitivity analysis, the reinforcement is assumed to be distributed in two equal layers with identical covers from the top and bottom faces, with ρ_g ranging from 0.5 to 2%. Since the reinforcement is not tied to prevent buckling, it is only considered effective in tension and is assumed to act as concrete in compression. Cable-stayed bridge deck slabs are typically 200 to 300mm thick (Gimsing & Georgakis, 2012), so allowing for cover, the steel-depth-to-slab-thickness ratio, d/h_s, is chosen to range between 0.8 and 0.9.

5.3.2 Applied Loading

In Chapter 4, a second-order analysis was performed on an idealized three-span cable-stayed bridge deck with a single point load applied at the center of the interior span, as shown in Figure 4.1 b). This loading results in a maximum moment concentrated at midspan, but instability failures may be more likely to occur when the maximum positive midspan moment is distributed more uniformly along the span. To investigate this, two

loads cases will be examined; one case with a single vertical point load applied to the middle of the interior span, as shown in Figure 4.1 b), and another case with two point loads applied to the interior span, to achieve a region of uniform first-order positive moment.

Figure 5.2 a) shows a cable-stayed bridge deck with a uniformly distributed load applied along the entire length, and Figure 5.2 b) shows the same bridge deck with two point loads applied to each span. Assuming the deck is infinitely long, a linear uncracked first-order analysis yields maximum negative moments at the supports equivalent to $\omega L^2/12$ for the uniformly distributed load, twice the maximum positive moment at midspan of $\omega L^2/24$, and points of zero moment at $0.21L$ from the supports, as shown in Figure 5.2 c). To achieve equivalent moments, the two point loads, P, must have magnitudes of $3\omega L/8$, and must be placed at the third points, as shown in Figures 5.2 b) and c). In this case, the points of zero moment are $0.22L$ from the supports.

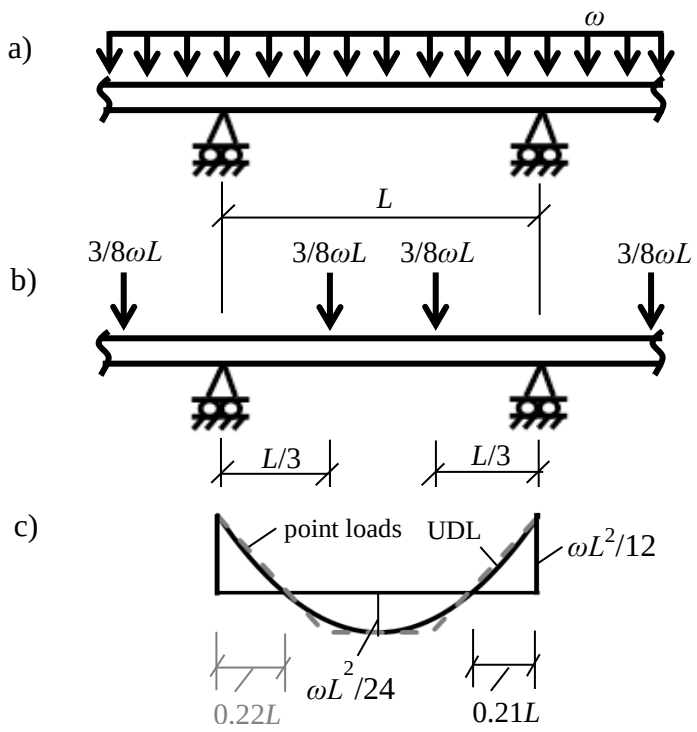

Figure 5.2: Cable-stayed bridge deck loading: a) uniformly distributed; b) two point loads spaced at *L*/3; c) super-imposed moment diagrams.

Figure 5.3 shows the simplified three-span continuous deck investigated for the two-point-load case. The compression force, *C*, is constant in each span and two vertical point loads, *P*, are applied to the interior span at the third points only. Both interior supports are assumed to provide some rotational restraint, K_θ, and the end supports are assumed pinned. The same structural idealization will be used for cases with one vertical point load applied to the interior span, shown previously in Figure 4.1 b).

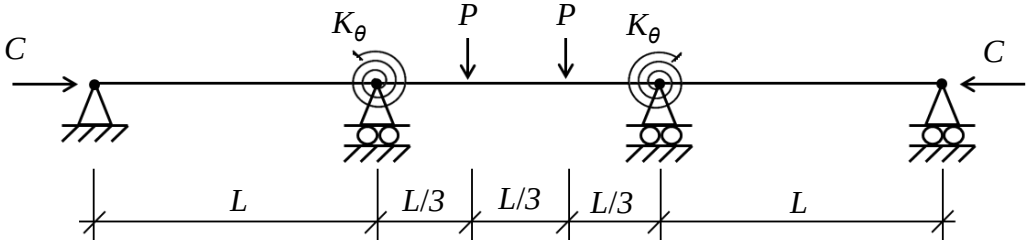

Figure 5.3: Idealized cable-stayed bridge deck used to perform a sensitivity analysis.

5.4 *CSDECK* RESULTS FOR VARIOUS APPLIED AXIAL LOAD RATIOS

Figures 5.4 a) and b) show the variation of the moment magnifier with the applied axial load ratio, $C/f'_c A_g$, for a 240mm thick deck slab with f'_c=55MPa, ρ_g=1%, and K_θ=0, as defined in the first row of Table 5.1. In Figure 5.4 a) the first-order moments were computed using the nonlinear-cracked analysis, accounting for cracking and material nonlinearity, while the first-order moments in Figure 5.4 b) were computed using the linear-uncracked analysis. Cases with slenderness ratios of 60, 80, and 100 were investigated as indicated by the different coloured lines. The solid lines are the moment magnifiers for the maximum positive moment at midspan and the dashed lines are the moment magnifiers for the maximum negative moments at the floorbeam supports.

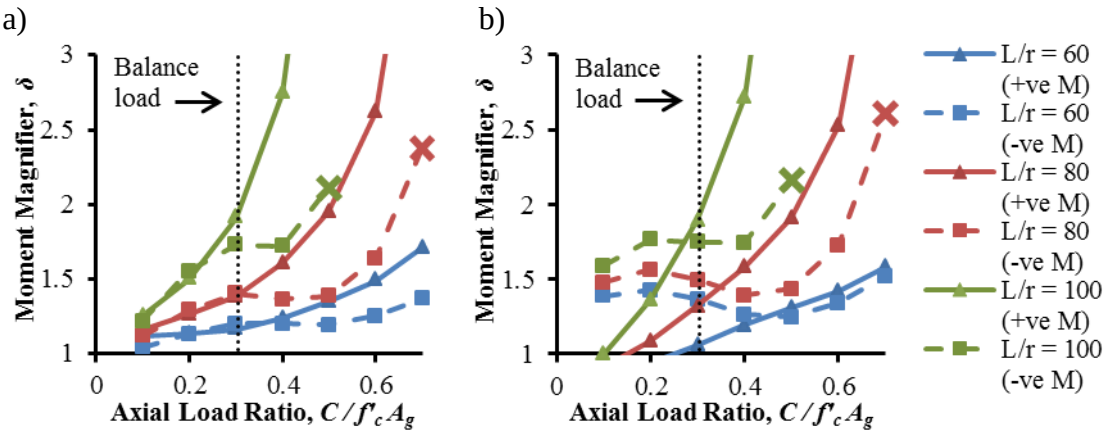

Figure 5.4: Moment magnifier for various applied axial load ratios when f'_c = 55MPa, using: a) nonlinear-cracked first-order analysis; b) linear-uncracked first-order analysis.

The X markers on the red and green dashed lines in Figure 5.4 represent instability failures, where the maximum total moments are less than 95% of the cross-section capacities. The corresponding positive moment magnifiers in both cases were greater than 4, exceeding the limit of the vertical axis. Given the accuracy of current methods for

computing slenderness effects, a design practitioner is likely to be leery of moment magnifiers exceeding 2, so for the rest of this investigation, moment magnifiers greater than 2 will be considered unrealistic. Members with L/r=100 will buckle due to the applied axial load alone when C>0.5 $f'_c A_g$, so the green lines terminate at these load ratios.

Figure 5.4 a) demonstrates that the moment magnifier increases as the applied axial load ratio increases, as is predicted by Eq. [5.1], and the increase in positive moment magnifiers is monotonic at all slenderness ratios. Below the balanced failure load, shown by the black-dotted line at roughly 0.3 $f'_c A_g$, the negative and positive moment magnifiers are similar in magnitude and increase by roughly the same amount. At loads just exceeding the balanced failure load, they diverge: the positive moment magnifiers continue to increase rapidly with $C/f'_c A_g$, but the negative moment magnifiers reduce slightly.

This can be explained using Figure 5.5, which shows the moment-curvature relationships for this cross section at two applied axial loads. The grey line is for an applied axial load of 0.2 $f'_c A_g$, which is below the balanced load of 0.3 $f'_c A_g$, and the black line is for an applied axial load of 0.4 $f'_c A_g$. All results shown in Figure 5.4 at applied axial loads of either 0.2 $f'_c A_g$ or 0.4 $f'_c A_g$ reached material failure at midspan, so the secant rigidity at midspan is shown by the black-dotted lines in Figure 5.5. The loss of rigidity for each axial load level can be seen by comparing the secant rigidities at midspan to the uncracked rigidity, $E_c I_g$, shown by the black-dashed line. Since the concrete is assumed to

have zero tensile strength, the cross sections at both applied axial loads will crack at the decompression moments, M_d. The section subjected to an applied axial load of $0.2 f'_c A_g$ will also experience yielding when the maximum moment reaches the yield moment, M_y. The combined effects of concrete cracking and steel yielding when $C = 0.2 f'_c A_g$ reduce the midspan rigidity to only 34% of $E_c I_g$, as shown, causing large rotations at the ends of the interior member and so large negative moments at the interior supports. The section subjected to the higher applied axial load of $0.4 f'_c A_g$ has a much higher decompression moment and the steel never yields, resulting in a midspan rigidity of 63% of $E_c I_g$. This is approximately 85% larger than that of the sections subjected to an applied axial load of $0.2 f'_c A_g$. To develop large negative moments there must be a significant reduction in rigidity near midspan of the slab. Since the rigidity at failure is much higher when the load is above the balanced failure load than when it is below, more moment is distributed to the midspan and so the maximum negative moments are less.

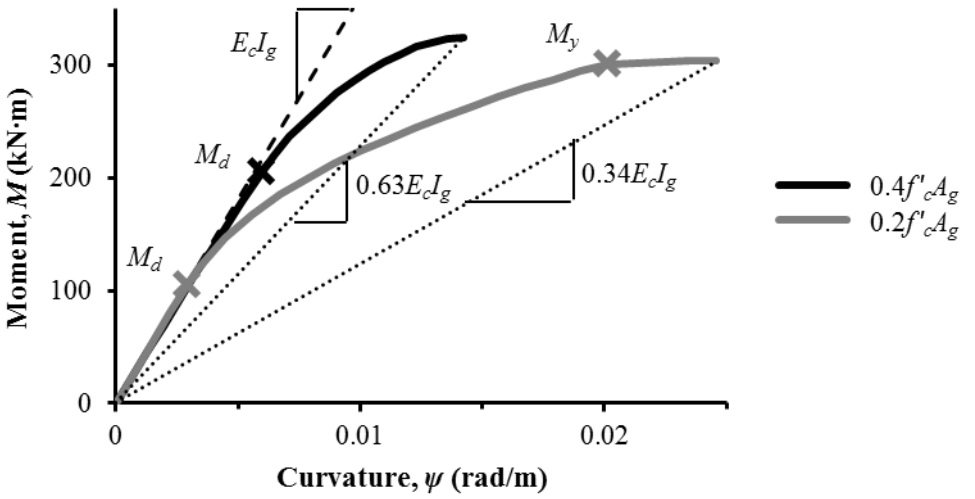

Figure 5.5: Moment-curvature relationships for two applied axial loads.

The negative moment magnifiers are also influenced by the magnitude of the applied moment necessary to cause cracking. The decompression moments, M_d, for applied axial loads of $0.2 f'_c A_g$ and $0.4 f'_c A_g$ equal 105kN.m and 205kN.m, respectively, which correspond to 35% and 63% of the respective cross-section capacities. As the applied vertical point loads are increased, the maximum negative moment magnifier remains essentially constant until the maximum moment at midspan reaches M_d, whereupon, the midspan rigidity reduces and the maximum negative moment magnifiers increase. Since almost twice as much vertical load must be applied to reach M_d when the applied axial load is $0.4 f'_c A_g$ than when it is $0.2 f'_c A_g$, much less additional load must be applied to increase the midspan moments from M_d to the cross-section capacity, M_u, so the increase in negative moment magnifiers is significantly less.

Comparing Figure 5.4 a) to Figure 5.4 b), it can be seen that the moment magnifiers computed using the linear-uncracked first-order analysis tend to follow similar trends as those computed using the nonlinear-cracked first-order analysis, especially at higher applied axial loads. Figure 5.6 shows the ratio of the moment magnifiers computed using a linear-uncracked analysis, δ_L, to those computed using the nonlinear-cracked analysis, δ_{NL}. The linear-uncracked analysis always underestimates the positive moment magnifiers, shown by the solid lines, and overestimates the negative moment magnifiers, shown by the dashed lines, since it overestimates the rigidity along the length of the interior span and so underestimates the negative first-order moments at the supports and overestimates the positive first-order moments at midspan. The two horizontal dashed lines indicate the 10% difference limits that define the range for acceptable predictions.

Values less than the lower limit can result in positive moment magnifiers less than 1, as shown in Figure 5.4 b).

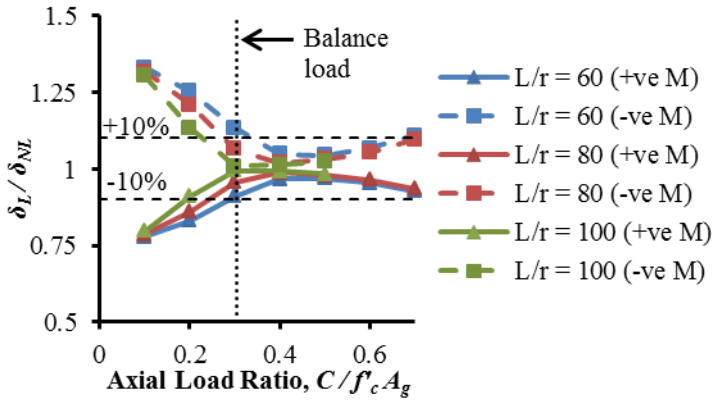

Figure 5.6: Ratio of moment magnifiers computed using a linear-uncracked first-order analysis to those using a nonlinear-cracked first-order analysis.

Figure 5.7 b) shows the rigidity distribution due to first-order moments according to the nonlinear-cracked analysis, for a member with a slenderness ratio of 80 and an applied axial load of $0.2 f'_c A_g$, loaded as shown in Figure 5.7 a). The actual rigidity along most of the slab is markedly less than the uncracked rigidity, $E_c I_g$, which affects the curvature distribution along the slab. Figures 5.7 c) and d) show the first-order curvature distributions computed using the linear-uncracked and the nonlinear-cracked analyses, respectively. From the Moment-Area Theorem, the rotation at each interior support is equal to the area under the curvature diagram between the interior support and midspan, shown shaded in both diagrams. Since the nonlinear-cracked analysis produces rigidities that are less than the uncracked value, $E_c I_g$, as demonstrated in Figure 5.7 b), the associated curvatures, shown in Figure 5.7 d), are larger than those obtained from the linear-uncracked analysis, shown in Figure 5.7 c), and so the computed rotations are also

larger. For this example, the linear-uncracked analysis predicts the end rotations to be $9.50*10^{-3}$ rad, 17% less than the nonlinear-cracked value of $11.5*10^{-3}$ rad, which is more accurate. Thus the linear-uncracked analysis underestimates the negative moments and overestimates the positive moments, leading to an overestimation of the negative moment magnifiers and underestimation of the positive moment magnifiers.

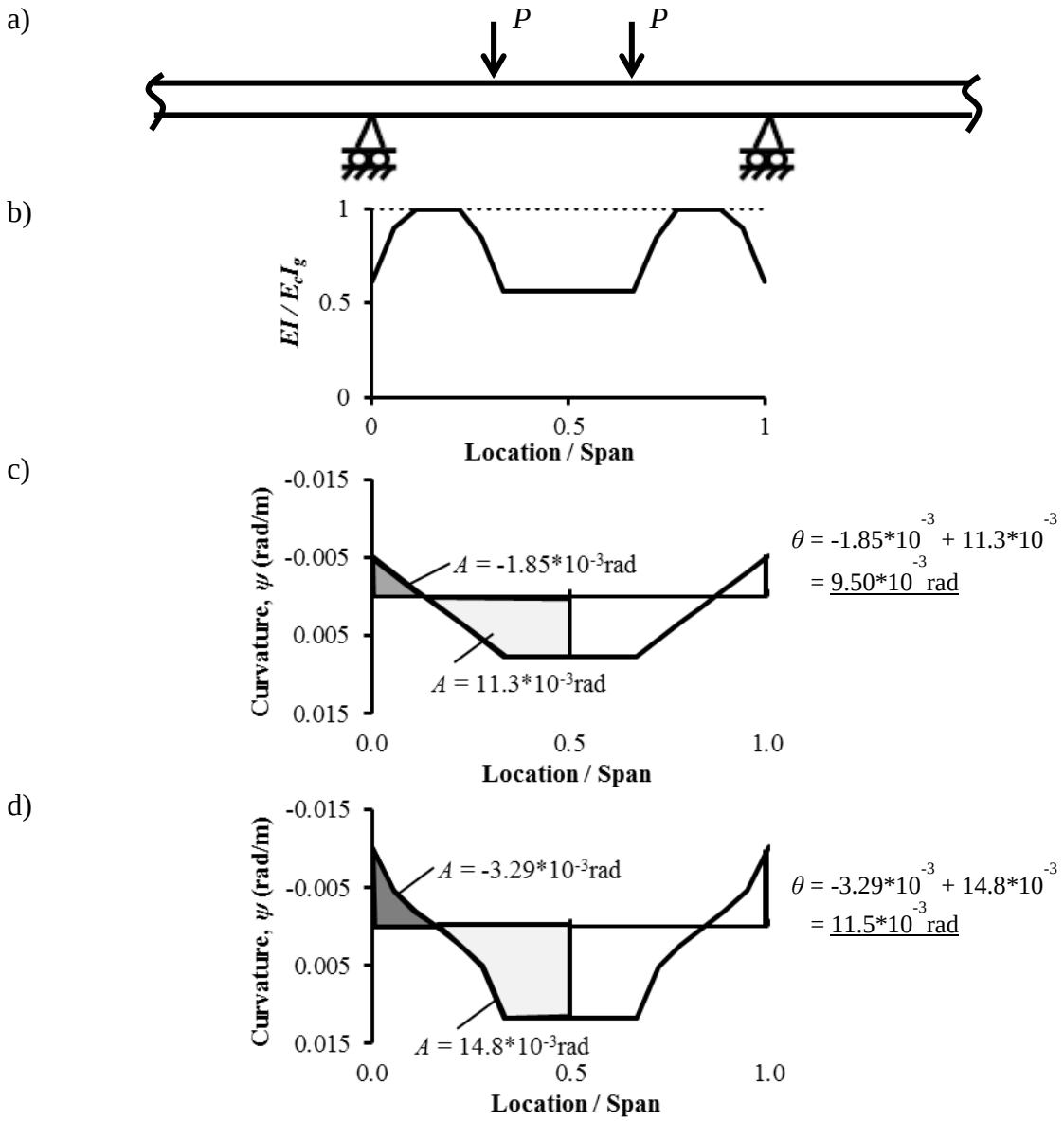

Figure 5.7: a) Beam elevation; b) first-order rigidity distribution; c) linear-uncracked first-order curvature diagram; d) nonlinear-cracked first-order curvature diagram.

Figure 5.7 was derived for an applied axial load of $0.2f'_c A_g$, which is less than the balanced axial load of $0.3f'_c A_g$. As demonstrated in Figure 5.6, the difference between the two first-order analyses is largest when the applied axial load is less than the balanced failure load, i.e., where the effects of cracking and yielding are most significant. As the applied axial load exceeds the balanced failure load, the difference between the two analyses reduces and the linear-uncracked analysis provides a good approximation of the nonlinear-cracked first-order moments. For the case shown in Figure 5.7 b), the rigidities associated with the first-order moments varies from 56 to 100% of E_cI_g. Figure 5.8 shows the moment-curvature relationship for the same section with an applied axial load of $0.4f'_c A_g$. The largest first-order moment obtained from the nonlinear-cracked analyses is 261kN·m for the member with a slenderness ratio of 60. Within this range of applied first-order moments, also shown in Figure 5.8, the secant rigidity ranges from the uncracked value, E_cI_g, to a minimum value, corresponding to the black-dashed line, of 87% of E_cI_g. Since in this case the rigidities associated with first-order moment are much closer to E_cI_g, the linear-uncracked analysis provides a much better approximation of the nonlinear-cracked first-order moments than when the load is below the balanced failure load. When C ranges from $0.4f'_c A_g$ to $0.5f'_c A_g$, the difference between the results from the two analyses at all slenderness ratios is less than 10%.

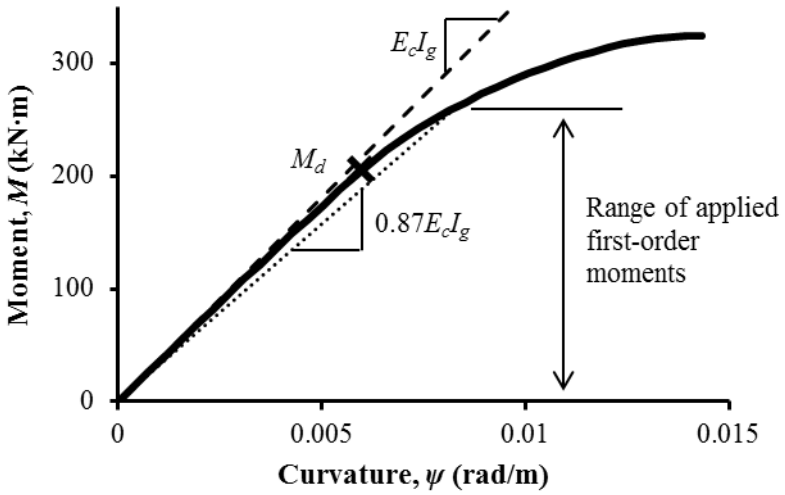

Figure 5.8: Moment curvature relationship for $C = 0.4 f'_c A_g$.

For applied axial loads much greater than the balanced failure load, say $C > 0.5 f'_c A_g$, the differences between the two analyses begin to increase again, as shown in Figure 5.6. The moment-curvature relationship for the cross section at an applied axial load of $0.6 f'_c A_g$ is shown in Figure 5.9. For this applied axial load, the member cannot reach the decompression moment and so will remain uncracked along its entire length until failure. However, the secant rigidity for any applied moment is always less than E_cI_g, as shown. The concrete stress due to the applied axial load alone is $0.6 f'_c$ and applied moments will increase this stress in some regions to $0.9 f'_c$, the maximum value permitted for the stress-strain relationship. These large stresses cause the secant modulus of elasticity of the concrete to be significantly less than that assumed in the linear-uncracked analysis.

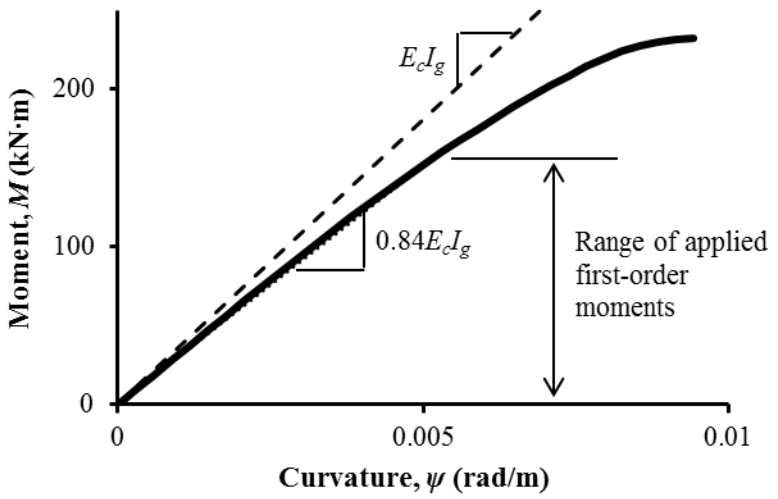

Figure 5.9: Moment curvature relationship for $C = 0.6 f'_c A_g$.

The maximum first-order moment computed using the nonlinear-cracked analysis for a member with an applied axial load of $0.6 f'_c A_g$ and a slenderness ratio of 60 was 155kN·m. Within this range of applied first-order moments, shown on Figure 5.9, the secant rigidity varies only slightly from 91% of E_cI_g, in regions with zero moment, to 84% of E_cI_g at the maximum moment region at midspan. Since the rigidity is always less than E_cI_g at these high loads, the difference between the two analyses is larger than when the applied axial load is first increased beyond $0.4 f'_c A_g$.

Lastly, Figure 5.6 indicates that the error between the two analyses decreases as the slenderness ratio increases and this trend will be examined further in the following section.

The results shown in Figures 5.4 and 5.6 were computed for a concrete strength, f'_c, of 55MPa. These analyses were also performed for f'_c = 40MPa, as indicated in Table 5.1.

All of the same trends were observed, except the difference between the results obtained from the two analyses was slightly larger. For f'_c = 40MPa, the difference between the results is less than 10% at all slenderness ratios only when the applied axial load ranges from $0.4 f'_c A_g$ to $0.5 f'_c A_g$, instead of $0.4 f'_c A_g$ to $0.6 f'_c A_g$ as shown in Figure 5.6.

All of the tests outlined in the first row of Table 5.1 were also performed for the load case with a single vertical point load. Figures D.1 and D.2 in Appendix D for the single-point-load case are comparable to Figures 5.4 and 5.5, respectively, for the two-point-load case. The trends described herein for the two-point-load case also apply to the single-point-load case, except the moment magnifiers for the single-point-load case are always less than those for the two-point-load case, since the single point load does not create a large region of uniform moment near midspan, as discussed in Section 5.3.2, so the second-order effects are not as significant and the moment magnifiers are less.

Furthermore, as described in Section D.1, the accuracy of the linear-uncracked analysis is also better for the single-point-load case. The difference between the two analyses is less than 10% at all slenderness ratios, when the applied axial load is between $0.4 f'_c A_g$ and $0.6 f'_c A_g$ for concrete strengths, f'_c, of either 40 or 55MPa.

5.5 *CSDECK* RESULTS FOR VARIOUS SLENDERNESS RATIOS

Figures 5.10 a) and b) show the variation of the moment magnifier with the slenderness ratio, *L/r*, for the same cross section used in the previous section with f'_c=55MPa, ρ_g=1%, and K_θ=0, as defined in the second row of Table 5.1. The first-order moments in

Figure 5.10 a), were computed using the nonlinear-cracked analysis and the first-order moments in Figure 5.10 b) were computed using the linear-uncracked analysis. The coloured lines represent the three different applied axial load ratios that were investigated, 0.2, 0.4, and 0.6. Again, the solid lines are the moment magnifiers for the maximum positive moment at midspan and the dashed lines are the moment magnifiers for the maximum negative moments at the supports.

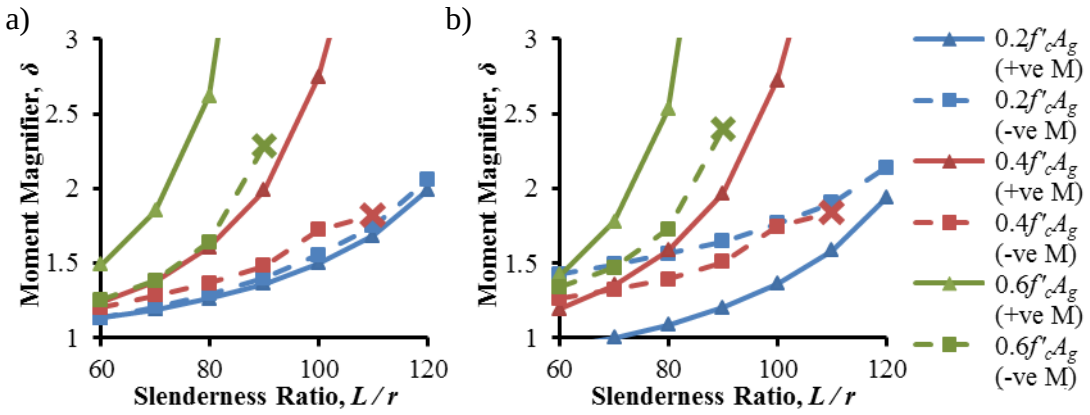

Figure 5.10: Moment magnifier for various slenderness ratios when f'_c = 55MPa, using: a) nonlinear-cracked first-order moment diagram; b) linear-uncracked first-order moment diagram.

The X markers in Figure 5.10, representing instability failures, only appear on the dashed lines for negative moments, as was the case in Figure 5.4, because the positive moment magnifiers in these cases again exceeded 4. Moment magnifiers of this magnitude are not realistic in practice. The green lines, corresponding to applied axial loads of $0.6 f'_c A_g$, are not shown for $L/r > 90$ and the red lines, $0.4 f'_c A_g$, stop before $L/r = 120$, because at these slenderness ratios the members will buckle when subjected to the applied axial load alone.

Figure 5.10 a) demonstrates that the moment magnifier, δ, always increases as the slenderness ratio increases. This is consistent with Eq. [5.1]. The previous observation that moment magnifiers for positive and negative moments are roughly equal when the applied axial load is less than that corresponding to the balance point, seems to hold for the range of slenderness ratios examined, at least for an applied axial load of $0.2 f'_c A_g$. However, this trend is completely hidden if a linear-uncracked first-order analysis is adopted, as shown in Figure 5.10 b), because the difference between the two analyses has previously been shown to be greatest at this axial load level.

It is again apparent in Figure 5.10 a) that once the applied axial load exceeds the balanced failure load, i.e., $0.3 f'_c A_g$, the positive moment magnifiers always exceed the negative moment magnifiers. For a member with constant slenderness, this is due to both the midspan stiffness at failure and the magnitude of the decompression moment, M_d, as was explained in the previous section. As the slenderness ratio increases, however, the difference between the positive and negative moments increases, since the maximum negative moments also reduce as the slenderness ratio increases. Figure 5.11 a) shows the maximum negative moments, including second-order effects, as a ratio of the cross-section capacity, M_u, for each case investigated in Figure 5.10. For the applied axial load of $0.2 f'_c A_g$, the negative moment remains constant as the slenderness increases from 60 to 70, since plastic redistribution occurs at these lengths and the negative moments equal the cross-section capacity, M_u. Otherwise, the negative moments always reduce as the slenderness ratio increases due to the increased second-order effects. Since any rotational restraint provided by the floorbeams, K_θ, is ignored in these analyses, the ends of the

interior span are restrained only by the flexural stiffness of the adjacent spans. Figure 5.11 b) shows the γ_L and γ_R factors, computed using Eqs. [4.5], [4.6], and [4.7], used to reduce the flexural stiffnesses of the left and right adjacent spans, accounting for second-order effects as discussed in Section 4.3. Clearly, increasing *L/r* reduces γ_L and γ_R and comparing Figures 5.11 a) and Figure 5.11 b), the reduction in γ_L and γ_R leads to a similar reduction in negative moments.

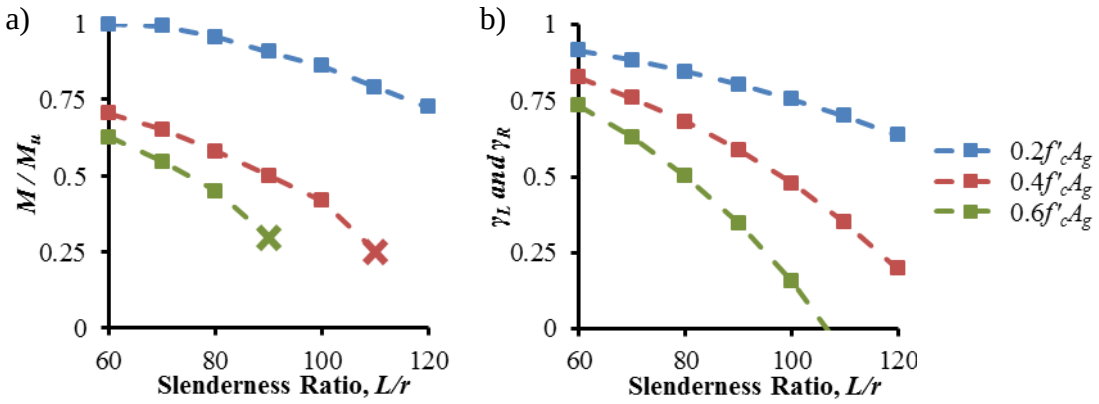

Figure 5.11: Reduction due to increasing slenderness: a) ratio of total negative moments to the cross-section capacity; b) modification factors, γ_L and γ_R.

Figure 5.12 shows the ratio of the moment magnifier computed using linear-uncracked analysis, δ_L, to that computed using the nonlinear-cracked analysis, δ_{NL}. The uncracked analysis provides a better approximation of the actual first-order moments as the slenderness ratio increases, as was noted in the previous section. Increasing the slenderness ratio increases the moment magnifier, as demonstrated by Figure 5.10, so the corresponding first-order moments must be reduced. If the range of first-order moments shown in Figure 5.8 is reduced, the rigidity along the length of the member will approach $E_c I_g$ for the members with applied axial loads less than or equal to $0.5 f'_c A_g$. For

members with very high applied axial loads of $0.6f'_cA_g$, the range of first-order moments still reduces as the slenderness ratio increases, but the member remains uncracked until failure, as shown in Figure 5.9, so the rigidity remains almost constant over the entire range of moments. Since increasing the slenderness ratio has very little effect on the rigidity at this applied axial load, it also has very little effect on the accuracy of the linear-uncracked analysis.

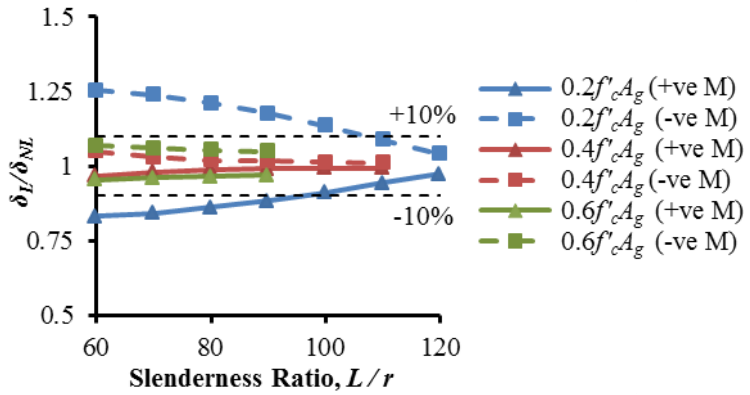

Figure 5.12: Ratio of moment magnifiers computed using a linear-uncracked first-order analysis and a nonlinear-cracked first-order analysis for various slenderness ratios.

If a 10% difference is again deemed to be the limit of acceptability, the linear-uncracked analysis provides acceptable predictions of the nonlinear-cracked first-order moments at all slenderness ratios when the applied axial load is between $0.4f'_cA_g$ and $0.6f'_cA_g$, as shown in Figure 5.12. At an applied axial load of $0.2f'_cA_g$, the linear-uncracked analysis only provides acceptable predictions of the first-order moments if the slenderness ratio exceeds 110.

These analyses were repeated for f'_c = 40MPa. All of the same trends were observed, except the difference between the results from the two first-order analyses was slightly larger. For f'_c = 40MPa, it was noted previously that the difference between the moment magnifiers is less than 10% at all slenderness ratios only when the applied axial load ranges from $0.4 f'_c A_g$ to $0.5 f'_c A_g$. However, the linear-uncracked analysis is still acceptable at most slenderness ratios when $C = 0.6 f'_c A_g$ and the difference in moment magnifiers exceeded 10% only when *L/r*=60. Three instability failures were observed when f'_c = 40MPa and in one case, the positive moment magnifier was 2.8. This is the lowest moment magnifier that was observed with an instability failure during this investigation, but is still much greater than 2, the upper limit for realistic cases.

All of the analyses shown in the second row of Table 5.1 were also performed for the single-vertical-point-load case. Figures D.3 and D.4 in Appendix D for the single-point-load case are comparable to Figures 5.10 and 5.12, respectively, for the two-point-load case. Again, the trends described herein for the two-point-load case also apply to the single-point-load case except, as mentioned previously, the magnitude of the moment magnifiers for a given applied axial load and slenderness ratio are again less for the single-point-load case than those for the two-point load case. The accuracy of the linear-uncracked analysis is also better for the single-point-load case. The difference between the two first-order analyses is less than 10% at all slenderness ratios, when the applied axial load is between $0.4 f'_c A_g$ and $0.6 f'_c A_g$ for concrete strengths, f'_c, of 40 or 55MPa.

5.6 *CSDECK* RESULTS FOR VARIOUS CONCRETE COMPRESSIVE STRENGTHS

Figures 5.13 a) and b) show the variation of the moment magnifier with the concrete compressive strength, f'_c, for the cross section used previously with ρ_g=1% and *L/r* = 80, as defined in Table 5.1. In Figure 5.13 a) the first-order moments were computed using the nonlinear-cracked analysis and the first-order moments in Figure 5.13 b) were computed using the linear-uncracked analysis. Three constant loads of 2400kN, 4800kN, and 7200kN, were chosen since they represent $0.2 f'_c A_g$, $0.4 f'_c A_g$, and $0.6 f'_c A_g$, respectively, for the members with f'_c=50MPa. All of the results shown in Figure 5.13 are material failures. The solid lines again represent positive moment magnifiers computed at midspan and the dashed lines are the negative moment magnifiers computed at the supports.

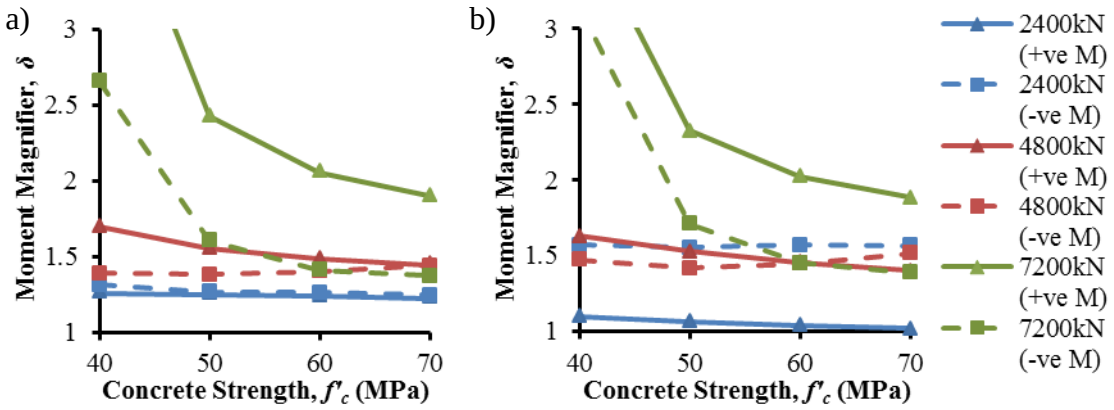

Figure 5.13: Moment magnifier for various concrete compressive strengths when *L/r* = 80, using: a) nonlinear-cracked first-order moment diagram; b) linear-uncracked first-order moment diagram.

Figure 5.13 a) demonstrates that increasing the concrete strength usually reduces the moment magnifier, as is evident from Eq. [5.1], since increasing f'_c also increases the

modulus of elasticity, E_c. Furthermore, increasing f'_c while holding C constant reduces the applied axial load ratio, $C/f'_c A_g$, which generally reduces the moment magnifier, as described in Section 5.4. An exception occurs in the negative moment magnifiers at a load of 4800kN, shown by the dashed-red line, where the moment magnifier increases slightly. As the concrete compressive strength is increased, the axial load at balanced failure also increases. For $f'_c \leq$ 60MPa, 4800kN is above the balanced failure load, while for greater strengths it is below it. In Section 5.4 it was observed that as the applied axial load just exceeds the balanced failure load, the negative moment magnifiers reduce slightly, since both the midspan rigidity and the decompression moment increase. At 4800kN, the applied axial load ratio, $C/f'_c A_g$, is decreased from 0.50, well above that at balanced failure, to 0.29, just below that at balanced failure, as the concrete strength increases from 40 to 70MPa. This reduces both the rigidity at midspan and the decompression moment, so more moment is distributed to the supports and the negative moment magnifiers increase slightly. The other values of applied axial loads remain either consistently above or below that at balanced failure for the range of concrete strengths investigated, so this increase does not occur.

The analyses were repeated for a slenderness ratio of 60, as shown in Table 5.1, and the same trends were noticed, except the magnitudes of the moment magnifiers were less. The same ranges of parameters, shown in the third row of Table 5.1, were also investigated for the single-point-load case and the results for L/r = 80 are shown in Figure D.5 in Appendix D. All of the trends noted in this section can be observed in Figure D.5

and, once again, the magnitudes of the moment magnifiers are less for the single-point-load case.

5.7 *CSDECK* RESULTS FOR VARIOUS FLOORBEAM ROTATIONAL RESTRAINTS

Figures 5.14 a), b), and c) show the moment magnifier, computed using the nonlinear-cracked analysis, plotted against the rotational restraint provided by the floorbeams, K_θ, for the same cross section used previously with f'_c = 55MPa, ρ_g=1%, and slenderness ratios of 60, 80, and 100, respectively. Applied axial load ratios of 0.2, 0.4, and 0.6 were investigated and the solid lines and dashed lines again represent the positive and negative moment magnifiers, respectively. One instability failure occurred for the case of L/r =100 and $C = 0.6 f'_c A_g$. This failure occurred when K_θ = 5*10^{3}kN·m/rad, but is not shown in Figure 5.14 c), since the both the positive and negative moment magnifiers exceeded 3 and so are not realistic in practice. For this case, if K_θ is reduced to 0, the member will buckle due to the applied axial load alone and cannot resist any applied vertical load.

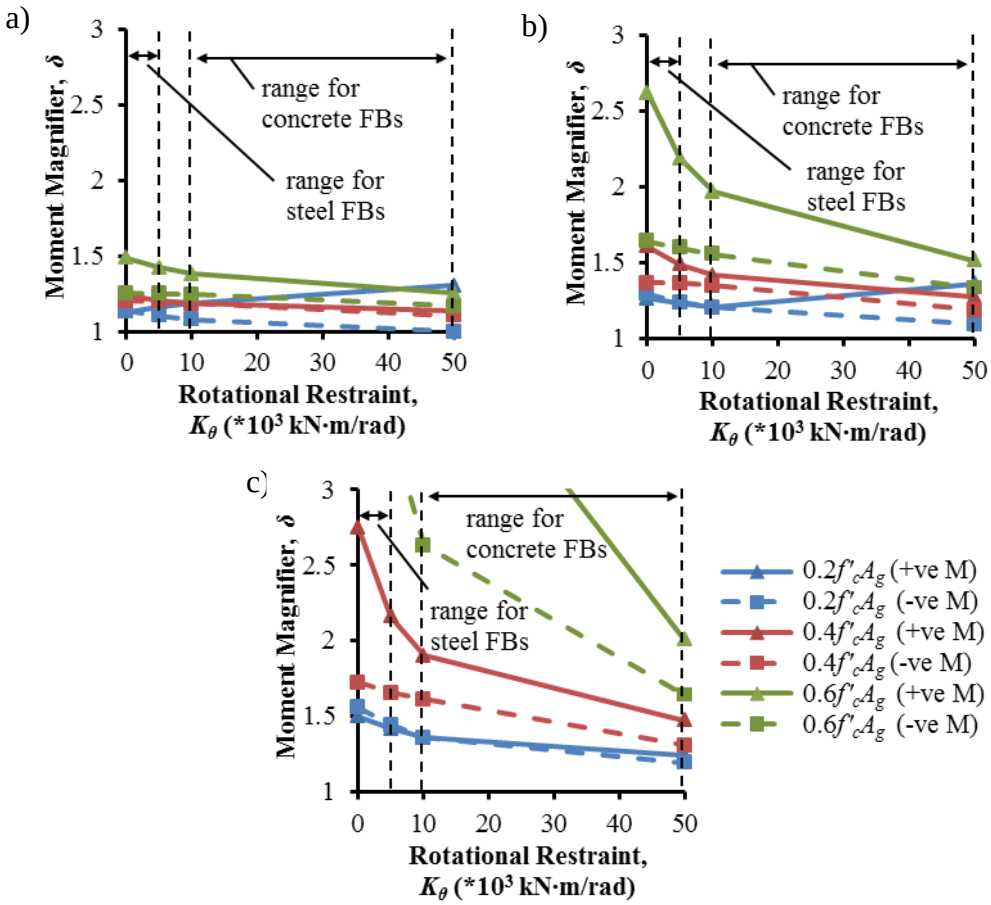

Figure 5.14: Moment magnifiers from a nonlinear-cracked first-order analysis for various floorbeam rotational restraints; a) L/r = 60; b) L/r = 80; c) L/r = 100.

Increasing the rotational restraint, K_θ, generally decreases the moment magnifier, which is consistent with Eq. [5.1]. Increasing K_θ from 0 to 50*10^{3}kN·m/rad reduces the effective length factor, k, from 1 to a minimum of 0.65 if the stiffness of the deck slab is reduced to account for cracking, as discussed in Chapter 3. However, as shown in Figure 5.14 a), the effect is relatively minor when L/r=60. The dashed vertical lines represent the upper- and lower-bound K_θ values for the steel floorbeams in the Alex Fraser Bridge and the concrete T-beams of the Talmadge Memorial Bridge, computed in Chapter 3 and scaled down for a 1m wide slab. The upper-bound value for the concrete floorbeams was

calculated using a realistic effective flange width, b_e, computed using Clause 13.8.2.7 of CSA A23.3-04 (CSA, 2004). As shown, increasing K_θ within the range of steel floorbeams only has a significant effect when the positive moment magnifiers at K_θ=0 are greater than 2, and so is not realistic in practice. However, increasing K_θ within the range expected for concrete floorbeams can reduce the positive moment magnifiers significantly, as shown by the green lines is Figure 5.14 b) and the red lines in Figure 5.14 c).

These effects are much less noticeable when the applied axial load is $0.2 f'_c A_g$ and for members with slenderness ratios of 60 or 80, shown in Figures 5.14 a) and b) respectively, the positive moment magnifiers increase slightly as K_θ increases. At this load, the support moments reach the cross-section capacity before the moments at midspan, but since the applied axial load is below the balanced failure load, plastic moment redistribution is assumed to occur. Increasing K_θ increases the negative support moments and so causes plastic redistribution to initiate at lower applied vertical loads. Thus more of the second-order support moments are redistributed to midspan, increasing the positive moment magnifiers. This response is not shown in Figure 5.14 c), because plastic redistribution is very limited when the slenderness ratio is 100. Members this slender undergo significant deflections as the support moments approach the cross-section capacity that lead to large second-order effects causing failure before plastic redistribution can occur.

Figure 5.15 shows the ratio of the moment magnifier computed using a linear-uncracked analysis, δ_L, to those computed using the nonlinear-cracked analysis, δ_{NL}, for the members with L/r = 60. The linear-uncracked analysis provides consistently better approximations of the first-order moments as K_θ is increased, since this increases the negative moments at the supports and so reduces the moments at midspan. Since the first-order moments at midspan are reduced, the linear-uncracked analysis provides better approximations of the nonlinear-cracked first-order moments, as explained in Section 5.4. This is most noticeable for $0.2 f'_c A_g$, shown by the blue lines, since the difference between the two analyses is largest at K_θ=0 but reduces considerably as K_θ increases.

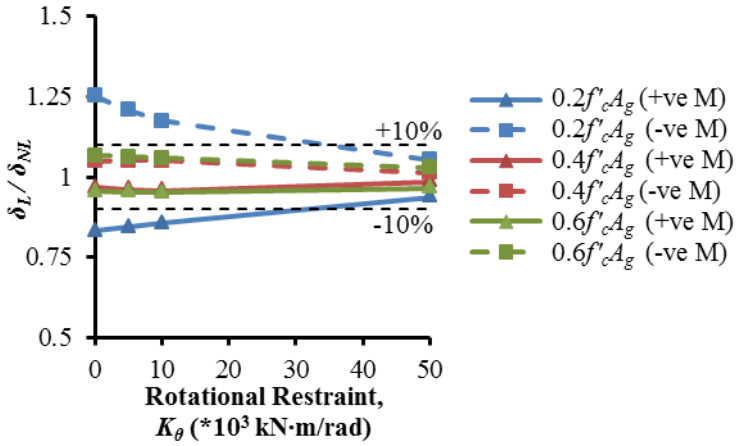

Figure 5.15: Ratio of moment magnifiers computed using a linear-uncracked first-order analysis and a nonlinear-cracked first-order analysis for various rotational restraints; *L/r* = 60.

The results shown in Figures 5.14 and 5.15 were also computed for f'_c = 40MPa and similar trends were observed. The ranges of parameters in the fourth row of Table 5.1 were also investigated for the single-point-load case and the results for f'_c = 55MPa are shown in Figures D.6 and D.7 in Appendix D. No plastic redistribution occurred in the

single-point-load case, since it creates smaller negative first-order moments, as described in detail in Section D.4. Another difference is that increasing K_θ has less influence on the accuracy of the linear-uncracked analysis for the single-point-load case, again because it creates smaller negative first-order moments. When $K_\theta = 50*10^3$kN·m/rad, the accuracy of the linear-uncracked analysis is better for the two-point-load case, shown in Figure 5.15, than for the single-point-load case, shown in Figure D.7. At all other K_θ values the linear-uncracked analysis is more accurate for the single-point-load case. When the restraint is increased to $50*10^3$kN·m/rad, the relative stiffness ratio, Ψ, from Eq. [3.1] is reduced to 0.7 for the members with a slenderness ratio of 60, if the rigidity of the deck slab is assumed to equal the uncracked rigidity. For both load cases, the linear-uncracked analysis provided acceptable results when the Ψ value is less than or equal to 0.7, for all members that were investigated.

5.8 *CSDECK* RESULTS FOR VARIOUS REINFORCING RATIOS AND STEEL DEPTHS

Figures 5.16 a) and b) show the variation of the moment magnifier with the reinforcing ratio, ρ_g, for the 240mm deck slab considered previously with f'_c = 55MPa and L/r = 80. In Figure 5.16 a), the first-order moments were computed using the nonlinear-cracked analysis, while the first-order moments in Figure 5.16 b) were computed using the linear-uncracked analysis. As with the previous investigations, applied axial load ratios of 0.2, 0.4, and 0.6 were investigated and the dashed and solid lines represent the negative and positive moment magnifiers, respectively.

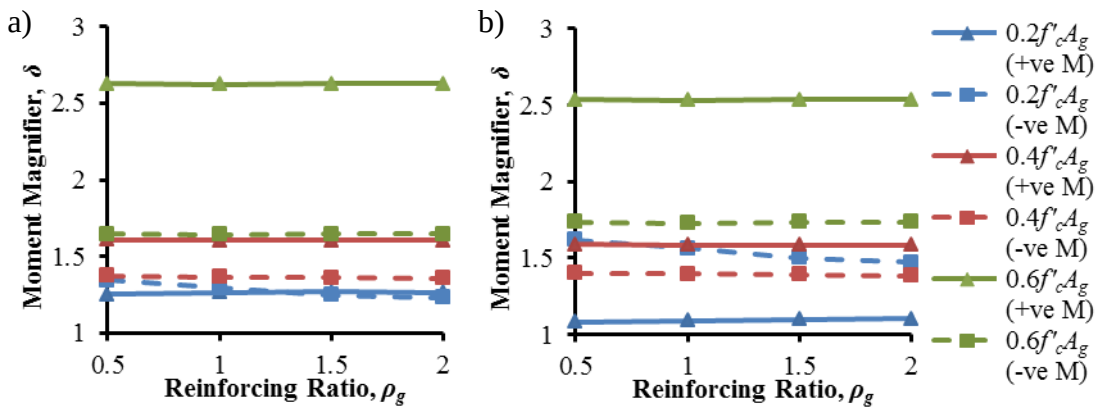

Figure 5.16: Moment magnifiers for various reinforcing ratios when L/r = 80, using: a) nonlinear-cracked first-order moment diagram; b) linear-uncracked first-order moment diagram.

Increasing ρ_g from 0.5 to 2% has a negligible influence on the moment magnifiers, as indicated by the horizontal lines in Figure 5.16. At low applied axial loads when the reinforcement is most effective, there is a slight tendency for the negative moment magnifiers to reduce as ρ_g increases, but this can be considered negligible. At higher applied axial loads, above that corresponding to a balanced failure, the reinforcement cannot yield and so is less effective.

Figures 5.17 a) and b) show the variation of the moment magnifier with the steel-depth-to-slab-thickness ratio, d/h_s, for the deck slab considered previously with f'_c = 55MPa and L/r = 80. In Figure 5.17 a), the first-order moments were computed using the nonlinear-cracked analysis and the first-order moments in Figure 5.17 b) were computed using the linear-uncracked analysis. Again, at low applied axial loads there is a very slight tendency for the negative moment magnifiers to reduce as d/h_s increases, but the effect is negligible and disappears for applied axial loads greater than the balanced failure load, when the steel is less effective.

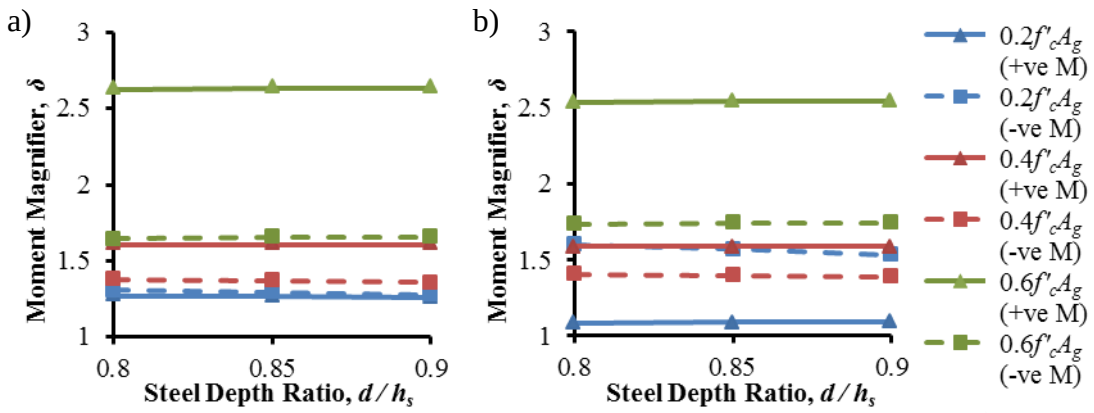

Figure 5.17: Moment magnifiers for various steel-depth-to-slab-thickness ratios when L/r = 80, using the following first-order analyses: a) nonlinear-cracked; b) linear-uncracked.

The results shown in Figures 5.16 and 5.17 were also computed for L/r = 60, as shown in Table 5.1, and again all of the lines were horizontal. Figures D.8 and D.9 in Appendix D show for the single-point-load case results similar to those shown in Figures 5.16 and 5.17 for the two-point-load case. It can be concluded that the reinforcing ratio, ρ_g, and the steel-depth-to-slab-thickness ratio, d/h_s, do not influence moment magnification in slender cable-stayed bridge decks.

5.9 ACCURACY OF SIMPLIFIED DESIGN METHODS

Table 5.2 compares the maximum total positive and negative moments computed using *CSDECK*, M^*, to the approximate magnified moments, M_c, computed using the moment magnifier equation, Eq. [1.6], neglecting the 0.75 reduction factor in Eq. [1.7]. The results shown are for the cases with slenderness ratios of 60. The rigidity, EI, was computed using Eq. [1.8] (CSA, 2006) and Eq. [2.3] (Olendzki, 2008). The accuracy of these equations is investigated using the ratio of the magnified moments obtained from the moment magnifier equation to the more accurate values obtained from *CSDECK*,

M_c/M^*. Values of this ratio greater than 1.0 are conservative. For applied axial loads of $0.3 f'_c A_g$ or less, the use of Eq. [1.8] yields magnified positive moments that are 1.5 to 4.2 times larger than the maximum total positive moments obtained from *CSDECK* and yields magnified negative moments that are 1.0 to 3.2 times larger than those computed using *CSDECK*. For larger applied axial loads, the use of Eq. [1.8] indicates that the member will buckle due to the applied load alone so the associated M_c values are shown equal to ∞. Since the current provisions in CSA S6-06 grossly overestimate the moment magnification of the idealized deck system with a slenderness ratio of 60, they are clearly inappropriate for the design of cable-stayed bridge decks that are typically more slender in practice.

Table 5.2: Comparison of magnified moments when *L/r*=60.

$\frac{C}{f'_c A_g}$	**Maximum Positive Moments (kN·m)**					**Maximum Negative Moments (kN·m)**				
	M^*	M_c **[1.8]**	M_c **[2.4]**	$\frac{M_c}{M^*}$ **[1.8]**	$\frac{M_c}{M^*}$ **[2.4]**	M^*	M_c **[1.8]**	M_c **[2.3]**	$\frac{M_c}{M^*}$ **[1.8]**	$\frac{M_c}{M^*}$ **[2.3]**
0.1	207	320	262	1.54	1.26	-219	-213	-174	0.97	0.79
0.2	301	658	392	2.19	1.31	-303	-439	-261	1.45	0.86
0.3	330	1373	432	4.16	1.31	-283	-915	-288	3.23	1.02
0.4	323	∞	430	∞	1.33	-228	∞	-287	∞	1.26
0.5	292	∞	417	∞	1.43	-185	∞	-278	∞	1.50
0.6	232	∞	370	∞	1.60	-145	∞	-246	∞	1.70
0.7	157	∞	285	∞	1.82	-101	∞	-190	∞	1.89

The use of Eq. [2.3] (Olendzki, 2008) yields more accurate results than the use of Eq. [1.8], with magnified positive moments ranging from 26% to 82% larger than the corresponding values obtained from *CSDECK* and magnified negative moments ranging from 21% smaller to 89% larger than those computed using *CSDECK*. However, since

these errors will also increase as the slenderness ratio increases, Eq. [2.3] is also inappropriate for computing the magnified moments in slender cable-stayed bridge decks.

The moment magnifier equation, Eq. [1.6], was derived to compute the magnified moment at the mid-height of a simply supported column, subjected to equal and opposite end moments causing single curvature. However, continuous cable-stayed bridge decks subjected to traffic loads applied between the floorbeams typically develop negative moments at the supports and positive moments at midspan and so are actually bent in triple curvature. This greatly reduces the second-order effects, so the magnified moments in continuous beam-columns computed using Eq. [1.6] are generally extremely conservative, even if the rigidity, *EI*, is computed using an equation that can be unconservative for members bent in single curvature.

5.10 SUMMARY

A sensitivity analysis was performed on an idealized three-span cable-stayed bridge deck to determine parameters that significantly influence moment magnification within these members. To compute the moment magnifier, the total moment diagram, including first- and second-order moments was computed using the program *CSDECK*, described in the Chapter 4. Two approaches were adopted to compute the first-order moments: (1) a nonlinear-cracked analysis that accounts for the loss of stiffness due to cracking and material nonlinearity, following the process outlined in Section 4.3; and (2) a linear-uncracked analysis that is readily carried out in practice. Since the linear-uncracked

analysis ignores the loss of stiffness due to cracking and material nonlinearity, the accuracy of this method was also investigated.

The parameters chosen for investigation were the applied axial load ratio, $C/f'_c A_g$, the slenderness ratio, *L/r*, the concrete compressive strength, f'_c, the rotational restraint provided by the floorbeams, K_θ, the gross reinforcing ratio, ρ_g, and the steel-depth-to-slab-thickness ratio, d/h_s. The ranges of the investigated parameters were chosen to be representative of current practice. All three spans were subjected to a constant applied axial load and two applied vertical load cases were considered. The case with two vertical point loads applied to the interior span only was presented in detail in this chapter and the other case, with only one vertical point load applied to the middle of the interior span, is presented in Appendix D.

The accuracy of estimating the total moments using the moment magnifier equation, Eq. [1.6], to magnify the linear-uncracked first-order results was investigated. The rigidity, *EI*, was computed either using Eq. [1.8] (CSA, 2006) or Eq. [2.3] (Olendzki, 2008).

5.11 CONCLUSIONS

The sensitivity analysis has yielded the following conclusions:

1) For the loading conditions investigated, realistic members typically exhibit material failure at midspan, except at very low applied axial loads where the cross-section capacity is first reached at the supports and additional moments are

redistributed to midspan. In such cases the positive midspan moment rarely reaches the cross-section capacity, but material failure still occurs at the supports. The only instability failures that were observed were accompanied by very large positive moment magnifiers, δ, greater than 2. Practice is not currently sufficiently advanced to predict these large δ values accurately, so they are not expected to be realistic.

2) The applied axial load ratio, $C/f'_c A_g$, slenderness ratio, *L/r*, concrete strength, f'_c, and rotational restraint provided by the floorbeams, K_θ, were all found to influence the moment magnifier significantly, as is evident from Eq. [5.1].

3) Increasing the applied axial load ratio always increases the positive moment magnifiers. The influence of the applied axial load ratio on the negative moment magnifier depends on whether the applied axial load is less or greater than the balanced failure load. For low applied axial loads, the negative moment magnifiers increase as the applied axial load increases and have roughly the same magnitudes as the positive moment magnifiers. For higher applied axial loads, larger moments are required to crack the section and the rigidity at midspan is higher, so more moment is resisted at midspan and less at the supports, so the positive moment magnifiers are always larger than the negative moment magnifiers.

4) Increasing the slenderness ratio always increases the moment magnifier, because the midspan deflection increases and so the second-order moments also increase.

5) Increasing the concrete compressive strength, f'_c, reduces the moment magnifiers in most cases, partly because this increases the initial tangent modulus of elasticity of concrete, E_c.

6) Increasing the rotational restraint, K_θ, typically reduces the moment magnifier, though the reduction is very slight when $L/r = 60$. At higher slenderness ratios, increasing K_θ within the range expected for steel floorbeams does not have a significant effect on realistic members, so K_θ for steel floorbeams can be neglected. However, increasing K_θ within the range of values expected for concrete floorbeams can reduce the moment magnifier significantly and so should be considered in practice.

7) The reinforcing ratio, ρ_g, and the ratio of the steel-depth-to-slab-thickness, d/h_s, have a negligible influence on the moment magnifiers, even at low applied axial loads when the steel is most effective.

8) The linear-uncracked first-order analysis always underestimates the positive moment magnifiers and overestimates the negative moment magnifiers. The linear-uncracked analysis overestimates the rigidity along the length of the interior span and so underestimates the rotations and negative moments at the supports. If the applied axial load is less than the balanced failure load, the linear-uncracked analysis will not accurately predict first-order moments, unless either the slenderness ratio is very large, $L/r \gtrsim 110$, or there is significant rotational

restraint provided by the floorbeams, $\Psi \lesssim 0.7$, since the combined effects of concrete cracking and steel yielding cause the first-order rigidity to be significantly less than the uncracked rigidity. These effects are negligible at any slenderness ratio when the applied axial load is from $0.4 f'_c A_g$ to $0.5 f'_c A_g$.

9) For high applied axial loads, $C \gtrsim 0.6 f'_c A_g$, the initial uncracked secant rigidity obtained from the actual moment-curvature relationship is less than that assumed in the linear-uncracked analysis, but it still provides acceptable predictions of the nonlinear-cracked first-order moments, provided the slenderness ratio is not less than 70.

10) The procedures provided in CSA S6-06 for computing second-order effects in slender concrete beam-columns are excessively conservative even for a relatively stocky cable-stayed bridge deck section (L/r=60), so these provisions cannot be used to design realistic decks that are often more slender.

11) The moment magnifier equation, Eq. [1.6], is not acceptable for approximating the second-order effects in continuous cable-stayed bridge decks bent in triple curvature, since it was derived for simply supported members bent in single curvature. Even when the least conservative equation investigated in Chapter 2, Eq. [2.3] (Olendzki, 2008), is used to compute *EI* in Eq. [1.6], the results are conservative overestimating the moment magnification by at least 26%.

CHAPTER 6: SUMMARY AND CONCLUSIONS

6.1 SUMMARY

Cable-stayed bridge girder systems often consist of a concrete deck slab supported by steel or concrete floorbeams that span transversely between the longitudinal steel or concrete girders. The deck slab is subjected to local bending moments from traffic loads, compression forces due to global bending of the longitudinal girder, and additional compression forces from the horizontal component of the stay cable tensions. The deck slabs must therefore be designed as slender beam-columns since their slenderness ratios can exceed 70 in practice (e.g. Bartlett, 1991). The current provisions in CSA S6-06 for second-order effects in slender beam-columns were derived for columns in buildings where slenderness effects can often be neglected (MacGregor, Breen, & Pfrang, 1970), so their suitability for extremely slender cable-stayed bridge decks warrants investigation.

The different failure modes for slender beam-columns were presented in Chapter 1 and the difference between the secant and tangent rigidities was demonstrated using a typical moment-curvature relationship. Results presented by Bartlett (1991) were used to demonstrate the inaccuracy associated with using the provisions in CSA S6-06 (CSA, 2006) for computing the resistance of slender concrete beam-columns to design cable-stayed bridge decks.

A detailed review of eight equations proposed in the literature for computing the rigidity, *EI*, of slender concrete columns was presented in Chapter 2. The limitations of each equation were discussed and the influences of the key variables in each equation were

compared. The accuracy associated with the eight equations was investigated through a case study of the deck slab in the Alex Fraser Bridge in Vancouver. Rigidities computed using each equation were used to determine the deck slab capacity and these results were compared to those from the second-order analysis discussed in Chapter 4.

The rotational restraint provided at the deck slab supports by steel or concrete transverse floorbeams was examined and approximate equations were presented in Chapter 3 to quantify the restraint provided. The equations account for the restraint provided by the torsional stiffness of the floorbeams and the additional restraint provided by the vertical eccentricity of the rigid deck slab with respect to the floorbeam centroid. The equations were validated using a linear-elastic static analysis performed in SAP2000. Typical ranges of effective length factors, *k*, were then computed using the validated equations for deck slabs supported by steel and concrete floorbeams, using case studies of the Alex Fraser Bridge and the Talmadge Memorial Bridge in Savannah, Georgia.

A rational method was presented for computing the first- and second-order moments in continuous beam-columns subjected to vertical loads between their supports in Chapter 4. The method was implemented into a MATLAB program to analyze a simplified three-span cable-stayed bridge deck subjected to axial compression in all three spans and vertical loads at the interior span only. The program was then used to compute the second-order effects in a simplified deck system resembling that of the Talmadge Memorial Bridge and was validated using both a nonlinear-static analysis performed in ANSYS 12.0 and a nonlinear analysis program developed by Nathan (1987).

A sensitivity analysis was presented in Chapter 5 that determines the influence of the following parameters on the moment magnification of slender cable-stayed bridge decks: the applied axial load ratio, $C/f'_c A_g$, the slenderness ratio, *L/r*, the concrete strength, f'_c, the rotational restraint provided by the floorbeams, K_θ, the reinforcing ratio, ρ_g, and the ratio of the reinforcement depth to slab thickness, d/h_s. Two loading conditions were investigated and the moment magnifiers were computed using two different methods to compute the first-order moments. Nonlinear-cracked analysis accounted for the variation in rigidity along the length of the slab, but was deemed to be difficult to carry out in practice. Linear-uncracked analysis is more readily carried out in practice, but idealizes the rigidity along the length of the member as constant and equal to the uncracked rigidity. Since the linear-uncracked analysis does not account for the variation in rigidity, its accuracy was also investigated. Furthermore, the accuracy of the moment magnifier equation, Eq. [1.6], for estimating the maximum total positive and negative moments by magnifying the linear-uncracked first-order moments was investigated, using both Eq. [1.8] (CSA, 2006) and Eq. [2.3] (Olendzki, 2008) to compute *EI*.

6.2 CONCLUSIONS

The main conclusions of this investigation are as follows:

1) The equations provided by CSA S6-06 for computing the rigidity, *EI*, of slender concrete members provide acceptable results at a low applied axial load and extremely conservative results at a higher applied axial load for a slender simply supported cable-stayed bridge deck subjected to equal and opposite end moments.

These equations are excessively conservative at all applied axial loads for continuous members subjected to transverse loads between their supports.

2) The various equations proposed in the literature to compute *EI* generally yield conservative estimates that are less accurate than the equations in CSA S6-06 at low axial loads. All yield more accurate, but still conservative estimates at higher axial loads, from 7 to 100% less than the capacity obtained from a detailed second-order analysis for a simply supported cable-stayed bridge deck subjected to equal and opposite end moments. The equation proposed by Olendzki (2008) was the only equation to provide unconservative results, underestimating the capacity by 20% at the lower applied load, but yielded an accurate prediction at the higher applied load, within 8% of the results from the detailed analysis. The method proposed by Khuntia and Ghosh (2004) provided the most consistent results with accurate predictions at both low and high applied axial loads, underestimating the capacity by 5 and 7%, respectively.

3) The moment magnifier equation, Eq. [1.6], yields very conservative estimates of the second-order effects in continuous beam-columns subjected to transverse loads between their supports. Using Eq. [2.3] (Olendzki, 2008) to compute *EI* in Eq. [1.6] can overestimate the capacity of simply supported members subjected to equal end moments causing single curvature by up to 20%, but greatly underestimates the capacity of continuous members bent in triple curvature.

4) The rotational restraint provided by the vertical eccentricity between the deck slab and the floorbeam centroid can significantly increase the total rotational restraint provided. It has a negligible influence, however, on the effective length factor, *k*, for steel floorbeams and reduced *k* by at most 11% for concrete floorbeams.

5) The effective length factor, *k*, for cable-stayed bridge deck slabs supported by steel floorbeams approaches 1. However, the rotational restraint provided by concrete floorbeams can reduce *k* below 0.9, typically from 0.6 to 0.85 for realistic cases. The difference in restraint provided by steel and concrete floorbeams is due to thin steel elements being ineffective at resisting St. Venant Torsion.

6) Realistic cable-stayed bridge deck slabs subjected to either a single point load applied between the supports or two point loads applied at the third points reach material failure at midspan, provided the cross-section capacity is not first reached at the supports. Instability failures are only anticipated when the maximum positive moment at midspan is magnified by a factor of more than two. Given the accuracy of current practice, a designer is likely to be leery of moment magnifiers of this magnitude and so they are not expected to be realistic in practice.

7) The applied axial load ratio, $C/f'_c A_g$, slenderness ratio, *L/r*, concrete strength, f'_c, and rotational restraint provided by the floorbeams, K_θ, influence the moment magnification of cable-stayed bridge decks significantly. The

reinforcement ratio, ρ_g, and the ratio of the reinforcement depth to slab thickness, d/h_s, have a negligible influence, even at low applied axial loads when the steel is most effective.

8) Increasing the applied axial load ratio always increases the positive moment magnifiers. The influence of the applied axial load ratio on the negative moment magnifiers is different at applied axial loads below and above the balanced failure load. At low applied axial loads, the negative moment magnifiers increase as the applied axial load increases and are roughly the same in magnitude as the positive moment magnifiers. At higher applied axial loads the positive moment magnifiers are larger than the negative moment magnifiers, since larger moments are required to crack the section and the reinforcement cannot yield so the midspan rigidity is much larger than at lower applied axial loads.

9) Increasing the slenderness ratio increases the moment magnifier, since the deflection midspan between the floorbeams increases and so the second-order moments also increase. The difference between the positive and negative moment magnifiers at applied axial loads above the balanced failure load increases further as the slenderness ratio increases, since the negative support moments are reduced.

10) Increasing the concrete compressive strength, f'_c, reduces the moment magnifiers in most cases, since it increases the initial tangent modulus of

elasticity, E_c, and also reduces the applied axial load ratio, $C/f'_c A_g$, which was shown to reduce the moment magnifier, except near balance point.

11) Increasing the rotational restraint, K_θ, typically reduces the moment magnifier, though the reduction is very minor when L/r = 60. At higher slenderness ratios, increasing K_θ within the range expected for steel floorbeams does not have a significant effect on realistic members. However, increasing K_θ from 0 to the largest value considered for concrete floorbeams reduces the moment magnifier significantly: in some cases it can reduce the positive moment magnifier from greater than 2.5 to a value near 1.5.

12) A linear-uncracked first-order analysis always underestimates the positive moment magnifiers and overestimates the negative moment magnifiers, since it overestimates the rigidity along the length of the interior span and so underestimates the rotations and negative moments at the supports.

6.3 RECOMMENDATIONS FOR DESIGN OFFICE PRACTICE

The following recommendations can be made for design office practice:

1) The procedures provided in CSA S6-06 for computing second-order effects in slender concrete beam-columns are excessively conservative and so cannot be used to design economical cable-stayed bridge decks.

2) The moment magnifier equation, Eq. [1.6], is not acceptable for approximating the second-order effects in continuous cable-stayed bridge decks bent in triple curvature, since it was derived for simply supported members bent in single curvature.

3) The rotational restraint provided by the vertical eccentricity between the deck slab and the floorbeam centroid can be neglected when computing the rotational restraint of steel or concrete floorbeams.

4) Increasing the rotational restraint, K_θ, within the range typical of steel floorbeams has a negligible effect on both the moment magnifier and the effective length factor for realistic cases, so K_θ for steel floorbeams can be neglected.

5) Increasing K_θ within the range of values expected for concrete floorbeams can reduce both the moment magnifier and the effective length significantly, so neglecting the restraint in practice may result in an uneconomical solution.

6) Linear-uncracked analysis should provide acceptable predictions of the nonlinear-cracked first-order moments at any slenderness ratio when the applied axial load is from $0.4 f'_c A_g$ to $0.5 f'_c A_g$.

7) At high applied axial loads, $C \gtrsim 0.6 f'_c A_g$, the linear-uncracked analysis provides acceptable predictions of the nonlinear-cracked first-order moments, provided the slenderness ratio is not less than 70.

8) If the applied axial load is less than the balanced failure load, the linear-uncracked analysis will not accurately predict first-order moments, unless either the slenderness ratio is very large, $L/r \gtrsim 110$, or there is significant rotational restraint provided by the floorbeams, $\Psi \lesssim 0.7$.

6.4 RECOMMENDATIONS FOR FUTURE WORK

The recommendations for future work are as follows:

1) Review past designs to determine the ranges of cross-section dimensions, material properties, and loading conditions that are typical in practice and compare these ranges to those used in Chapter 5.

2) Explore the effects of more realistic loading conditions, consisting of a CL-625W truck driven across the deck slab and compare the results to the results from the two load cases investigated in Chapter 5.

3) Determine the influence of tension stiffening on the moment magnification of cable-stayed bridge decks subjected to low applied axial loads, where the effects of cracking are most significant.

4) Investigate time-dependent effects to determine their influence on the response of slender cable-stayed bridge decks. These effects, such as creep, can be expected to reduce the rigidity of the deck slab and so increase the second-order effects. In the case of composite girder systems with steel edge girders, creep will also cause

some of the axial load in the deck slab to be shed to the steel girders, which will also affect the moment magnification.

REFERENCES

American Concrete Institute. 2008. *Building code requirements for reinforced concrete, (ACI 318-08)*, Detroit, Michigan.

American Concrete Institute. 2002. *Building code requirements for reinforced concrete, (ACI 318-02)*, Detroit, Michigan.

Anderson, A.R., & Moustafa, S.E. 1970. Ultimate strength of prestressed concrete piles and columns, *American Concrete Institute Journal*, Vol. 37, No. 8, pp. 620-635.

ANSYS Inc. 2009. ANSYS Version 12.0. Canonsburg, Pennsylvania, U.S.A.

Bartlett, F.M. 1991. Instability of reinforced concrete beam-columns. *Proceedings, CSCE Annual Conference*, Vancouver, II, pp. 22-31.

Bergman, D. 2011. Personal communication.

Bonet, J.L., Romero, M.L., & Miguel, P.F. 2011. Effective flexural stiffness of slender reinforced concrete columns under axial forces and biaxial bending, *Engineering Structures*, Vol. 33, pp. 881-893.

Canadian Standards Association. 2006. *Canadian highway bridge design code (CAN/CSA S6-06)*, CSA, Mississauga, Ontario, pp. 203, 329.

Canadian Standards Association. 2004. *Design of concrete structures (CAN/CSA A23.3-04)*, CSA, Rexdale (Toronto), Canada, pp. 47, 86.

CBA – Buckland & Taylor Ltd. 1983. Annacis Bridge – Steel alternative, *Government of British Columbia Ministry of Transportation and Highways Bridge Engineering Branch*.

Collins, M.P., & Mitchell, D. 1990. *Prestressed Concrete Structures*. Prentice Hall, Englewood Cliffs, N.J., 776 pp.

Computers & Structures Inc. 2011. SAP2000 Version 15.0. Berkeley, California, U.S.A.

European Committee for Standardization. 2004. *Eurocode 2: design of concrete structures—part 1: general rules and rules for buildings, (EN 1992-1-1)*.

Gimsing, N. J., & Georgakis, C.T. 2012. Cable supported bridges, concept and design – Third Edition. *John Wiley & Sons Ltd., West Sussex*, 310pp.

Hauge, L., & Anderson, E. Y. 2011. Keynote lecture – Longer..., *IABSE-IASS Symposium, London*, pp. 8-16.

Hibbeler, R.C. 2009. *Structural analysis*: *Seventh Edition*. Prentice Hall/Pearson Education Canada Inc., Upper Saddle River, New Jersey, pp. 318-327.

Hsu, T.T.C. 1968. Torsion of structural concrete - behaviour of reinforced concrete rectangular members, *Torsion of Structural Concrete*, ACI Publication SP-18, American Concrete Institute, Detroit, pp. 261-306.

Khuntia, M., & Ghosh, S.K. 2004. Flexural stiffness of reinforced concrete columns and beams: analytical approach and experimental approach, *American Concrete Institute Structural Journal*, Vol. 101, No. 3, pp. 351-374.

Lopez, M. 2005. Creep and shrinkage of high performance lightweight concrete: a multi-scale investigation, *Thesis submitted in partial fulfilment of the Ph.D. degree*, Georgia Institute of Technology, Atlanta, 531pp.

MacGregor, J.G., & Bartlett, F.M. 2000. *Reinforced concrete mechanics and design*: *First Canadian Edition*. Prentice Hall/Pearson Education Canada Inc., Toronto, Ontario, 1042pp.

MacGregor, J., Breen, J., & Pfrang, E. 1970. Design of slender concrete columns, *American Concrete Institute Journal*, Vol. 67, No. 1, pp 6-28.

Nathan, N.D. 1972. Slenderness of prestressed concrete beam-columns. *Prestressed Concrete Institute Journal*. Vol. 17, No. 6, pp. 45-57.

Nathan, N. D. 1983. Slenderness of prestressed concrete columns, *Prestressed Concrete Institute Journal*, Vol. 28, No. 2, pp. 50-77.

Nathan, N.D. 1985. Rational analysis and design of prestressed concrete beam columns and wall panels, *Prestressed Concrete Institute Journal*, Vol. 30, No. 3, pp. 82-133.

Nathan, N.D. 1987. A computer program for the rational analysis of beam columns. pp. 1-43.

Olendzki, P. 2008. Flexural stiffness to estimate the moment magnification for slender reinforced concrete columns, *Thesis submitted in partial fulfilment of the M.E.Sc. degree*, University of Western Ontario, London, 119pp.

PCI Committee on Prestressed Concrete Columns. 1988. Recommended practice for the design of prestressed concrete columns and walls, *Prestressed Concrete Institute Journal*, Vol.33, No. 4, pp. 56-81.

Przemieniecki, J.S. 1968. *Theory of matrix structural analysis*. McGraw-Hill Inc., New York, N.Y., pp. 388-391.

Salonga, J.A. 2010. Innovative systems for arch bridges using ultra high-performance fibre-reinforced concrete. *Thesis submitted in partial fulfilment of the Ph.D. degree*, University of Toronto, Toronto, 335pp.

Schemmann, A., Bergman, D., & Shafer, G. 2011. Design-build of the longest cable-stayed span in the Americas John James Audubon Bridge, *Proceedings of IABSE –IASS Symposium, London*, International Association for Bridge and Structural Engineering, Zurich, No. 434.

Shuraim, A.B. 1990. Slenderness effects in prestressed concrete columns, *Dissertation submitted in partial fulfilment of the PhD degree*, University of Michigan, Ann Arbor, 285pp.

Shuraim, A.B, & Naaman, A.E. 2003. A new design methodology for the ultimate capacity of slender prestressed concrete columns, *Prestressed Concrete Institute Journal*, Vol. 48, No. 1, pp. 64-80.

The Mathworks Inc. 2011. MATLAB R2011b. Natick, Massachusetts, U.S.A.

Thorenfeldt, E., Tomaszewicz, & Jensen, J.J. 1987. Mechanical properties of high-strength concrete and application in design. *Proceedings of the Symposium "Utilization of High-Strength Concrete,"* Stavanger, Norway, pp. 149-159.

Tikka, T.K., & Mirza S.A. 2008. Effective flexural stiffness of slender structural concrete columns, *Canadian Journal of Civil Engineering*, Vol. 35, pp. 384-399.

APPENDIX A: BASIS OF RIGIDITY EQUATIONS PROPOSED BY OTHERS

Equation [2.1] was proposed by Nathan (1983) to improve the accuracy of the moment magnifier equation, Eq. [1.6], for prestressed concrete columns. Nathan (1983) observed prestressed concrete columns are often governed by instability throughout most of their practical slenderness range, since they typically have lower reinforcing ratios, higher slenderness ratios, and higher axial loads at balanced failure than typical reinforced concrete columns. However, cable-stayed bridge deck panels are also very slender and have low reinforcing ratios, which can cause relatively high axial loads at balanced failure. Prestressed wall panels typically carry relatively low axial loads and are usually statically determinate, however, whereas cable-stayed deck panels can be subjected to large axial loads and are typically indeterminate.

Equation [2.1] was developed by back-calculation from the results obtained from a rational computer analysis. It is intended to apply to prestressed columns when the concrete stress due to prestressing is less than 4 MPa, the initial prestressing is greater than 50% of the ultimate strand stress, and the slenderness ratio, kL/r, is less than 150. It is not intended to represent the secant rigidity or the tangent rigidity, but instead to provide an artificial rigidity that simulates instability failures as equivalent material failures, as suggested by the interaction diagram shown in Figure A.1. The true load path, from the origin to the actual mid-height moment, $M_{c,A}$, is simulated using a fictitious load path, from the origin to the simulated mid-height moment, $M_{c,S}$. The end moment at instability, M_2, can then be approximated by over-estimating the second-order effects, $M_2(\delta - 1)$, using the simulated mid-height moment, $M_{c,S}$, equal to the cross-section

capacity, and the proposed rigidity equations. The equations therefore intentionally underestimate the true secant rigidity when instability occurs.

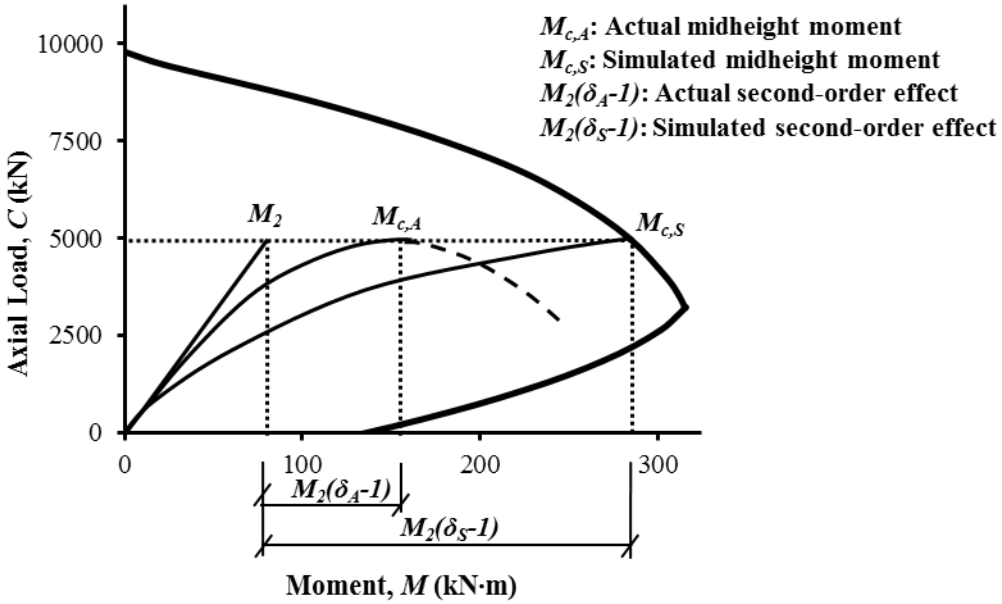

Figure A.1: The real load path of a stability failure and the simulated load path assumed by Nathan (after Nathan, 1983).

However, Nathan (1985) observed that Eq. [2.1] does not produce acceptable results if either the member resistance factor, ϕ_m, taken to be 0.75 in CSA S6-06, or the sustained load factor, β_d, is included. Equation [2.1] is therefore recommended if the short-term nominal response is desired (i.e. $\beta_d = 0$, $\phi_m = 1.0$), and Nathan (1985) proposed Eq. [A.1] and [A.2] for the factors, η and Ω, to replace those in the right column of Table 2.1 when the long-term factored response is required. For $0 \leq \beta_d \leq 0.5$ and $\phi_m = 0.75$:

[A.1] $$\eta = 2.5 + \frac{1.6}{C_f / C_o}$$

where $6 \leq \eta \leq 70$. For sections without compression flanges with the same range of β_d and value of ϕ_m:

[A.2] $$\Omega = \frac{27}{kL/r} - 0.05$$

and $\alpha = \eta\Omega$ should not be taken less than 3.2. The PCI Committee on Prestressed Concrete Columns (1988) adopted Eq. [2.1] for calculating *EI*, with η and Ω defined by Eqs. [A.1] and [A.2], and proposed that α should not be taken less than 3.

Khuntia and Ghosh (2004) proposed Eq. [2.2] as the flexural rigidity for analyzing sway frames and non-sway frames, and specifically for analyzing frames with slender columns. Equation [2.2] provides the secant rigidity of typical cross sections and was developed to reduce the ambiguities between the two frame analysis methods in ACI 318-02 (ACI, 2002), which are very similar to those in CSA S6-06. Equation [2.2] was validated using test results reported in the literature and the predictions were compared extensively to those obtained from Eq. [1.8] and from a form of Eq. [1.9] that appeared in previous editions of CSA S6. Based on the experimental results investigated, Eq. [2.2] predicts the slender column capacity much more accurately. The tests used to validate Eq. [2.2] for analyzing columns in non-sway frames bent in single curvature had slenderness ratios from 31 to 61, which are less than the typical range of slenderness ratios in cable-stayed bridge deck panels and much less than the slenderness limit of 100 in CSA S6-06.

Equation [2.2] is based on the assumptions that when subjected to typical factored loads that are less than the factored resistances, the maximum compression strain in the concrete does not exceed 0.0015 and the tension steel is unlikely to yield. However, the effective flexural rigidity required in the moment magnifier equation, Eq. [1.6], must represent the secant rigidity immediately prior to failure (MacGregor & Bartlett, 2000), which is defined by CSA S6-06 to occur at an extreme fibre compression strain, ε_{cu}, of 0.0035.

Figure A.2 shows the moment resistance, M_u, as a function of the extreme fibre compression strain for a 400mm square column with f'_c=30MPa and ρ_g=2%. The symbol X marks the yield moment of the section. The maximum applied load of $0.5C_o$ exceeds the load at balanced failure, so yielding does not occur and the maximum moment resistance corresponds to an extreme fibre strain of approximately 0.0025. For the lower applied axial loads of $0.125C_o$ and $0.25C_o$, the yield moments occur at extreme fibre strains of 0.00175 and 0.0025, respectively. In both cases the yield moment exceeds 97% of the maximum moment resistance, so the moment resistance remains essentially constant as the extreme fibre strain increases to 0.0035. Thus for this cross section, the secant rigidity should be computed for a maximum extreme fibre strain of 0.0025: for higher strains, the moment remains essentially constant but the curvature increases by at least 40% so the secant rigidity reduces by at least 30%. Adopting the Khuntia and Ghosh proposal that the extreme fibre strain does not exceed 0.0015 seems inappropriate, however, because this corresponds to only 86%, 68%, and 64% of the maximum moment resistance for loads of $0.125C_o$, $0.25C_o$, and $0.5C_o$, respectively. However, Eq. [2.2] was

intended to apply to both serviceability and ultimate limit states, and much lower extreme fibre strains can be expected under service loads.

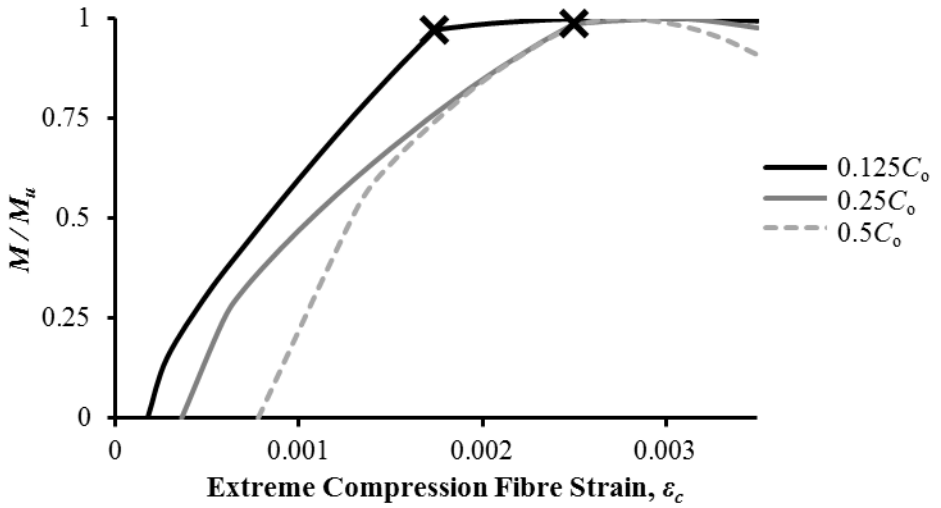

Figure A.2: The moment resistance vs. extreme fibre compressive strain relationship for a 400mm square column, f'_c = 30MPa and ρ_g = 2%.

Equation [2.3], suggested by Olendzki (2008), was derived from a statistical analysis of 275 slender reinforced concrete column tests reported in the literature and is intended to provide an equivalent column flexural rigidity that is more accurate than Eqs. [1.8] and [1.9]. It is unclear whether Eq. [2.3] is intended to represent the secant or tangent rigidity, and the failure modes of the reported tests are not discussed. Equation [2.3] can therefore be assumed to provide an equivalent flexural rigidity that minimizes the statistical error of the test-to-predicted ratios. All of the tested columns had slenderness ratios, *kL*/*r*, less than 100 and so are slender columns as per CSA S6-06. Equation [2.3] is therefore restricted to same slenderness ratio limit of 100 that currently applies to Eqs. [1.8] and [1.9] in CSA S6-06.

Tikka and Mirza (2008) proposed Eqs. [2.4] and [2.5] to compute the effective flexural rigidity for slender reinforced concrete and composite columns, where the end eccentricity ratio, *e*/*h*, is not taken less than 0.1. Equations [2.4] and [2.5] were developed by regression analysis of the theoretical flexural rigidity at simulated material failure of over 27,000 reinforced concrete and composite columns. The cross-section capacity, M_u, was taken as the maximum from the moment-curvature relationship. The theoretical rigidity was then determined using the secant formula, assuming the mid-height moment reached M_u. Equations [2.4] and [2.5] are intended to apply when the slenderness ratio, *kL*/*r*, is less than 104, the concrete compressive strength, f'_c, is less than 55MPa, and the gross reinforcing ratio, ρ_g, is greater than 1%. Given that the precast deck panels in both the Alex Fraser Bridge in Vancouver and the John James Audubon Bridge in Louisiana are made with 55MPa concrete (Schemmann et al., 2011), it is perhaps inappropriate to consider Eqs. [2.4] and [2.5] for designing deck panels since the current-state-of-practice has already exceeded these limitations.

Bonet et al. (2011) proposed Eq. [2.6] as part of a study focused primarily the flexural rigidity of members subjected to biaxial bending. Equation [2.6] was proposed for uniaxial bending and was developed by regression analysis of numerically simulated results, performed using general finite element analysis software and verified using 613 test results reported in the literature for columns subjected to both uniaxial and biaxial bending. The range of parameters investigated included: gross reinforcing ratios, ρ_g, greater than 1%; concrete compressive strengths, f'_c, from 30 to 100MPa; and slenderness ratios, *kL*/*r*, up to 100. However, Eq. [2.6] was developed to be included in

both the ACI-318 (ACI, 2008) and Eurocode 2 (European Committee for Standardization, 2004) and contains the creep coefficient, φ, from Eurocode 2 which differs from the β_d factor in CSA S6-06. Equation [2.6] is intended to apply to both material and instability failures, yet is also meant to be used in the moment magnifier equation, Eq. [1.6], with the mid-height moment equal to the cross-section capacity, M_u. Equation [2.6] is therefore intended to approximate the secant rigidity at material failure and, similar to Nathan's (1983) approach, to underestimate to secant rigidity for instability failures. The simulated second-order effects are therefore overestimated for instability failures, so they can be analyzed as equivalent material failures, similar to Eq. [2.1], as was shown in Figure A.1.

Equation [1.3] for the secant rigidity at material failure is based entirely on mechanics and is therefore applicable to all columns with linear strain distributions that reach material failure. It will always provide conservative results because the rigidity is calculated at the critical mid-height section where it is the least. Furthermore, as shown in Figure A.2, the maximum moment corresponds approximately to an extreme fibre strain, ε_{cu}, of 0.0025, so assuming a value of 0.0035 and the associated neutral axis depth, c_u, will significantly underestimate the true secant rigidity.

A variation on Eq. [1.3] suggested by Shuraim and Naaman (2003) for slender prestressed concrete columns is described in Chapter 2. As mentioned, they propose adopting the secant rigidity at the applied end eccentricity, instead of at the applied load, C_f, as shown in Figure 2.1. This assumption seems counterintuitive since this rigidity

value corresponds neither to the applied load at the critical section nor the eccentricity at the critical section. While Shuraim (1990) states that "if *EI* is calculated at the same axial load, the results will be very conservative," there is no rational explanation for this procedure other than it provides good agreement with the rigidity obtained from finite element analysis.

The computed rigidity proposed by Shuraim and Naaman (2003) was compared to the results from their finite element analysis in Figure 2.2. As previously mentioned in Chapter 2, the method greatly underestimates the rigidity at low eccentricity ratios, e/h, as demonstrated by the dashed line. Shuraim and Naaman attribute this to the failure being governed by instability at high axial loads, causing an increase in the effective rigidity at failure. However, this contradicts previous research by Nathan (1983) who noticed that prestressed columns are often governed by instability at any applied load when the slenderness ratio exceeds 50. As the applied axial load approaches the axial resistance for zero applied moment, C_o, the rigidity calculated at the applied eccentricity approaches the rigidity calculated at the applied axial load. Therefore, the method becomes more conservative as the applied load increases, approaching that of Anderson and Moustafa (1970) which gives very conservative results.

To avoid extreme conservatism at low eccentricities, Shuraim and Naaman (2003) further proposed that the rigidity should not be taken less than the peak secant rigidity, shown by point B on Figure 2.2. Equation [2.7] in Chapter 2 is proposed for computing the neutral axis depth at the peak secant rigidity and the ultimate moment resistance, M_u, corresponding to this neutral axis depth can be obtained by interpolation, provided the

neutral axis depth is known for a sufficient number of points defining the short column interaction diagram.

To further improve the accuracy of the proposed method for eccentricities less than the peak value, Shuraim and Naaman (2003) suggest that the rigidity be computed by interpolating between the peak secant rigidity, point B on Figure 2.2, and the tangent rigidity under concentric axial load, shown by the dashed line at the top of the figure. The critical tangent rigidity under concentric axial load can be obtained by equating the critical buckling load to an unknown uniform stress across the column area (Shuraim & Naaman, 2003):

[A.3] $$C_c = \frac{\pi^2 E_{tc} I_g}{kL^2} = A_g E_{sc} \varepsilon$$

The critical buckling load is defined by the concrete tangent modulus, E_{tc}, while the concrete secant modulus, E_{sc}, defines the uniform stress across the gross concrete area, A_g, corresponding to the strain, ε. For simplicity, Shuraim and Naaman propose using a simple parabolic stress-strain relationship for concrete in compression:

[A.4] $$f_c = f'_c \left[2\frac{\varepsilon}{\varepsilon_o} - \left(\frac{\varepsilon}{\varepsilon_o} \right)^2 \right]$$

where f_c is the stress corresponding to the strain, ε, and ε_o is the strain corresponding to the peak stress, f'_c. The tangent modulus, E_{tc}, can be obtained by differentiating Eq. [A.4] with respect to the strain, ε, yielding:

[2.9] $$E_{tc} = \frac{2f'_c}{\varepsilon_o}\left(1 - \frac{\varepsilon}{\varepsilon_o}\right)$$

The secant modulus, E_{sc}, can be obtained by dividing the stress by the strain. For the stress-strain relationship given by Eq. [A.4]:

[A.6] $$E_{sc} = \frac{f'_c}{\varepsilon_o}\left(2 - \frac{\varepsilon}{\varepsilon_o}\right)$$

Substituting Eq. [A.5] and [A.6] in Eq. [A.3] and solving for the strain yields Eq. [2.10] for the ultimate strain under concentric axial load:

[2.10] $$\varepsilon = \left[\varepsilon_o + \left(\frac{\pi r}{kL}\right)^2\right] - \sqrt{{\varepsilon_o}^2 + \left(\frac{\pi r}{kL}\right)^4}$$

Substituting Eq. [2.10] back into Eq. [A.5] yields the concrete tangent modulus, and the tangent rigidity under concentric axial load follows as:

[2.8] $$EI_{tan} = E_{tc} I_g$$

Figure 2.2 demonstrates that the method proposed by Shuraim and Naaman (2003) closely approximates the rigidity obtained using finite element analysis, if the secant rigidity, Eq. [1.3], corresponding to the applied end eccentricity is used at high eccentricities, and the rigidity is obtained by interpolating between the peak secant rigidity and the critical tangent, Eq. [2.8], at low eccentricities. The rigidity obtained using the proposed method is shown by the solid line with a kink at point B, which closely follows the smooth solid line representing the results from their finite element analysis.

APPENDIX B: DERIVATION OF APPROXIMATE EQUATIONS FOR COMPUTING THE ROTATIONAL RESTRAINT PROVIDED BY FLOORBEAMS

B.1 EQUATION [3.4]

From Chapter 3, the rotational restraint, K_θ, of an elastic member with fixed ends rotating about its centroid due to an applied point torque is:

[3.2] $$K_\theta = \frac{T}{\theta} = \frac{GJs}{a(s-a)}$$

where θ is the rotation at the point of application of the point torque, T, at a distance, a, from the support. The shear modulus is G, J is the St. Venant torsional constant, and s is the length of the floorbeam. If the deck slab is assumed to prevent deflection at the mid-height of the slab, the restraint provided by the deck slab, P_e, will create a restraining torque, T_e:

[B.1] $$T_e = P_e\left(\bar{y} - h_s/2\right)$$

where $\bar{y}$ is the distance from the top of the deck slab to the floorbeam centroid and h_s is the thickness of the deck slab. If the rotation, θ, is small, the centroid deflection, Δ_e, caused by the restraint, P_e, is computed as:

[B.2] $$\Delta_e \approx \theta\left(\bar{y} - h_s/2\right)$$

Using the beam deflection equation for a fixed beam with an applied point load a distance, *a*, from the support, the deflection is also computed as:

[B.3] $$\Delta_e = \frac{P_e a^3 (s-a)^3}{3EI_y s^3}$$

where E is the modulus of elasticity and I_y is the y-axis moment of inertia of the floorbeam. Setting Eq. [B.2] equal to Eq. [B.3] and rearranging for the rotation, θ:

[B.4] $$\theta \approx \frac{P_e a^3 (s-a)^3}{3EI_y s^3 (\bar{y} - h_s/2)}$$

Rearranging Eq. [B.1] for the restraint, P_e, and substituting it into Eq. [B.4]:

[B.5] $$\theta \approx \frac{T_e a^3 (s-a)^3}{3EI_y s^3 (\bar{y} - h_s/2)^2}$$

Rearranging Eq. [B.5] yields the rotational restraint, K_e, provided by the vertical eccentricity of the rigid deck slab from the floorbeam centroid:

[3.3] $$K_e = \frac{T_e}{\theta} = \frac{3EI_y s^3 (\bar{y} - h_s/2)^2}{a^3 (s-a)^3}$$

The total applied torque is equilibrated by the sum of the internal torque, T, and the restraining torque, T_e. The total rotational restraint, K_θ, is therefore the sum of the restraint provided by the torsional stiffness of the floorbeams, Eq. [3.2], and that provided by the vertical eccentricity deck, Eq. [3.3]:

[3.4] $$K_\theta \approx \frac{GJs}{a(s-a)} + \frac{3EI_y s^3 \left(\bar{y} - h_s/2\right)^2}{a^3 \left(s-a\right)^3}$$

B.2 EQUATIONS [3.5] AND [3.6]

Equations [3.5] and [3.6] provide the rotational restraint at the quarter-spans and midspan, respectively, of a floorbeam with fixed ends and a uniform torque applied between the quarter points. The rotational restraint provided by the torsional stiffness of a floorbeam subjected to a uniform torque applied between the quarter points can be computed at a distance, a, from the support:

[B.6] $$k_\theta = \frac{t}{\theta} = \frac{2GJ}{sa - a^2 - s^2/16}$$

where $0.25s \leq a \leq 0.75s$. If the restraint, p_e, provided by the deck slab is assumed uniform, the deflection at a can be computed using the beam deflection equation for a fixed beam with a uniformly distributed load between the quarter points:

[B.7] $$\Delta_e = p_e \times \frac{(a - s/4)^4 - sa^3 + (11/16)s^2a^2}{24EI_y}$$

for $0.25s \le a \le 0.75s$. Substituting Eq. [B.7] into Eq. [B.2] and rearranging:

[B.8] $$\theta \approx p_e \times \frac{(a - s/4)^4 - sa^3 + (11/16)s^2a^2}{24EI_y(\bar{y} - h_s/2)}$$

The uniform restraint, p_e, causes a uniform restraining torque, t_e:

[B.9] $$t_e = p_e(\bar{y} - h_s/2)$$

Arranging Eq. [B.9] for the restraint, p_e, and substituting it into Eq. [B.8]:

[B.10a] $$\theta \approx t_e \times \frac{(a - s/4)^4 - sa^3 + (11/16)s^2a^2}{24EI_y(\bar{y} - h_s/2)^2}$$

Rearranging Eq. [B.10a], the rotational restraint, k_e, provided by the eccentricity of the deck slab is:

[B.10b] $$k_e = \frac{t_e}{\theta} \approx \frac{24EI_y(\bar{y} - h_s/2)^2}{(a - s/4)^4 - sa^3 + (11/16)s^2a^2}$$

The total rotational restraint, k_θ, is therefore the sum of the restraint provided by the torsional stiffness of the floorbeams, Eq. [B.6], and that provided by the eccentric deck, Eq. [B.10b]:

[B.11] $$k_\theta = \frac{t_a}{\theta} \approx \frac{2GJ}{sa - a^2 - s^2/16} + \frac{24EI_y\left(\bar{y} - h_s/2\right)^2}{\left(a - s/4\right)^4 - sa^3 + \left(11/16\right)s^2a^2}$$

where $0.25s \le a \le 0.75s$. Solving Eq. [B.11] for $a = s/4$, the rotational restraint at the quarter-spans of a floorbeam is:

[3.5] $$k_\theta = \frac{t_a}{\theta} \approx \frac{16GJ}{s^2} + \frac{6144EI_y\left(\bar{y} - h_s/2\right)^2}{7s^4}$$

Similarly, solving Eq. [B.11] for $a = s/2$, the rotational restraint at the midspan of a floorbeam is:

[3.6] $$k_\theta = \frac{t_a}{\theta} \approx \frac{32GJ}{3s^2} + \frac{6144EI_y\left(\bar{y} - h_s/2\right)^2}{13s^4}$$

B.3 EQUATIONS [3.7] AND [3.8]

Equations [3.5] and [3.6] were derived assuming the floorbeams are fixed against y-axis deflection, but steel floorbeams are likely to behave as pinned. The beam deflection equation, Eq. [B.7], used in Section B.2 needs to be revised for a beam with pinned ends and then the process outlined in Section B.2 can be used to develop equations for the rotational restraint, k_θ, at the quarter-spans and midspan of steel floorbeams.

Using the moment-area theorem, the deflection at the quarter-span of a fixed beam with a uniformly distributed load between the quarter points can be computed as:

[B.12] $$\Delta_e = \frac{5 p_e s^4}{768 E I_y}$$

Following the process outline in Section B.2, the rotational restraint at the quarter-span of a steel floorbeam is:

[3.7] $$k_\theta = \frac{t_a}{\theta} \approx \frac{16GJ}{s^2} + \frac{768 E I_y \left(\bar{y} - h_s/2\right)^2}{5 s^4}$$

Using the moment-area theorem again, the deflection at midspan of a fixed beam with a uniformly distributed load between the quarter points is:

[B.13] $$\Delta_e = \frac{57 p_e s^4}{6144 E I_y}$$

Following the process outlined in Section B.2, the rotational restraint at the midspan of a steel floorbeam is:

[3.8] $$k_\theta = \frac{t_a}{\theta} \approx \frac{32GJ}{3s^2} + \frac{6144 E I_y \left(\bar{y} - h_s/2\right)^2}{57 s^4}$$

APPENDIX C: SOURCE CODE FOR *CSDECK*

The overall function, *CSDECK*, contains all raw input data and controls the entire analysis. *CSDECK* contains three input functions, *SECTION*, *STEEL*, and *UNITM*, to organize the input data into a format easily manipulated by MATLAB. Once the input data has been arranged, *CSDECK* begins the analysis by sequentially calling the main functions, *MOMCURV* and *PDELTA*, which in turn call the sub-functions and basic functions as outlined in Section 4.6. This Appendix contains the source code for *CSDECK* and all of the functions within it, including a brief description of the input parameters and any calculations performed.

As mentioned in Chapter 4, the program *QULT* by Salonga (2010) was used as a model to develop to source code for computing the moment-curvature relationship. Four of the functions within *CSDECK*, *MOMCURV*, *CONTOURCURV*, *INTERACTION* (originally *NMBOUND*), and *INTERPOLATE*, were developed by Salonga (2010) and have been adopted into *CSDECK* with only minor modifications.

C.1 INPUT FUNCTIONS

Input functions are functions that organize the parameters input directly into *CSDECK* into a format that is easily manipulated by MATLAB. For example, the function *SECTION* takes the dimensions of the deck slab and the number of layers used to discretize the slab as inputs and outputs a single matrix containing the area and distance from the top fibre to the center of each layer.

C.1.1 *SECTION*

```
function [conc_layers]=SECTION(hs, w, n)
%%  1. Input Parameters:
%       hs: slab thickness (mm)
%       w: slab width (mm)
%       n: number of layers to discretize the cross section

%%  2. Create an nx2 matrix containing the concrete layer properties.
%       Each row represents one layer:
%       1st column - area (mm^2)
%       2nd column - distance from the top fibre to the centroid (mm)
conc_layers = zeros(n,2);
for ii = 1:n
    conc_layers(ii,1) = hs/n*w; % layer area
    conc_layers(ii,2) = (ii-0.5)*hs/n; % distance to center of layer
end
end
```

C.1.2 *STEEL*

```
function [steel_prop] = STEEL(conc_prop,fy,Es,steel_comp)
%%  1. Input Parameters:
%       conc_prop: matrix containing the stress-strain relationship
%                  for concrete in compression (MPa)
%       fy: yield stress of steel (MPa)
%       Es: modulus of elasticity of steel (MPa)
%       steel_comp: 1 to consider the steel in compression
%                   0 to treat steel in compression as concrete

%%  2. Create matrix containing stress-strain relationship for steel.
%       Each row represents one stress/strain point:
%       1st column - strain
%       2nd column - stress (MPa)
%       Notes: A bilinear relationship is used in tension, and either
%       the same bilinear relationship (steel_comp=1) or the concrete
%       relationship(steel_comp=0) is used in compression.
if steel_comp == 1
    steel_prop = [-1,-fy;-fy/Es,-fy;fy/Es,fy;1,fy];
else if steel_comp ==0
        steel_prop = zeros(size(conc_prop,1)+2,2);
    for i=1:size(conc_prop,1)
        steel_prop(i,1) = conc_prop(i,1);
        steel_prop(i,2) = conc_prop(i,2);
    end
    steel_prop(size(conc_prop,1)+1,1) = fy/Es;
    steel_prop(size(conc_prop,1)+1,2) = fy;
    steel_prop(size(conc_prop,1)+2,1) = 1;
    steel_prop(size(conc_prop,1)+2,2) = fy;
    else
        disp('Must Input 1 or 0 for steel in compression');
    end
end
end
```

C.1.3 *UNITM*

```
function BMD_unit = UNITM(location,moment,n_elem,L)
%%  1. Input Parameters:
%       location: row vector containing points along interior span (mm)
%       moment: row vector containing the primary moment at each
%               location along the interior span (N.mm)
%       n_elem: number of segments of constant curvature along the
%               interior span
%       L: length of the three spans (mm)

%%  2. Create a matrix containing the unit primary moment diagram.
%       Each row represents one node along the interior span:
%       1st column: location of the nodes (mm)
%       2nd column: moment at each node for the unit moment diagram
%                   (N.mm)
location = roundn(location,-6);
if location(1,1)~=0 % check inputs
    disp('First location must be x=0');
elseif location(size(location,1),1)~= roundn(L,-6); % check inputs
    disp('Last location must be x=L');
else
    M_input_max = max(abs(moment));
    elem_length = L/n_elem;
    BMD_unit = zeros(n_elem+1,2);
    for i = 0:n_elem
        BMD_unit(i+1,1) = roundn(i*elem_length,-6);
        BMD_unit(i+1,2) = INTERPOLATE(location, moment,
BMD_unit(i+1,1))/M_input_max;
    end
end
end
```

C.2 BASIC FUNCTIONS

Basic functions perform simple calculations that must be repeated several times. Some of these functions, such as *INTERACTION* and *CENTROID*, are called only twice in an analysis, while others, such as *INTERPOLATE*, *STRESS*, and *EQUILIBRIUM*, are called thousands of times per analysis.

C.2.1 *INTERPOLATE* (modified from Salonga, 2010)

```
function [y] = INTERPOLATE(xvector,yvector,x)
%%  1. Input Parameters:
%       xvector: column vector containing x values in ascending order
%       yvector: column vector containing y values
%       x: value of x used to interpolate for the desired y
```

```
%%  2. Find the two x values that bound x.
%       Check that x is within the range of xvector:
%       If not, set y = 0.
maxima = max(xvector);
minima = min(xvector);
if x > maxima(1,1)
    y = 0;
elseif x < minima(1,1)
        y = 0;
elseif x == xvector(find(xvector(:,1)==x,1,'first'),1)
            y = yvector(find(xvector(:,1)==x,1,'first'));
else
    previous_index = find(xvector(:,1)>x,1,'first')-1;
    next_index = find(xvector(:,1)>x,1,'first');
    x1 = xvector(previous_index,1);
    x2 = xvector(next_index,1);
%%  3. Find the corresponding two y values that must bound y.
    y1 = yvector(previous_index,1);
    y2 = yvector(next_index,1);

%%  4. Linearly interpolate between the two y values to estimate the y
%   value corresponding to x.
    slope = (y2-y1)/(x2-x1);
    intercept = y2 - (slope*x2);
    y = (x*slope) + intercept;
end
end
```

C.2.2 *STRESS*

```
function [stress] = STRESS(strain,mat_prop)
%%  1. Input Parameters:
%       strain: value of strain
%       mat_prop: matrix containing the stress-strain relationship
%       (MPa)

%%  2. Call INTERPOLATE to find the stress value corresponding to the
%   input strain
if strain > mat_prop(size(mat_prop,1),1)
        stress = 0;
else
    stress = INTERPOLATE(mat_prop(:,1),mat_prop(:,2),strain);
end
end
```

C.2.3 *CENTROID*

```
function plas_cent = CENTROID(conc_lay,steel_lay,conc_prop,steel_prop)
%%  1. Input Parameters:
%       conc_lay: matrix containing the area and location of each
%                 concrete layer (mm^2,mm)
%       steel_lay: matrix containing the area and centroid of each
%                  steel layer (mm^2,mm)
```

```
%       conc_prop: matrix containing the stress-strain relationship
%                  for concrete in compression (MPa)
%       steel_prop: matrix containing the stress-strain relationship
%                   for steel (MPa)

%%  2. Find the strain corresponding to the peak concrete stress
peakstress = min(conc_prop(:,2));
strain = INTERPOLATE(conc_prop(:,2),conc_prop(:,1),peakstress);

%%  3. Compute forces and moments (from top fibre) from each steel and
%   concrete layer, assuming the peak strain is applied uniformly along
%   the section.
steel_force = zeros(size(steel_lay,1),2);
for i = 1:size(steel_lay,1)
    steel_force(i,1) = (STRESS(strain,steel_prop)-
STRESS(strain,conc_prop))*steel_lay(i,1);
    steel_force(i,2) = steel_force(i,1)*steel_lay(i,2);
end
conc_force = zeros(size(conc_lay,1),2);
for ii = 1:size(conc_lay,1)
    conc_force(ii,1) = STRESS(strain,conc_prop)*conc_lay(ii,1);
    conc_force(ii,2) = conc_force(ii,1)*conc_lay(ii,2);
end

%%  4. Compute the distance from the plastic centroid to the top fibre
totalforce = sum(steel_force(:,1))+sum(conc_force(:,1));
totalmoment = sum(steel_force(:,2))+sum(conc_force(:,2));
plas_cent = totalmoment/totalforce;
end
```

C.2.4 *EQUILIBRIUM*

```
function [load_moment] =
EQUILIBRIUM(conc_lay,steel_lay,conc_prop,steel_prop,plas_cent,curv,top_s
train)
%%  1. Input Parameters:
%       conc_lay: matrix containing the area and centroid of each
%                 concrete layer (mm^2,mm)
%       steel_lay: matrix containing the area and centroid of each
%                  steel layer (mm^2,mm)
%       conc_prop: matrix containing the stress-strain relationship of
%                  concrete in compression (MPa)
%       steel_prop: matrix containing the stress-strain relationship of
%                  steel (MPa)
%       plas_cent: distance from the plastic centroid to the top fibre
%                  (mm)
%       curv: value of curvature (rad/mm)
%       top_strain: extreme compression fibre strain

%%  2. Compute the neutral axis depth.
c = -top_strain/curv;

%%  3. Find the forces and moments (from plastic centroid) for each
%   steel and concrete layer
steel_force = zeros(size(steel_lay,1),2);
```

```
for i = 1:size(steel_lay,1)
    strain = top_strain*(1-steel_lay(i,2)/c);
    if strain < 0 % if steel is in compression
    steel_force(i,1) = (STRESS(strain,steel_prop)-
STRESS(strain,conc_prop))*steel_lay(i,1);
    steel_force(i,2) = steel_force(i,1)*(steel_lay(i,2)-plas_cent);
    else % if steel is in tension
    steel_force(i,1) = (STRESS(strain,steel_prop))*steel_lay(i,1);
    steel_force(i,2) = steel_force(i,1)*(steel_lay(i,2)-plas_cent);
    end
end
conc_force = zeros(size(conc_lay,1),2);
for ii = 1:size(conc_lay,1)
    strain = top_strain*(1-conc_lay(ii,2)/c);
    conc_force(ii,1) = STRESS(strain,conc_prop)*conc_lay(ii,1);
    conc_force(ii,2) = conc_force(ii,1)*(conc_lay(ii,2)-plas_cent);
end

%%  4. Compute the axial load and bending moment using fundamentals of
%   equilibrium.
%       load_moment = [load, moment]
load_moment = [-(sum(steel_force(:,1))+sum(conc_force(:,1))),
(sum(steel_force(:,2))+sum(conc_force(:,2)))];
end
```

C.2.5 *AVGSTIFF*

```
function avg_EI = AVGSTIFF(Mcurv,BMD)
%%  1. Input Parameters:
%       Mcurv: matrix containing the moment-curvature relationship of
%              the cross section(N.mm, rad/mm)
%       BMD: matrix containing the bending moment diagram (mm,N.mm)
avg_M = zeros(size(BMD,1)-1,1);
avg_phi = avg_M;
avg_EI = avg_M;

%%  2. Compute the gross rigidities of the cross section.
count = 1;
while Mcurv(count,1)<0
    count = count+1;
end
EI_gross_pos = Mcurv(count,1) / Mcurv(count,2);
EI_gross_neg = Mcurv(count-1,1) / Mcurv(count-1,2);

%%  3. Compute the average secant rigidity of each segment in the
%   interior span.
%       If the moment, either positive or negative, exceeds the
%       cross-section capacity, set the rigidity equal to the rigidity
%       at the cross-section capacity.
for i = 1:size(BMD,1)-1
    if (BMD(i,2)+BMD(i+1,2))/2 >= Mcurv(size(Mcurv,1),1)
        avg_EI(i,1) = (Mcurv(size(Mcurv,1),1)/Mcurv(size(Mcurv,1),2));
    elseif (BMD(i,2)+BMD(i+1,2))/2 <= Mcurv(1,1)
        avg_EI(i,1) = (Mcurv(1,1)/Mcurv(1,2));
```

```
    elseif (BMD(i,2)+BMD(i+1,2))/2 < Mcurv(count,1) &&
(BMD(i,2)+BMD(i+1,2))/2 >=0
        avg_EI(i,1) = EI_gross_pos;
    elseif (BMD(i,2)+BMD(i+1,2))/2 > Mcurv(count-1,1) &&
(BMD(i,2)+BMD(i+1,2))/2 < 0
        avg_EI(i,1) = EI_gross_neg;
    else
        Moment = (BMD(i,2)+BMD(i+1,2))/2;
        avg_phi(i,1) = INTERPOLATE(Mcurv(:,1),Mcurv(:,2),Moment);
        avg_EI(i,1) = Moment/avg_phi(i,1);
    end
end
end
```

C.2.6 *INTERACTION* (modified from Salonga, 2010)

```
function int_diag =
INTERACTION(conc_lay,steel_lay,conc_prop,steel_prop,plas_cent)
%  1. Input Parameters:
%       conc_lay: matrix containing the area and centroid of each
%                 concrete layer (mm^2,mm)
%       steel_lay: matrix containing the area and centroid of each
%                  steel layer (mm^2,mm)
%       conc_prop: matrix containing the stress-strain relationship of
%                  concrete in compression (MPa)
%       steel_prop: matrix containing the stress-strain relationship of
%                  steel (MPa)
%       plas_cent: distance from the plastic centroid to the top fibre
%                  (mm)

%% 2. Find the ultimate extreme fibre compression strain
ult_strain = conc_prop(1,1); %largest input strain value

%% 3. Compute the approximate ultimate interaction diagram
%       Find the load and moment corresponding to curvatures defined
%       by equating the top strain to the ultimate strain and the
%       neutral axis depth to the depth centroid for each concrete
%       layer.
int_diag = zeros(size(conc_lay,1),3);
for i = 1:size(conc_lay,1) % for each concrete layer:
    this_curv = -ult_strain/conc_lay(i,2);
    load_moment =
EQUILIBRIUM(conc_lay,steel_lay,conc_prop,steel_prop,plas_cent,this_curv,
ult_strain);
    int_diag(i,1) = this_curv; % ultimate curvature
    int_diag(i,2) = load_moment(1,1); % ultimate axial load
    int_diag(i,3) = load_moment(1,2); % ultimate bending moment
end
end
```

C.2.7 *ENDROTN*

```
function end_rotns = ENDROTN(avg_EI,BMD)
%% 1.  Input Parameters:
%       avg_EI: column vector containing the average rigidity of each
```

```
%               segment (N.mm^2)
%       BMD: matrix containing the bending moment diagram (mm,N.mm)

%% 2.  Compute the average curvature of each segment
L = BMD(size(BMD,1),1);
elem_length = L / (size(BMD,1)-1);
avg_phi = zeros(size(avg_EI,1),2);
for i = 1:size(avg_EI,1)
    avg_phi(i,1) = (i-0.5)*elem_length;
    avg_phi(i,2) = ((BMD(i,2)+BMD(i+1,2))/2)/avg_EI(i,1);
end

%% 3. Compute the end rotations using the Moment Area Theorem
%   (e.g. Hibbeler, 2009)
%       The deflection at the near support with respect to a tangent
%       at the far support is equal to the area under the curvature
%       diagram multiplied by the distance from the near support to
%       the centroid of the area under the curvature diagram. The
%       curvature along each segment is assumed to be constant.
area_moment_LR = zeros(size(avg_EI,1),1);
area_moment_RL = zeros(size(avg_EI,1),1);
for ii = 1 : size(avg_EI,1)
    area_moment_LR(ii,1) = -avg_phi(ii,1)*avg_phi(ii,2)*elem_length;
    area_moment_RL(ii,1) = (L-avg_phi(ii,1))*avg_phi(ii,2)*elem_length;
end
delta_LR = sum(area_moment_LR);
delta_RL = sum(area_moment_RL);
%       Assuming small rotations, the rotation at the near support is
%       equal to the deflection at the far support with respect to a
%       tangent at the near support, divided by the span length.
left_rotn = delta_RL / L;
right_rotn = delta_LR / L;
end_rotns = [left_rotn, right_rotn];
end
```

C.3 SUB-FUNCTIONS

Sub-functions perform most of the detailed calculations that are carried out within the overall program, *CSDECK*. The function *CONTOURCURV* gets called only twice in a given analysis, while the functions *ENDMOM* and *DEFLECTION* can be called hundreds of times during an analysis.

C.3.1 *CONTOURCURV* (modified from Salonga, 2010)

```
function [contour] =
CONTOURCURV(conc_lay,steel_lay,conc_prop,steel_prop,plas_cent,N)
%%  1. Input Parameters:
```

```
%       conc_lay: matrix containing the area and centroid of each
%                 concrete layer (mm^2,mm)
%       steel_lay: matrix containing the area and centroid of each
%                  steel layer (mm^2,mm)
%       conc_prop: matrix containing the stress-strain relationship of
%                  concrete in compression (MPa)
%       steel_prop: matrix containing the stress-strain relationship of
%                  steel (MPa)
%       plas_cent: distance from the plastic centroid to the top fibre
%                  (mm)
%       N: axial load (N)

%% 2. Compute an approximate interaction diagram
NMcurv = INTERACTION(conc_lay,steel_lay,conc_prop,steel_prop,plas_cent);

%% 3. Estimate the maximum curvature for the given axial load
%       If the axial load exceed the maximum from the approx.
%       interaction diagram, set the max. curvature equal to the
%       curvature at the max. load. Otherwise, estimate the curvature
%       for the given axial load from the approx. interaction diagram.
N_max = max(NMcurv(:,2));
if N > N_max
    phi_max = INTERPOLATE(NMcurv(:,2),NMcurv(:,1),N_max);
else
    phi_max = INTERPOLATE(NMcurv(:,2),NMcurv(:,1),N);
end

%% 4. Determine the curvature contours to compute
n = 30;   % number of contours
%       Estimate the maximum curvature at the balanced failure load:
M_bal = max(NMcurv(:,3));
phi_bal = INTERPOLATE(NMcurv(:,3),NMcurv(:,1),M_bal);
curv = zeros(n,1);
%       If the maximum curvature exceeds that at the balanced failure
%       load, ensure that at least 2/3 of the contours are below the
%       curvature at the balanced failure load.
if phi_max > 2*phi_bal
    interval1 = (phi_bal)/round(2/3*n);
    interval2 = (phi_max - phi_bal)/round(1/3*n);
    for i=1:round(2/3*n);
        curv(i,1) = i*interval1;
    end
    for i=1+round(2/3*n):n
        curv(i,1) = phi_bal + ((i-round(2/3*n))*interval2);
    end
else
    interval3 = phi_max/n;
    for i=1:n
        curv(i,1) = i*interval3;
    end
end

%% 5. Compute the axial load and moment for several points per contour
%       Each point on a contour is defined by a different extreme
%       compression fibre strain, ranging from 0 to the ultimate value.
m = 70; % Number of points per contour
```

```
neg_strain = conc_prop(1,1); % ultimate compression fibre strain
increment = neg_strain/m; % strain increment
contour = zeros(m,3,size(curv,1));
for k=1:size(curv,1)
    for i=1:m
        thisQM =
EQUILIBRIUM(conc_lay,steel_lay,conc_prop,steel_prop,plas_cent,curv(k,1),
increment*i);
        contour(i,3,k) = curv(k,1);
%       Set negative axial loads or bending moments equal to zero
        if thisQM(1,1) <= 0
            contour(i,1,k) = 0;
            contour(i,2,k) = 0;
        elseif thisQM(1,2)<0
            contour(i,1,k) = 0;
            contour(i,2,k) = 0;
        else
        contour(i,1,k) = thisQM(1,1);
        contour(i,2,k) = thisQM(1,2);
        end
    end
end
end
```

C.3.2 *ENDMOM*

This function computes the end moments developed due to loads applied to the interior span, using the Force Method of analysis (e.g. Hibbeler, 2009) as discussed in Chapter 4. As mentioned, the solution does not always converge if the process discussed in Chapter 4 is followed, so an algorithm was written to improve convergence. As shown in Figure 4.4, the primary moment diagram for the simply supported primary structure is used initially and is shifted to satisfy the boundary conditions at the interior supports. However, shifting the moment diagram changes the rigidity along the length of the member, so an iterative procedure must be adopted to find the correct rigidity distribution and updated moment diagram that yield compatible rotations at the interior supports. This process can be shortened by recognizing that any two subsequent iterations must bound the correct solution. For example, Line A in Figure C.1 represents the primary bending moment diagram used in the first iteration and the updated moment diagram that is

produced is shown by Line B. Line A has zero end moments, so the midspan moment is larger than the actual midspan moment and the midspan rigidity is less than the actual midspan rigidity. Since the midspan rigidity in Line A is underestimated, the resulting magnitude of the end moments in Line B is overestimated and the midspan moment underestimated. Therefore, Lines A and B must bound the correct solution. Since positive moments are shown on the tension face, Line A becomes the upper bound and Line B the lower bound. If Line B is used to compute the rigidity distribution for the subsequent iteration, the midspan rigidity will be overestimated and so the resulting updated moment diagram will underestimate the magnitude of the end moments and overestimate the midspan moments. However, if the average of the upper and lower bounds, Line C, is used to compute the rigidity in the following iteration a more accurate estimate of the actual moments will be obtained, as shown by Line D. Now, Lines C and D must bound the correct solution and so they should be compared to the previous upper and lower bounds, Lines A and B respectively, to determine the updated bounds. The average of the previous bounds, Line C, will always be one of the updated bounds, since the midspan moment is less than the previous upper-bound value and higher than the previous lower-bound value. Since the midspan moment in Line C is larger than in Line D, Line C becomes the revised upper bound. Since the midspan moment in Line D is larger than in Line B, Line D is the new lower bound. If the midspan moment in Line B was larger than in Line D, Line B would remain the lower bound. The average of the new bounds, Lines C and D, is then used to determine the rigidity for the following iteration and both the average and the resulting moment diagram are compared to Lines C and D to determine the new bounds. If this process is continued the solution converges consistently.

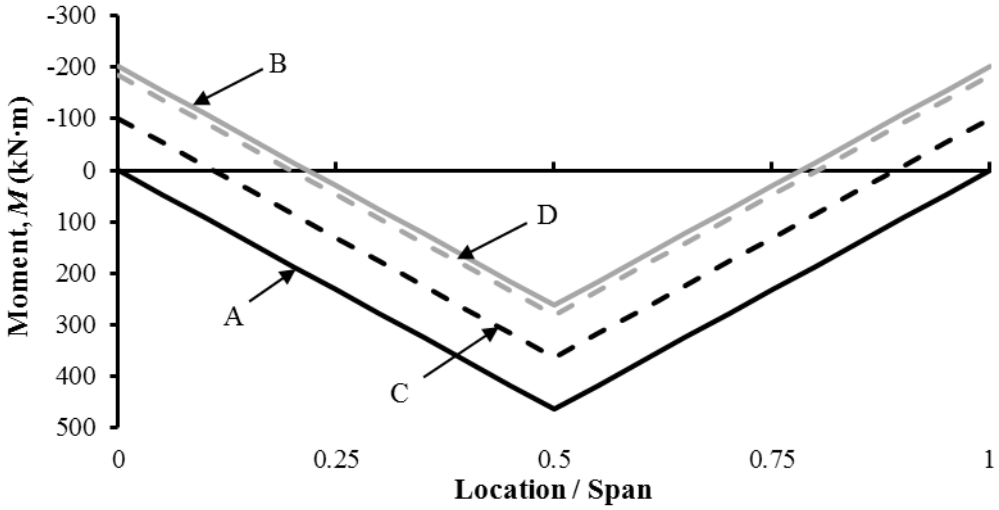

Figure C.1: Iterations of distributing moments in the interior span.

```
function RBMD = ENDMOM(Mcurv,PBMD,elas_prop)
%% 1. Input Parameters
%       Mcurv: matrix containing the moment-curvature relationship of
%              the cross section (N.mm, rad/mm)
%       PBMD: bending moment diagram for the primary, simply
%             supported, interior span (mm, N.mm)
%       elas_prop: column vector containing stiffness properties
%            [3*gamma_L*E*I/L; 3*gamma_R*E*I/L; K_theta; plas_hinge];
L = PBMD(size(PBMD,1),1);
elem_length = L / (size(PBMD,1)-1);
RBMD = PBMD;
redundant_left= UNITM([0;L],[1;0],(size(PBMD,1)-1),L);
redundant_right= UNITM([0;L],[0;1],(size(PBMD,1)-1),L);
error = PBMD(:,2);

%% 1. Determine the initial upper- and lower-bound moment diagrams
UBOUND = PBMD;
LBOUND = PBMD;
LBOUND(:,2) = PBMD(:,2) - max(PBMD(:,2));

%% 2. Iterate for the actual moment distribution
while max(abs(error))/max(RBMD(:,2))>0.0001 %set for tolerance
    avg_stiff = AVGSTIFF(Mcurv, RBMD);
%       Compute the rotations at the ends of the interior primary span
%       due to unit moments applied at either support:
    redundant_end_rotns_left = ENDROTN(avg_stiff,redundant_left);
    redundant_end_rotns_right = ENDROTN(avg_stiff,redundant_right);
%       Compute the flexibility coefficients:
    alpha_LL =
redundant_end_rotns_left(1)+1/(elas_prop(1,1)+elas_prop(3,1));
    alpha_LR = redundant_end_rotns_right(1);
    alpha_RL = -redundant_end_rotns_left(2);
    alpha_RR = -
redundant_end_rotns_right(2)+1/(elas_prop(2,1)+elas_prop(3,1));
%       Compute the primary end rotations:
```

```
    primary_end_rotns = ENDROTN(avg_stiff,PBMD);
%       Compute the end moments, unless the member is simply supported:
    if elas_prop(1:3,1)==0
        left_support_mom = 0;
        right_support_mom = 0;
    else
        left_support_mom = (primary_end_rotns(1)*(alpha_RR/alpha_LR)-(-
primary_end_rotns(2)))/(alpha_RL - alpha_LL*alpha_RR/alpha_LR);
        right_support_mom = (-primary_end_rotns(1)-
left_support_mom*alpha_LL)/alpha_LR;
    end
    RBMD_prev = RBMD;
%       Revise the BMD for the computed end moments:
    for i = 1:size(RBMD,1)
        RBMD(i,2) = round(PBMD(i,2) + left_support_mom +
(right_support_mom - left_support_mom)*(i-1)*elem_length / L);
    end
%       Compute the difference between this BMD and the previous BMD:
    error = RBMD(:,2) - RBMD_prev(:,2);
%       Compare the previous BMD, computed by averaging the previous
%       bounds, and the  updated BMD to the previous upper and lower
%       bounds.
    if max(RBMD_prev(:,2)) > max(RBMD(:,2))
            UBOUND(:,2) = RBMD_prev(:,2);
        if max(RBMD(:,2)) > max(LBOUND(:,2))
            LBOUND(:,2) = RBMD(:,2);
        end
    else
            LBOUND(:,2) = RBMD_prev(:,2);
        if max(RBMD(:,2)) < max(UBOUND(:,2))
            UBOUND(:,2) = RBMD(:,2);
        end
    end

%       Final convergence check:
    if abs((max(UBOUND(:,2))-
max(LBOUND(:,2)))/(max(LBOUND(:,2))))<0.0000001 &&
max(abs(error))/max(RBMD(:,2))>0.001
        disp('Convergence problems, watch results. Check for upwards
deflections.');
        if max(RBMD(:,2)) > max(RBMD_prev(:,2))
            UBOUND(:,2) = RBMD(:,2);
        else
            LBOUND(:,2) = RBMD(:,2);
        end
    end

%       Average the new upper and lower bounds to obtain the moment
%       diagram, used to determine the rigidity in the following
%       iteration:
    RBMD(:,2) = (LBOUND(:,2) + UBOUND(:,2))/2;
end

%% 3. Check the results
%       Check for plastic redistribution:
if left_support_mom < Mcurv(1,1);
```

```
    if elas_prop(4,1)== 1
       left_support_mom = Mcurv(1,1);
    else
       RBMD(:,2) = zeros(size(RBMD,1),1);
    end
end
if right_support_mom < Mcurv(1,1);
    if elas_prop(4,1)== 1
       right_support_mom = Mcurv(1,1);
    else
       RBMD(:,2) = zeros(size(RBMD,1),1);
    end
end
%       Recalculate the updated moment diagram if plastic
%       redistribution did occur.
if max(RBMD(:,2))==0
else
for i = 1:size(RBMD,1)
RBMD(i,2) = round(PBMD(i,2) + left_support_mom + (right_support_mom -
left_support_mom)*(RBMD(i,1)/L));
end
end
%       If the revised moment exceeds the cross-section capacity, the
%       deck failed.
if max(RBMD(:,2)) > Mcurv(size(Mcurv,1),1)
    RBMD(:,2) = zeros(size(RBMD,1),1);
end
end
```

C.3.3 *DEFLECTION*

```
function [delta] = DEFLECTION(avg_EI,RBMD)
%% 1. Input Parameters
%       avg_EI: column vector containing the average rigidity of each
%               segment (N.mm^2)
%       RBMD: matrix containing the updated moment diagram, accounting
%             for any ends moments (mm, N.mm)

%% 2. Compute the average curvature in each segment
avg_phi = zeros(size(avg_EI,1),2);
for i = 1:size(avg_EI,1)
    avg_phi(i,1) = (RBMD(i,1)+RBMD(i+1,1))/2;
    avg_phi(i,2) = ((RBMD(i,2)+RBMD(i+1,2))/2)/avg_EI(i,1);
end

%% 3. Compute the end rotations
end_rotns = ENDROTN(avg_EI,RBMD);

%% 4. Compute the rotation and displacement at each interior span node
L = RBMD(size(RBMD,1),1);
elem_length = L / (size(RBMD,1)-1);
node_rotns = zeros(size(RBMD, 1),1);
delta = zeros(size(RBMD,1),1);
node_rotns(1,1) = end_rotns(1);
for ii = 2:size(RBMD,1)
```

```
    node_rotns(ii,1) = node_rotns(ii-1,1) - avg_phi(ii-1,2)*elem_length;
    delta(ii,1) = roundn(delta(ii-1,1) + node_rotns(ii-1,1)*elem_length
- avg_phi(ii-1,2)*(elem_length^2)/2, -3);
%       round values to avoid non-zero deflections at the far end.
end

%% 5. Check results:
if abs((node_rotns(size(node_rotns,1),1) - end_rotns(2))/end_rotns(2)) >
0.01
    disp('Rotation at the right support is not equal the previously
computed value');
end
if abs(delta(size(delta,1),1)/max(delta(:,1))) > 0.0001
    disp('Deflection at the right support is not equal zero');
end
```

C.4 MAIN FUNCTIONS

The main functions organize the analysis and control when the sub-functions are called to perform detailed calculations. The function *CSDECK* is the overall function that runs the entire analysis. All of the input data is entered directly into the function *CSDECK*, which calls *MOMCURV* to compute the moment-curvature relationship of the cross section and *PDELTA* to compute the total moments, including second-order effects, along the interior span.

C.4.1 *MOMCURV* (modified from Salonga, 2010)

```
function [Mcurv] =
MOMCURV(conc_lay,steel_lay,conc_prop,steel_prop,plas_cent,N)
%  1. Input Parameters:
%       conc_lay: matrix containing the area and centroid of each
%                 concrete layer (mm^2,mm)
%       steel_lay: matrix containing the area and centroid of each
%                  steel layer (mm^2,mm)
%       conc_prop: matrix containing the stress-strain relationship of
%                  concrete in compression (MPa)
%       steel_prop: matrix containing the stress-strain relationship of
%                  steel (MPa)
%       plas_cent: distance from the plastic centroid to the top fibre
%                  (mm)
%       N: axial load (N)

%% 2. Compute contours of equal curvature for positive moments
```

```
contour_pos =
CONTOURCURV(conc_lay,steel_lay,conc_prop,steel_prop,plas_cent,N);

%% 3. Compute contours of equal curvature for negative moments
slab_thick = max(conc_lay(:,2))+0.5*(conc_lay(2,2)-conc_lay(1,2));
neg_plas_cent = slab_thick - plas_cent;
neg_conc_lay = zeros(size(conc_lay,1),2);
for i = 1:size(conc_lay,1)
    neg_conc_lay(i,1) = conc_lay(size(conc_lay,1)+1-i,1);
    neg_conc_lay(i,2) = slab_thick - conc_lay(size(conc_lay,1)+1-i,2);
end
neg_steel_lay = zeros(size(steel_lay,1),2);
for ii = 1:size(steel_lay,1)
    neg_steel_lay(ii,1) = steel_lay(size(steel_lay,1)+1-ii,1);
    neg_steel_lay(ii,2) = slab_thick - steel_lay(size(steel_lay,1)+1-
ii,2);
end
contour_neg =
CONTOURCURV(neg_conc_lay,neg_steel_lay,conc_prop,steel_prop,neg_plas_cen
t,N);

%% 3. Interpolate to determine the bending moment corresponding to the
%  applied axial load for each positive curvature contour
M_curv_pos = zeros(size(contour_pos,3),2);
%       Remove any of the values in the curvature contours that are
%       zero:
for k=1:size(contour_pos,3)
    contour_pos_index = find(contour_pos(:,1,k));
    contour_pos_cut = zeros(size(contour_pos_index));
    for iii = 1:size(contour_pos_index)
        contour_pos_cut(iii,1) =
contour_pos(contour_pos_index(iii,1),1,k);
        contour_pos_cut(iii,2) =
contour_pos(contour_pos_index(iii,1),2,k);
    end
%       Interpolate to find the moment for each contour:
    M_curv_pos(k,2) = contour_pos(1,3,k);
    if size(contour_pos_cut,1)>1
        M_curv_pos(k,1) =
INTERPOLATE(contour_pos_cut(:,1),contour_pos_cut(:,2),N);
    elseif contour_pos_cut(1,1) == N
        M_curv_pos(k,1) = contour_pos_cut(1,2);
    else
        M_curv_pos(k,1) = 0;
    end
end

%% 4. Interpolate to determine the bending moment corresponding to the
%  applied axial load for each negative curvature contour
M_curv_neg = zeros(size(contour_neg,3),2);
%       Remove zeros:
for k=1:size(contour_neg,3)
    contour_neg_index = find(contour_neg(:,1,k));
    contour_neg_cut = zeros(size(contour_neg_index));
    for iii = 1:size(contour_neg_index)
```

```
        contour_neg_cut(iii,1) =
contour_neg(contour_neg_index(iii,1),1,k);
        contour_neg_cut(iii,2) =
contour_neg(contour_neg_index(iii,1),2,k);
    end
%       Interpolate for the moment:
    M_curv_neg(k,2) = -contour_neg(1,3,k);
    if size(contour_pos_cut,1)>1
        M_curv_neg(k,1) = -
INTERPOLATE(contour_neg_cut(:,1),contour_neg_cut(:,2),N);
    elseif contour_neg_cut(1,1) == N
        M_curv_neg(k,1) = -contour_neg_cut(1,2);
    else
        M_curv_neg(k,1) = 0;
    end
end

%% 5. Stop the moment-curvature relationships at the maximum moments
M_peak_pos = max(M_curv_pos(:,1));
%       Estimate the curvature at the maximum positive moment
curv_peak_pos = INTERPOLATE(M_curv_pos(:,1),M_curv_pos(:,2),M_peak_pos);
%       Remove any curvature values larger than that at the maximum
%       positive moment:
count = 1;
while M_curv_pos(count,2)<curv_peak_pos
count = count+1;
end
M_curv_cut_pos = zeros(count,2);
for i = 1:count
    M_curv_cut_pos(i,1) = M_curv_pos(i,1);
    M_curv_cut_pos(i,2) = M_curv_pos(i,2);
end
%       Estimate the curvature at the maximum negative moment
M_peak_neg = min(M_curv_neg(:,1));
curv_peak_neg = INTERPOLATE(M_curv_neg(:,1),M_curv_neg(:,2),M_peak_neg);
%       Remove any curvature values smaller than that at the maximum
%       negative moment:
count = 1;
while M_curv_neg(count,2)>curv_peak_neg
count = count+1;
end
M_curv_cut_neg = zeros(count,2);
for i = 1:count
    M_curv_cut_neg(i,1) = M_curv_neg(i,1);
    M_curv_cut_neg(i,2) = M_curv_neg(i,2);
end

%% 6. Combine the two moment-curvature diagrams
Mcurv = zeros(( size(M_curv_cut_neg,1)+size(M_curv_cut_pos,1)),2 );
for i=1:size(M_curv_cut_neg,1)
    Mcurv(i,1) = M_curv_cut_neg(size(M_curv_cut_neg,1)+1-i,1);
    Mcurv(i,2) = M_curv_cut_neg(size(M_curv_cut_neg,1)+1-i,2);
end
for i=1:size(M_curv_cut_pos,1)
    Mcurv(i+size(M_curv_cut_neg,1),1) = M_curv_cut_pos(i,1);
    Mcurv(i+size(M_curv_cut_neg,1),2) = M_curv_cut_pos(i,2);
```

```
end
end
```

C.4.2 *PDELTA*

```
function total_BMD_step = PDELTA(Mcurv, elas_prop,PBMD,N)
%% 1. Input Parameters
%       Mcurv: matrix containing the moment-curvature relationship of
%              the cross section (N.mm, rad/mm)
%       PBMD: bending moment diagram for the primary, simply
%             supported, interior span (mm, N.mm)
%       elas_prop: column vector containing stiffness properties
%            [3*gamma_L*E*I/L; 3*gamma_R*E*I/L; K_theta; plas_hinge];
%       N: axial load (N)

%% 2. Deflection Iterations:
PBMD_step = PBMD;
total_BMD_step = PBMD;
delta1 = zeros(size(PBMD,1),1);
delta_inc = 1;   %  set to begin while loop
while max(abs(delta_inc)) > 0.01 % set for tolerance (units of length)
%       Distribute the moments along the interior span:
    RBMD = ENDMOM(Mcurv,PBMD_step,elas_prop);
    format longg
%       Check to ensure the deck has not failed:
    if max(abs(RBMD(:,2))) == 0
    delta_inc = zeros(size(RBMD,1),1);
    else
%       Compute the deflection due to the distributed moment diagram:
    avg_stiff_rev = AVGSTIFF(Mcurv, RBMD);
    delta0 = delta1;
    delta1 = DEFLECTION(avg_stiff_rev, RBMD);
    delta_inc = delta1(:,1)-delta0(:,1);
    end
%       Define the new primary moment as the old PBMD plus the second-
%       order moment
    PBMD_step(:,2) = PBMD(:,2) + N*delta1(:,1);
%       Check if the new primary moment is less than the maximum:
    if max(abs(PBMD_step(:,2))) > (Mcurv(size(Mcurv,1),1)-Mcurv(1,1))
        total_BMD_step(:,2) = zeros(size(PBMD,1),1);
        delta_inc = zeros(size(PBMD,1),1); % stop the while loop
    else
%       Define the total moment as the old RBMD plus the incremental
%       second-order moment. All of the moment values will be zero if
%       the member failed.
    total_BMD_step(:,2) = RBMD(:,2)+ N*(delta_inc);
    end
end
end
```

C.4.3 *CSDECK*

```
function [sec_ord_BMD] = CSDECK(slenderness_ratio,
axial_load_ratio)%axial_load_ratio
%% 1. Enter Input Parameters:
```

```
%       All inputs are entered directly into this function.
%       USE UNITS OF: N, mm, MPa.
hs = 240; % deck slab thickness
w = 1000; % deck slab width
rho = 0.01; % gross reinforcement ratio
n_slice = 50; % number of slices used to discretize the cross-
%               section for computing the moment-curvature
%               relationship

%       Enter the stress-strain relationship of concrete.
%       The first strain and stress values must be 0,and the last
%       strain value should be the ultimate strain.
fc=40;
strain =[0  0.0001  0.0003  0.0005  0.0007  0.0009  0.0011  0.0013
0.0015  0.0017  0.001898    0.0019  0.0021  0.0023  0.0025  0.0027
0.0029  0.0031  0.0033  0.0035];
stress =[0.00   2.78    8.32    13.79   19.06   23.94   28.20   31.65
34.12   35.55   36.00   35.99   34.19   31.48   28.29   24.98   21.82
18.93   16.37   14.15];

%       Enter the area and centroid of the steel layers:
%       Each row should be one layer [Area1, depth from top face1;...]
steel_layers = [rho*hs*w/2  35; rho*hs*w/2  205];
fy = 400; % yield stress
Es = 200000; % modulus of elasticity of the reinforcement
steel_comp = 0; % enter 1 to consider steel in compression,
%                 enter 0 to ignore it.

L = slenderness_ratio*hs/sqrt(12); % floorbeam spacing
E = 3300*sqrt(fc)+6900; % concrete modulus of elasticity
K_theta = 0; % rotational restraint provided by the floorbeams
n_elem = 50; % number of segments used to discretize the interior span
N = axial_load_ratio*hs*w*fc; % applied axial load

%       Enter the shape of the first-order moment diagram for the
%       given loading applied to the simply supported primary
%       structure as a series of points, starting from a location of 0,
%       until a location of L. The magnitude of the moments does not
%       matter, provided the diagram has the correct shape. Both
%       [location] and [moment] must be column vectors.
location = [0; L/3; 2*L/3; L];
moment = [0; 1; 1; 0];
first_ord_type = 1; % enter 1 to perform a nonlinear-cracked analysis
%                     enter 0 to perform a linear-uncracked analysis

%% 2. Generate the Moment-Curvature Relationship
%       Organize the input data:
conc_prop = zeros(length(strain),2);
for i = 1:1:length(strain)
    conc_prop(i,1) = -strain(1,length(strain)+1-i);
    conc_prop(i,2) = -stress(1,length(stress)+1-i);
end
conc_layers = SECTION(hs,w,n_slice);
steel_prop = STEEL(conc_prop,fy,Es,steel_comp);
%       Compute the plastic centroid
plas_cent = CENTROID(conc_layers,steel_layers,conc_prop,steel_prop);
```

```
format shortg
%       Call MOMCURV.m to derive the moment-curvature relationship
Mcurv =
MOMCURV(conc_layers,steel_layers,conc_prop,steel_prop,plas_cent,N);

%% 3. Compute the maximum primary moment that can be applied
%       Determine if the load is above or below the balanced failure
%       load, to determine if plastic redistribution can occur.
d = max(steel_layers(:,2));
c = 0.0035/(0.002+0.0035)*d;
alpha_1 = max(0.85-0.0015*fc,0.67);
beta_1 = max(0.97-0.0025*fc,0.67);
T = fy * steel_layers(2,1);
Cc = alpha_1*fc*beta_1*c*w;
if steel_comp ==0
    Cs = 0;
elseif steel_comp==1
    Cs = steel_layers(1,1)* (min((c-steel_layers(1,2))/c*0.0035*Es ,fy)-
alpha_1*fc);
end
N_bal = Cc + Cs - T;
if N>N_bal
    plas_hinge = 0;
else
    plas_hinge = 1;
end
%       Compute the gamma factors for the adjacent spans:
I = w*(hs)^3/12;
gamma_L = (4*E*I/L - 2*N*L/15 - (2*E*I/L + N*L/30)^2 / (4*E*I/L -
2*N*L/15)) /(3*E*I/L);
gamma_R = (4*E*I/L - 2*N*L/15 - (2*E*I/L + N*L/30)^2 / (4*E*I/L -
2*N*L/15)) /(3*E*I/L);
if gamma_L < 0
    gamma_L = 0;
end
if gamma_R < 0
    gamma_R = 0;
end
%       [elas_prop] is 4x1 matrix containing the elastic properties
%       used to distribute the moments in the interior span
elas_prop = [3*gamma_L*E*I/L; 3*gamma_R*E*I/L; K_theta; plas_hinge];
%       Compute a unit bending moment diagram
BMD_unit = UNITM(location,moment,n_elem,L);
%       Compute the maximum possible primary moment diagram
MaxPBMD(:,1) = BMD_unit(:,1);
MaxPBMD(:,2) = BMD_unit(:,2)*(Mcurv(size(Mcurv,1),1)-Mcurv(1,1));
%       Starting with the maximum possible primary moment, call
%       PDELTA.m to determine the total moment diagram, including
%       second-order effects, and then begin incrementally reducing
%       the primary moments until PDELTA.m returns a non-zero
%       solution.
sec_ord_BMD = PDELTA(Mcurv, elas_prop,MaxPBMD,N);
count = 1;
while max(sec_ord_BMD(:,2))==0 && count < 200
    MaxPBMD(:,2) = BMD_unit(:,2)*(Mcurv(size(Mcurv,1),1)-
Mcurv(1,1))*(200-count)/200;
    sec_ord_BMD = PDELTA(Mcurv, elas_prop,MaxPBMD,N);
```

```
    count = count+1;
end
format shortg
%       Display warnings if plastic redistribution occurred:
if abs(sec_ord_BMD(1,2)/Mcurv(1,1)) < 1.001 &&
abs(sec_ord_BMD(1,2)/Mcurv(1,1)) > 0.999
disp('Left support formed plastic hinge');
end
if abs(sec_ord_BMD(size(sec_ord_BMD,1),2)/Mcurv(1,1)) < 1.001 &&
abs(sec_ord_BMD(size(sec_ord_BMD,1),2)/Mcurv(1,1)) > 0.999
disp('Right support formed plastic hinge');
end

%% 3. Perform a first-order analysis to determine the distribution of
%  the maximum primary moments
if first_ord_type == 1 % performs a nonlinear-cracked analysis
    Mcurv_first = Mcurv;
elseif first_ord_type == 0 % performs a linear-uncracked analysis
    Mcurv_first = [Mcurv(1,2)*E*I, Mcurv(1,2);
Mcurv(size(Mcurv,1),2)*E*I, Mcurv(size(Mcurv,1),2)];
else
    disp('fir_ord_tpye must be 1 or 0');
end
elas_prop_1 = [3*E*I/L; 3*E*I/L; K_theta; plas_hinge];
first_ord_BMD = ENDMOM(Mcurv_first,MaxPBMD,elas_prop_1);

%% 4. Output:
str1 = ['The max. positive moment is ',
num2str(round(max(sec_ord_BMD(:,2)))), ', or ',
num2str(round(max(sec_ord_BMD(:,2))/Mcurv(size(Mcurv,1),1)*100)),'
percent of the cross-section capacity.'];
str2 = ['The max. negative moment is ',
num2str(round(min(sec_ord_BMD(:,2)))), ', or ',
num2str(round(min(sec_ord_BMD(:,2))/Mcurv(1,1)*100)),' percent of the
cross-section capacity.'];
str3 = ['The max. positive first-order moment of ',
num2str(round(max(first_ord_BMD(:,2)))),' is magnified by a factor of ',
num2str(roundn(max(sec_ord_BMD(:,2))/max(first_ord_BMD(:,2)),-2)),'.'];
str4 = ['The max. negative first-order moment of ',
num2str(round(min(first_ord_BMD(:,2)))),' is magnified by a factor of ',
num2str(roundn(min(sec_ord_BMD(:,2))/min(first_ord_BMD(:,2)),-2)),'.'];
disp(str1);
disp(str2);
disp(str3);
disp(str4);
end
```

APPENDIX D: SENSITIVITY ANALYSIS RESULTS FOR SINGLE-POINT-LOAD CASE

This appendix contains selected results from the sensitivity analysis for the load case with a single vertical point load applied to the midspan of the interior span. All of the results shown in Chapter 5, for the case with two vertical point loads, are shown in this section for the single-point-load case.

D.1 *CSDECK* RESULTS FOR VARIOUS APPLIED AXIAL LOAD RATIOS

Figure D.1 shows the moment magnifier plotted against the applied axial load ratio and is comparable to Figure 5.4 for the two-point-load case. Essentially all of the same trends that are discussed in Section 5.4 for the two-load-point-case are also apparent in Figure D.1 a), except magnitude of the moment magnifiers at any given applied axial load and slenderness ratio are less. The two point loads create a region of uniform moment in middle of the interior span, as discussed in Section 5.3.2. This region creates large curvatures at midspan and therefore, large deflections and second-order effects. The single point load does not create this uniform moment region, so the second-order effects are not as significant and the moment magnifiers are less.

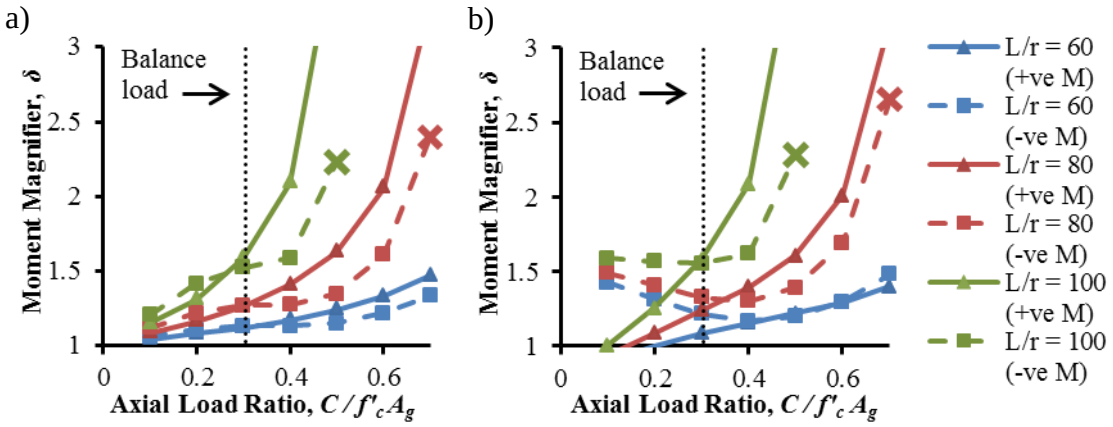

Figure D.1: Moment magnifier for various applied axial load ratios when f'_c = 55MPa, using the following first-order analyses: a) nonlinear-cracked; b) linear-uncracked.

Figure D.2 shows the ratio of the moment magnifier computed using a linear-uncracked analysis, δ_L, to those computed using the nonlinear-cracked analysis, δ_{NL}, for the single-point-load case and is comparable to Figure 5.6 for the two-point-load case. The linear-uncracked analysis provides a more accurate prediction of the first-order moments for the single-point-load case than for the two-point-load case, but all other trends described in Section 5.4 for the two-point-load case apply to the single-point-load case as well. As explained in Section 5.4, the error in the linear-uncracked analysis is due to the analysis overestimating the midspan rigidity and so underestimating the midspan curvature, as shown in Figure 5.7. Since the single point load does not create a large region of uniform curvature near midspan, the error in linear-uncracked analysis is not as significant.

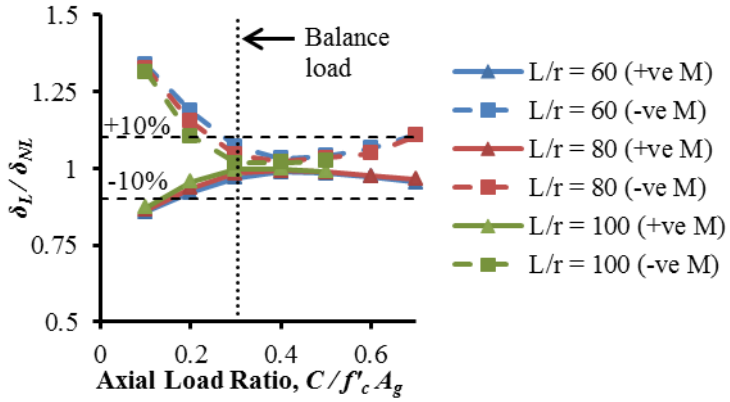

Figure D.2: Ratio of moment magnifiers computed for various applied axial loads using a linear-uncracked first-order analysis to those using a nonlinear-cracked first-order analysis.

As noted in Section 5.4 for the two-point-load case, the difference between the results obtained from the two first-order analyses is larger when f'_c equals 40MPa and this is also true for the single-point-load case. However, the difference between the results when f'_c equals 40MPa is still less than 10% at all slenderness ratios when the applied axial load is from $0.4 f'_c A_g$ to $0.6 f'_c A_g$, rather than from only $0.4 f'_c A_g$ to $0.5 f'_c A_g$ for the two-point-load case.

D.2 *CSDECK* RESULTS FOR VARIOUS SLENDERNESS RATIOS

Figure D.3 shows the moment magnifier plotted against the slenderness ratio and is comparable to Figure 5.10 for the two-point-load case. All of the trends discussed in Section 5.5 for the two-point-load case are also apparent in Figure D.3, except the magnitudes of the moment magnifiers at any given applied axial load and slenderness ratio are less, as explained in the previous section.

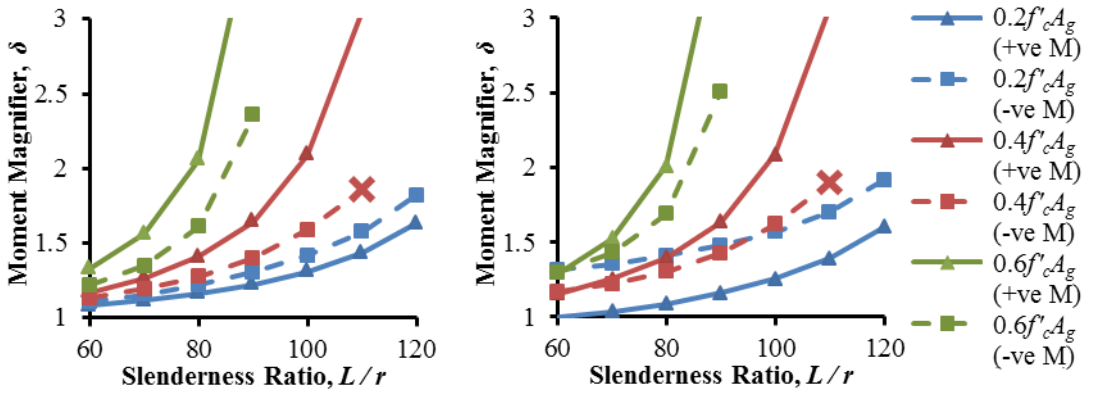

Figure D.3: Moment magnifier for various slenderness ratios when f'_c = 55MPa, using the following first-order analyses: a) nonlinear-cracked; b) linear-uncracked.

Figure D.4 shows the ratio of the moment magnifier computed using a linear-uncracked analysis, δ_L, to those computed using the nonlinear-cracked analysis, δ_{NL}, for the single-point-load case and is comparable to Figure 5.12 for the two-point-load case. Again, the linear-uncracked analysis provides a better prediction of the nonlinear-cracked moments for the single-point-load case than for the two-point-load case and again the difference between the two analyses reduces as *L/r* increases, as noted in Section 5.5.

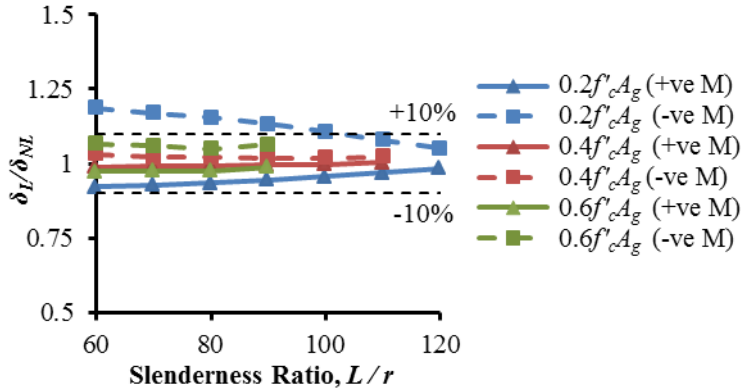

Figure D.4: Ratio of moment magnifiers computed using a linear-uncracked first-order analysis and a nonlinear-cracked first-order analysis for various slenderness ratios.

It was noticed in Section 5.5 for the two-point-load case, that the difference between the results obtained from the two first-order analyses is larger when f'_c equals 40MPa and this is also apparent for the single-point-load case. For this case, the difference when f'_c is 40MPa is always less than 10% when the applied axial load is from $0.4 f'_c A_g$ to $0.6 f'_c A_g$, but is always greater than 10% when $C = 0.2 f'_c A_g$.

D.3 *CSDECK* RESULTS FOR VARIOUS CONCRETE COMPRESSIVE STRENGTHS

Figure D.5 shows the moment magnifier plotted against the concrete strength, f'_c, for the single-point-load case and is comparable to Figure 5.13 for the two-point-load case. As discussed in Section 5.6 for the two-point-load case, increasing f'_c decreases the moment magnifiers, since it increases both the modulus of elasticity, E_c, and for a given applied axial load, C, it reduces the applied axial load ratio, $C/f'_c A_g$, which typically reduces the moment magnifier, as discussed in Section 5.4. Again, the moment magnifiers are generally smaller for the single-point-load case than the two-point-load case, as explained in Section D.1.

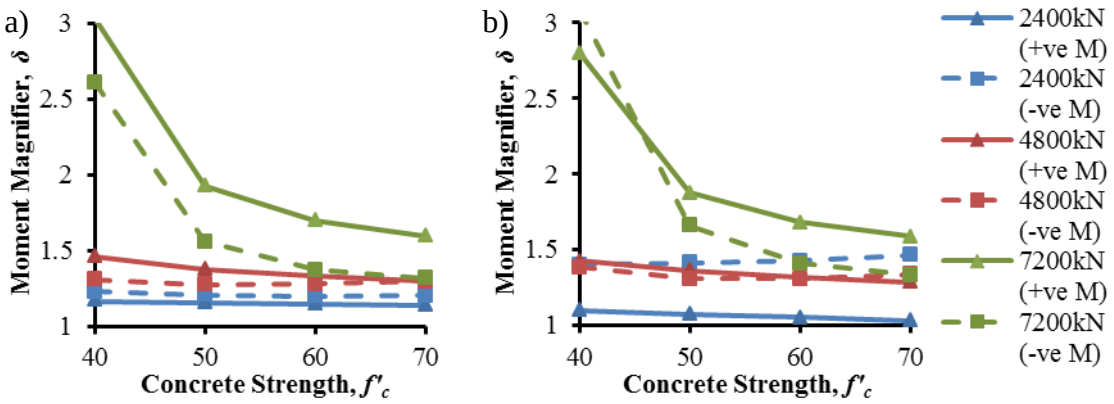

Figure D.5: Moment magnifier for various concrete compressive strengths when *L/r* = 80, using: a) nonlinear-cracked first-order analysis; b) linear-uncracked first-order analysis.

D.4 *CSDECK* RESULTS FOR VARIOUS FLOORBEAM ROTATIONAL RESTRAINTS

Figure D.5 shows the moment magnifier, computed using the nonlinear-cracked analysis, plotted against the rotational restraint provided by the floorbeams, K_θ, for the single-point-load case and is comparable to Figure 5.14 for the two-point-load case. As discussed in Section 5.7 for the two-point-load case, increasing K_θ also reduces the moment magnifier for this case, except there is no exception at the applied axial load of $0.2 f'_c A_g$. The support moments never reach the cross-section capacity in the single-point-load case, so plastic redistribution does not occur. To develop large negative moments there must be a reduction in rigidity near midspan causing a significant increase in the area under the curvature diagram, as explained in Section 5.4 and shown in Figure 5.7. The single point load creates a reduction in rigidity that is concentrated at midspan, affecting a smaller area on the curvature diagram than the double point loads, so the negative moments are always less.

Again, increasing K_θ within the range expected for steel floorbeams only has a significant effect on the moment magnifier, δ, if δ is greater than 2 for K_θ = 0. In these cases increasing K_θ to the upper bound for the steel floorbeams of the Alex Fraser Bridge reduces δ just below 2, but a much more effective reduction can be achieved if K_θ is increased further to values more representative of concrete floorbeams.

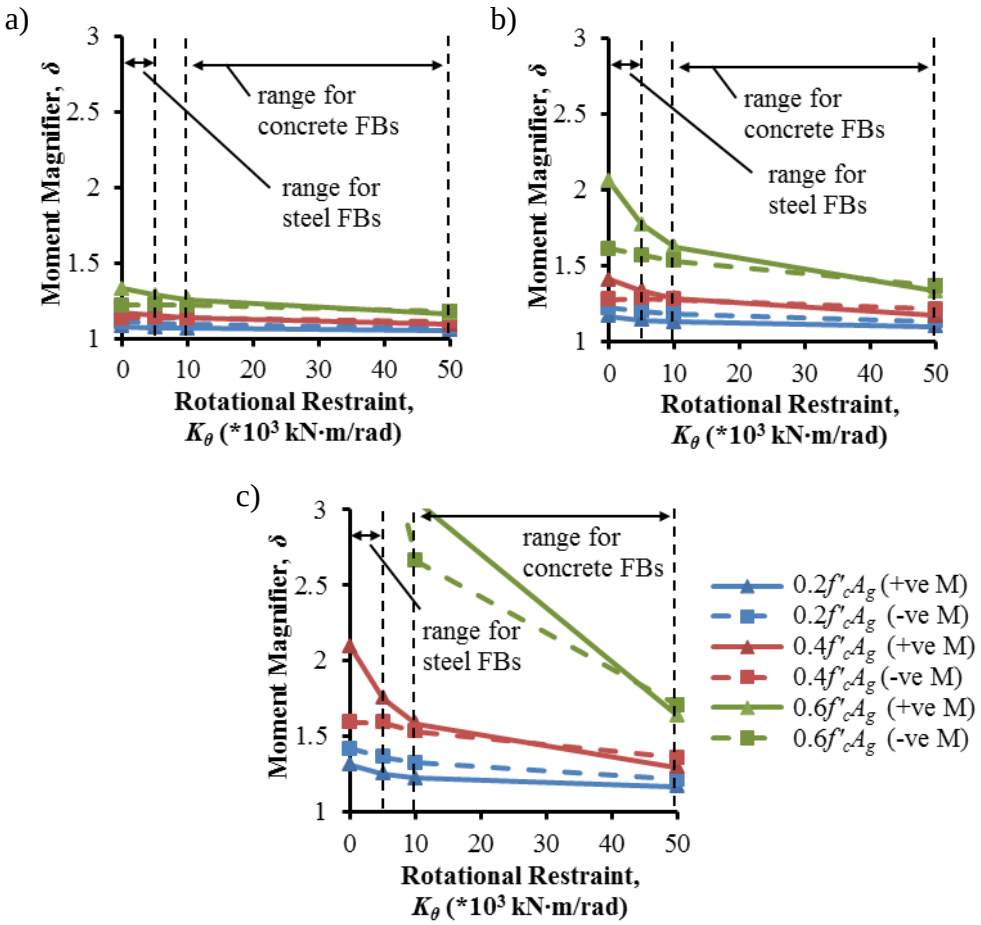

Figure D.6: Moment magnifiers from a nonlinear-cracked first-order analysis for various floorbeam rotational restraints; a) L/r = 60; b) L/r = 80; c) L/r = 100.

Figure D.7 shows the ratio of the moment magnifier computed using the linear-uncracked analysis to those computed using the nonlinear-cracked analysis, for the members with

L/r = 60 subjected to a single vertical point load. Again it is apparent that the accuracy of the linear-uncracked first-order analysis improves slightly as K_θ is increased, although the increase in Figure D.7 is not as significant as in Figure 5.15 for the two-point-load case. The large negative moments in the two-point-load case reduce the first-order moments at midspan, improving the accuracy of the linear-uncracked analysis, as explained in Section 5.7. The smaller negative moments in the single-point-load case have less of an effect on the first-order moments, so K_θ has less influence on the accuracy of the linear-uncracked analysis. This also explains why the accuracy of the linear-uncracked analysis when is better for the two-point-load case than for the single-point-load case when K_θ = 50*10^3 kN·m/rad. For all the other ranges of variables that were examined the accuracy was best for the single-point-load case, but the effect of the large negative moments, caused by the double point loads and large K_θ value, improves the prediction provided by the linear-uncracked analysis.

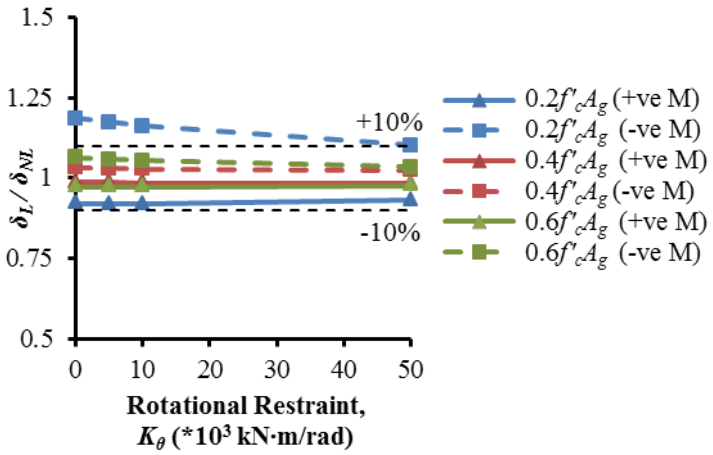

Figure D.7: Ratio of moment magnifiers computed using a linear-uncracked first-order analysis and a nonlinear-cracked first-order analysis for various rotational restraints; L/r = 60.

D.5 *CSDECK* RESULTS FOR VARIOUS REINFORCEMENT RATIOS AND STEEL DEPTHS

Figures D.8 and D.9 show the moment magnifier plotted against the reinforcement ratio, ρ_g, and steel-depth-to-slab-thickness ratio, d/h_s, respectively, for the deck slab with f'_c = 55MPa and L/r = 80 subjected to a single vertical point load and are comparable to Figures 5.16 and 5.17, respectively, for the two-point-load case. Both figures reinforce the conclusions made in Chapter 5, that the parameters, ρ_g and d/h_s, have a negligible influence on the moment magnification of slender cable-stayed bridge decks.

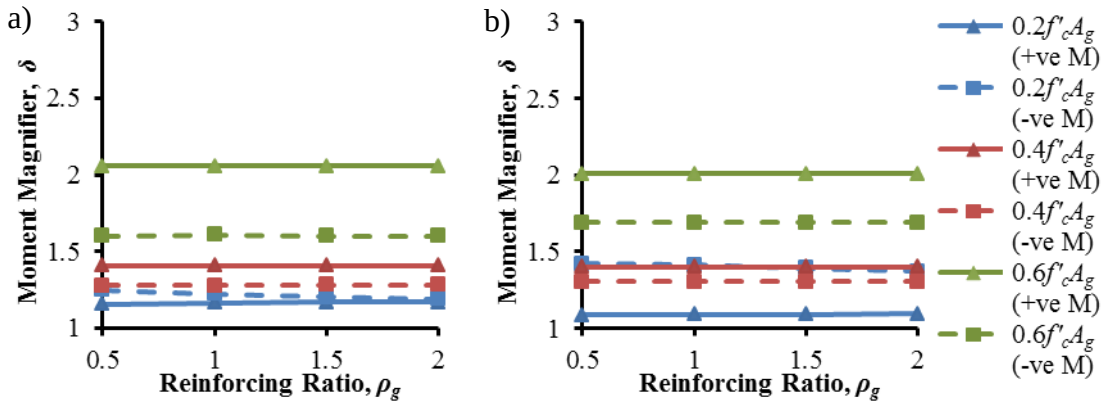

Figure D.8: Moment magnifiers for various reinforcing ratios, using the following first-order analyses: a) nonlinear-cracked b) linear-uncracked.

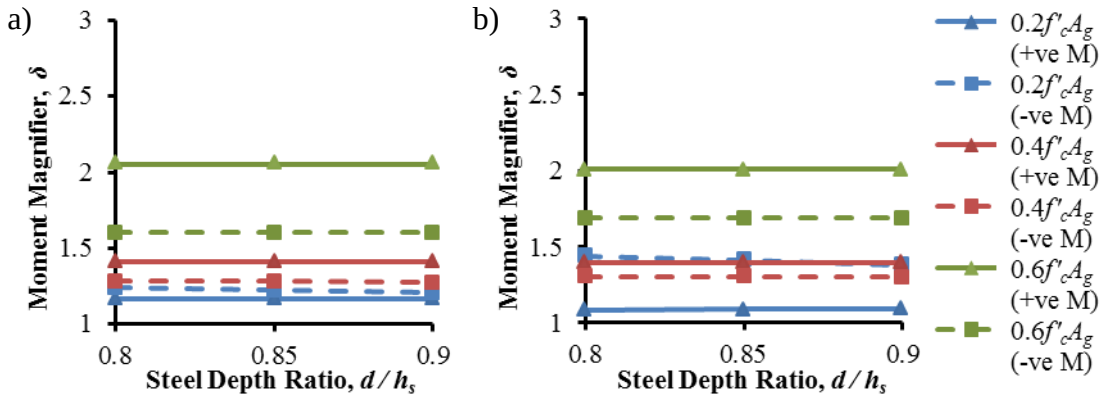

Figure D.9: Moment magnifiers for various steel-depth-to-slab-thickness ratios, using the following first-order analyses: a) nonlinear-cracked; b) linear-uncracked.

CIRRICULUM VITAE

Identification Zachary T. McNeil, b. Bridgetown NS, 1989

Post Secondary Education

2011 – 2013 Master of Engineering Science, MESc, Civil
The University of Western Ontario, London, Canada

2007 – 2011 Bachelor of Science in Engineering, BScE, Civil
The University of New Brunswick, Fredericton, Canada

Honors and Awards

2012 – 2013 QEII Graduate Scholarship in Science and Technology (QEIIGSST)
The University of Western Ontario, London, Canada

2011 – 2012 NSERC Alexander Graham Bell Canada Graduate Scholarship (CGS)
The University of Western Ontario, London, Canada

2008 – 2011 Dean's List in the Faculty of Engineering
The University of New Brunswick, Fredericton, Canada

2007 – 2011 Currie Scholarship in Engineering
The University of New Brunswick, Fredericton, Canada

2010 Francis Vanicek Prize in Civil Engineering
The University of New Brunswick, Fredericton, Canada

2009 Alan K. Grimmer Prize in Civil Engineering
The University of New Brunswick, Fredericton, Canada

Related Employment

2011 – 2013 Research Assistant, Teaching Assistant
The University of Western Ontario, London, Canada

2008 – 2010 Student Labourer (Bridge Construction Crew)
NS Department of Transportation and Infrastructure Renewal,
Middleton, Canada

Related Publications and Presentations

McNeil, Z. & Bartlett, F.M. 2013. Effective Length of Cable-stayed Bridge Decks, *Proceedings of the CSCE 2013 3rd Specialty Conference on Engineering Mechanics and Materials*, Montreal, QC, MEC-053, 10-page paper in CD-ROM Proceedings.

McNeil, Z. & Bartlett, F.M. 2012. Instability of Cable-stayed Bridge Decks, *Presentation given at the ACI Fall 2012 Convention - Research in Progress Session Part II*, Toronto, ON.